HOW TO ACCOUNT FOR UNCERTAINTY IN SOIL PROPERTIES IN OFFSHORE MONOPILE DESIGN BY MEANS OF PROBABILISTIC ANALYSIS

A THESIS SUBMITTED TO
THE GRADUATE SCHOOL OF NATURAL AND APPLIED SCIENCES
OF
MIDDLE EAST TECHNICAL UNIVERSITY

BY

OLGU ORAKCI

IN PARTIAL FULFILLMENT OF THE REQUIREMENTS
FOR
THE DEGREE OF MASTER OF SCIENCE
IN
CIVIL ENGINEERING

FEBRUARY 2022

Approval of the thesis:

HOW TO ACCOUNT FOR UNCERTAINTY IN SOIL PROPERTIES IN OFFSHORE MONOPILE DESIGN BY MEANS OF PROBABILISTIC ANALYSIS

submitted by **OLGU ORAKCI** in partial fulfillment of the requirements for the degree of **Master of Science in Civil Engineering Department, Middle East Technical University** by,

Prof. Dr. Halil Kalıpçılar
Dean, Graduate School of **Natural and Applied Sciences** _____

Prof. Dr. Erdem Canbay
Head of Department, **Civil Engineering** _____

Assoc. Prof. Dr. Nejan Huvaj
Supervisor, **Civil Engineering, METU** _____

Prof. Dr. Georgios Anogiatis
Co-supervisor, **Civil Engineering, KU Leuven** _____

Examining Committee Members:

Prof. Dr. Erdal Çokça
Civil Engineering, METU _____

Assoc. Prof. Dr. Nejan Huvaj
Civil Engineering, METU _____

Prof. Dr. Stijn François
Civil Engineering, KU Leuven _____

Prof. Dr. Berna Unutmaz
Civil Engineering, Hacettepe University _____

Assoc. Prof. Dr. Kartal Toker
Civil Engineering, METU _____

Date: 28.02.2022

I hereby declare that all information in this document has been obtained and presented in accordance with academic rules and ethical conduct. I also declare that, as required by these rules and conduct, I have fully cited and referenced all material and results that are not original to this work.

Name, Surname: Olgu Orakcı

Signature :

ABSTRACT

HOW TO ACCOUNT FOR UNCERTAINTY IN SOIL PROPERTIES IN OFFSHORE MONOPILE DESIGN BY MEANS OF PROBABILISTIC ANALYSIS

Orakcı, Olgu
M.S., Department of Civil Engineering
Supervisor: Assoc. Prof. Dr. Nejan Huvaj
Co-Supervisor: Prof. Dr. Georgios Anogiatis

February 2022, 107 pages

Offshore wind turbines gain more importance worldwide as they contribute to reduce greenhouse gas emissions and achieve a low-carbon future producing sustainable energy. Monopile is the most commonly employed foundation type for offshore wind turbines. Monopile design requires a comprehensive assessment of seabed soil properties with depth. However, seabed soils involve inherent variability and uncertainty in material properties. Modifications to deterministic design approaches are suggested in the literature to account for uncertainties and achieve target reliability. This study aims to incorporate the uncertainty of soil properties in a probabilistic approach to reach a more reliable and cost-efficient design. Thus, a one-dimensional analysis by the p-y method is conducted to check structural stability and serviceability according to American Petroleum Institute (API) and Det Norske Veritas - Germanischer Lloyd (DNV-GL) guidelines. Hence, nonlinear springs are assigned along the length of the monopile to account for the soil-structure interaction. Analyses are conducted using OpenSees as a nonlinear solver and Python for batch runs. Monte Carlo Simulation is employed to generate random fields. Firstly, the analysis method is

verified by comparing the deterministic analysis for a case study in Denmark. Then, probabilistic analysis is applied to the case study and a newly designed monopile in Belgium offshore. Results show that seabed soil variability can affect the probability of unsatisfactory performance (PUP) depending on the specific soil conditions (Denmark Case Study less than 1%, Belgium Case Study 12%). Furthermore, the selection of soil parameter distribution function can affect PUP for high coefficient of variation values.

Keywords: offshore wind turbines, probabilistic, uncertainty, monopiles

ÖZ

ZEMİN PARAMETRELERİNDEKİ BELİRSİZLİKLERİN DENİZÜSTÜ RÜZGAR TÜRBİNİ TASARIMINA ETKİSİNİN OLASILIKSAL YÖNTEMLER İLE İNCELENMESİ

Orakcı, Olgu
Yüksek Lisans, İnşaat Mühendisliği Bölümü
Tez Yöneticisi: Doç. Dr. Nejan Huvaj
Ortak Tez Yöneticisi: Prof. Dr. Georgios Anogiatis

Şubat 2022 , 107 sayfa

Açık deniz rüzgar türbinleri sürdürülebilir enerji üreterek sera gazı salınımını azaltmaya ve düşük karbon bir gelecek sağlamaya katkı sağlayarak dünyada giderek önem kazanmaktadır. Tekil kazık ise en çok kullanılan temel çeşididir. Tekil kazık tasarımı için açık deniz zemin parametlerinin derinlikle değişiminin kapsamlı bir şekilde değerlendirilmesi gereklidir. Ayrıca bu zeminler doğal yapıları gereği değişkenlik ve belirsizlik içerir. Belirsizlikleri hesaba katmak ve hedef güvenilirliği sağlamak için literatürde deterministik tasarım yaklaşımlarında modifikasyonlar önerilmektedir. Buna paralel olarak, bu çalışmanın temel amacı, daha güvenilir ve düşük maliyetli bir tek kazık tasarımına ulaşmak için zemin özelliklerinin belirsizliğini olasılıksal bir yaklaşımla değerlendirmektir. Bu tez kapsamında, American Petroleum Institute (API) ve Det Norske Veritas - Germanischer Lloyd (DNV-GL) klavuzlarına göre tekil kazıkların yapısal stabilitesini ve servis ömrü dayanılırlığını kontrol etmek için p-y yöntemiyle tek boyutlu analizler yapılmıştır. Zemin-yapı etkileşimini hesaba katmak için API klavuzuna uygun olarak tekil kazık boyunca nonlineer Winkler yayları atanır.

Analizler doğrusal olmayan çözücü OpenSees ve toplu analizler için Python kullanılarak yapılmıştır. Monte Carlo Simülasyonu rastsal alanlar oluşturmak için kullanılmıştır. Bu olasılıksal analizler için önce literatürden bir örnek tekil kazık çalışması incelenmiş (Danimarka) ve yöntem doğrulandıktan sonra Belçika açıklarında yeni bir tekil kazık dizayn edilmiştir. Sonuçlar, deniz tabanı zemin değişkenliğinin, belirli zemin koşullarına bağlı olarak yetersiz performans olasılığını etkileyebileceğini göstermektedir (Danimarka çalışması için yetersiz performans olasılığı 1%den az, Belçika çalışması için 12%). Ayrıca, zemin parametresi istatistiksel dağılım fonksiyonunun seçiminin, yüksek belirsizlik katsayısı değerleri için yetersiz performans oranını etkileyebileceği görülmüştür.

Anahtar Kelimeler: deniz üstü rüzgar türbinleri, olasılıksal, belirsizlik, tekil kazık

Dedicated to my family...

ACKNOWLEDGMENTS

This master's thesis is a joint work between KU Leuven and Middle East Technical University. I had the opportunity to conduct my research under the Erasmus Exchange Program.

I would like to thank my supervisors for their guidance during my research. Special thanks to Dr. Nejan Huvaj, who made this joint work possible by unlimited courage and support. Special thanks to Dr. Georgios Anogiatis, who accepted me as an Erasmus exchange student with lots of endorsement on the way. Special thanks to Dr. Stijn François, who reinforced the work with different perspectives and supported me with writing. I am grateful for all the things I learned from them. I also want to thank Ali Nazari Tileki for all the technical and uplifting supports.

Finally, I would like to thank my beloved family and friends for their endless support in this journey and wholesome presence in my life. Last but not least, I want to express my sincere gratitude to Türksönmez family for all their blessings.

Olgu Orakcı

Brugge, January 16, 2022

TABLE OF CONTENTS

ABSTRACT v

ÖZ vii

ACKNOWLEDGMENTS x

TABLE OF CONTENTS xi

LIST OF TABLES xiv

LIST OF FIGURES xvi

LIST OF ABBREVIATIONS xxi

CHAPTERS

1 INTRODUCTION 1

1.1 Offshore wind turbines 1

1.2 Research question and objectives of the study 9

1.3 Scope 10

2 BACKGROUND 11

2.1 Introduction 11

2.2 Analysis methods 11

2.3 p-y curves 14

2.3.1 Terzaghi curves 16

2.3.2 Analytical solutions for ultimate resistance 17

2.3.3 API curves . . . 20
2.3.4 Reese, et al. (1974) procedure curves . . . 22
2.3.5 DNV-GL curves . . . 25
2.3.6 LPile curves . . . 26
2.4 t-z curves . . . 26
2.5 Q-z curves . . . 29
2.6 Variability in soil properties . . . 30
2.7 Probabilistic evaluation of soil properties . . . 33
2.7.1 Monte Carlo analysis . . . 33
2.7.2 Probabilistic analysis parameters . . . 34
2.7.2.1 Statistical distribution of material properties . . . 34
2.7.2.2 Coefficient of variation . . . 38
2.7.2.3 Correlation coefficient . . . 38
2.7.2.4 Spatial correlation length . . . 42
2.7.3 Denmark soil data . . . 42
2.7.4 Belgium soil data . . . 43
3 DETERMINISTIC ANALYSIS FOR MONOPILES . . . 45
3.1 Introduction . . . 45
3.2 Methodology . . . 45
3.2.1 Pile properties . . . 46
3.2.2 Spring properties . . . 47
3.2.3 Load definition . . . 51
3.2.4 OpenSees analysis . . . 52

3.3 Verification of the analysis 53
3.3.1 Model parameters 55
3.3.2 Comparison of results 58
3.3.2.1 Displacement 59
3.3.2.2 Shear force 60
3.3.2.3 Moment 60
3.4 Design checks 60
3.5 Interpretation of the results 64
3.6 Conclusions 64
4 PROBABILISTIC ANALYSIS FOR MONOPILES 65
4.1 Introduction 65
4.2 Methodology 65
4.2.1 Analysis parameters 66
4.2.2 Monte Carlo simulations 69
4.3 Probabilistic study for a monopile in Denmark 72
4.4 Probabilistic study for a monopile in Belgium 77
4.4.1 Soil idealization and material properties 79
4.4.2 Monopile design 85
4.4.3 Probabilistic analysis 86
4.5 Discussion and conclusions 89
5 CONCLUSIONS AND FUTURE RECOMMENDATIONS 93
REFERENCES 97

LIST OF TABLES

TABLES

Table 2.1 Terzaghi's recommended modulus values for laterally loaded piles in sand [108] 16

Table 2.2 Friction angle versus initial modulus of subgrade reaction [101] . . . 22

Table 2.3 Reese et al.'s recommended modulus values for laterally loaded piles in sand below water table [93] 25

Table 2.4 Definition of t-z curves [101] 27

Table 2.5 Design parameters for t-z curves [101] 28

Table 2.6 Definition of Q-z curves [101] 29

Table 2.7 Design parameters for Q-z curves [101] 30

Table 2.8 Coefficient of variation values from the literature for soil material properties 40

Table 2.9 Correlation coefficient values from the literature for friction angle and unit weight 41

Table 3.1 Ultimate and serviceability design checks 63

Table 4.1 Probability of unsatisfactory performance (%) with different COV of friction angle with non-limited approach for modulus of subgrade reaction without axial loading for the case study in Denmark 73

Table 4.2 Probability of unsatisfactory performance (%) with different COV of friction angle with limited approach for modulus of subgrade reaction without axial loading for the case study in Denmark 73

Table 4.3 Probability of unsatisfactory performance (%) with different COV of friction angle with non-limited approach for modulus of subgrade reaction with axial loading for the case study in Denmark 75

Table 4.4 Probability of unsatisfactory performance (%) with different COV of friction angle with limited approach for modulus of subgrade reaction with axial loading for the case study in Denmark 75

Table 4.5 Analysis results with characteristic value for friction angle 78

Table 4.6 Belgium CPT and Borehole data used in Figure 4.12 [3] 84

LIST OF FIGURES

FIGURES

Figure 1.1 Wind turbine components [22] 2

Figure 1.2 An offshore wind farm [7] 3

Figure 1.3 Offshore and onshore wind installation expectations for 2021-2025 [64] 4

Figure 1.4 Different foundation types for offshore wind turbines [22] (a) bucket/suction caisson, (b) gravity-based, (c) monopile, (d) tripod on bucket/suction caisson, (e) jacket/lattice structure, (f) tension leg platform, and (g) spar buoy floating concept 6

Figure 1.5 The distribution of the substructures among the foundations installed in 2020 [90] 6

Figure 1.6 Example monopile structure cross section 7

Figure 1.7 Loads on a monopile structure [85] 7

Figure 1.8 Geological cross section for 5 different monopiles at The Westermost Rough Offshore Wind Farm [61] 8

Figure 1.9 A horizontal soil profile with variability of soil strength (depth unknown) [28] 9

Figure 2.1 Load-displacement curves [100] 12

Figure 2.2 Basic sketches for analysis methods (a) p-y method, (b) PISA design method, (c) macro element model and (d) 3D FEM method [5, 20] 15

Figure 2.3 Passive wedge failure assumption for piles in sand [95] 17

Figure 2.4 Passive wedge failure assumption for piles in sand [95] 19

Figure 2.5 C_1, C_2, and C_3 coefficients versus friction angle [101] 21

Figure 2.6 Characteristic shape of laterally loaded piles in sand [93] 23

Figure 2.7 Values for: (a) A_s and A_c, (b) B_s and B_c [93] 24

Figure 2.8 Initial modulus of subgrade reaction for fine sands suggested by LPile 27

Figure 2.9 Boundary approximation for normal distribution [1] 35

Figure 2.10 Normal material distribution 36

Figure 2.11 Lognormal material distribution 37

Figure 2.12 Boundary approximation for uniform distribution [2] 37

Figure 2.13 Uniform material distribution 38

Figure 2.14 Scatter of data sets with different correlation coefficients [8] . . . 39

Figure 2.15 Soil types of Denmark according to the Danish Soil Classification [25] 43

Figure 2.16 Soil classification results for northern Belgium with 480,000 soil samples [99] 44

Figure 3.1 Pile mesh 47

Figure 3.2 Spring assignment along the monopile 48

Figure 3.3 Comparison for initial modulus of subgrade reactions based on different guidelines 49

Figure 3.4 Relative density, angle of internal friction, and k chart given by previous API guideline [101] 50

Figure 3.5 Friction angle versus initial modulus of subgrade reaction 51

Figure 3.6 Point of loading 52

Figure 3.7 Location of the Horns Rev I offshore wind farm 54

Figure 3.8 Model idealization 54

Figure 3.9 Vestas V80-2.0 MW turbine [9] 55

Figure 3.10 Soil layering and material properties 56

Figure 3.11 p-y curves 57

Figure 3.12 T-z curve 57

Figure 3.13 Q-z curve 58

Figure 3.14 Displacement comparison 59

Figure 3.15 Shear comparison 61

Figure 3.16 Moment comparison 62

Figure 4.1 Probability of density functions for: (a) friction angle, (b) buoyant unit weight, (c) modulus of subgrade reaction. (d) Correlation between friction angle and unit weight for normal distribution 68

Figure 4.2 Probability of density functions for: (a) friction angle, (b) buoyant unit weight, (c) modulus of subgrade reaction. (d) Correlation between friction angle and unit weight for lognormal distribution 69

Figure 4.3 Probability of density functions for: (a) friction angle, (b) buoyant unit weight, (c) modulus of subgrade reaction. (d) Correlation between friction angle and unit weight for uniform distribution 70

Figure 4.4 Number of runs vs. probability of unsatisfactory performance for Monte Carlo simulations 71

Figure 4.5 Analysis parameters (a) the initial modulus of subgrade reaction, (b) load conditions 72

Figure 4.6 Modulus of subgrade reaction distribution along the pile 76

Figure 4.7 Pile tip deformations for different COV values of friction angle . 78

Figure 4.8 Selected CPT location in Belgium offshore 79

Figure 4.9 Borehole data near to the selected CPT location 79

Figure 4.10 Soil classification charts by Robertson [96] 80

Figure 4.11 CPT tip resistance versus friction angle correlation graph with different calibration chamber corrections [58] 81

Figure 4.12 CPT tip resistance versus friction angle correlation graph with different calibration chamber corrections with Belgium soil data 83

Figure 4.13 Correlation between CPT results and unit weight [97] 84

Figure 4.14 Idealized soil data on CPT data in Belgium offshore 85

Figure 4.15 Robertson chart for the CPT in Belgium offshore 86

Figure 4.16 Idealized soil sketch for the CPT in Belgium offshore with designed monopile 87

Figure 4.17 The designed monopile geometry and properties on Belgian offshore 88

Figure 4.18 Probability of density functions for: (a) friction angle, (b) buoyant unit weight, (c) modulus of subgrade reaction. (d) Correlation between friction angle and unit weight for normal distribution 89

Figure 4.19 Probability of density functions for: (a) friction angle, (b) buoyant unit weight, (c) modulus of subgrade reaction. (d) Correlation between friction angle and unit weight for lognormal distribution 90

Figure 4.20 Probability of density functions for: (a) friction angle, (b) buoyant unit weight, (c) modulus of subgrade reaction. (d) Correlation between friction angle and unit weight for uniform distribution 91

LIST OF ABBREVIATIONS

1D	1 Dimensional
3D	3 Dimensional
API	American Petroleum Institute
CL	Center Line
CPT	Cone Penetration Test
COV	Coefficient of Variation
DNV-GL	Det Norske Veritas - Germanischer Lloyd
HP	Hypo Plastic
HS	Hardening Soil
HSsmall	Hardening Soil for small strain stiffness increase
MC	Mohr-Coulomb
MSL	Mean Sea Level
SCL	Spatial Correlation Length
c	Correlation coefficient $[-]$
f_a	Absolute value of acting axial stress $[MPa]$
f_{bx}	Absolute value of acting resultant bending stress in x direction $[MPa]$
f_{by}	Absolute value of acting resultant bending stress in y direction $[MPa]$
f_s	Maximum beam shear stress $[MPa]$
k	Initial modulus of subgrade reaction $[MN/m^3]$
p	Lateral soil resistance $[kN/m]$
p_u	Ultimate soil resistance $[kN/m]$
p_{us}	Ultimate soil resistance for shallow depths $[kN/m]$

p_{ud}	Ultimate soil resistance for deep depths $[kN/m]$
q_c	CPT cone tip resistance $[m]$
s	Mesh size $[m]$
t	Thickness $[m]$
A	Cross sectional area $[m^2]$
A_m	Area of rotor swept area $[m^2]$
C	Correlation matrix $[-]$
D	Diameter $[m]$
D_r	Relative density $[\%]$
D_{r0}	Initial relative density $[\%]$
E	Young's modulus $[GPa]$
F_a	Active force $[kN]$
F_b	Allowable bending stress $[MPa]$
F_h	Horizontal load $[MN]$
F_p	Passive force $[kN]$
F_{pt}	The total lateral force $[kN]$
F_s	Allowable beam shear stress $[MPa]$
F_v	Vertical load $[MN]$
F_{xc}	Inelastic local buckling stress $[MPa]$
F_y	Yield strength $[MPa]$
I	Moment of inertia $[m^4]$
K	Radius of gyration $[m]$
K_0	Coefficient of earth pressure at rest $[-]$
K_a	Coefficient of active earth pressure $[-]$
L	Total length of the monopile $[m]$
L_e	Embedded length of the monopile $[m]$
L_f	Free length of the monopile $[m]$

M	Bending moment $[MN \cdot m]$
P	Power $[W]$
P_a	Atmospheric pressure $[atm]$
P_v	Axial loading $[MN]$
Q_c	Ultimate axial capacity of piles in compression $[MN]$
Q_{fc}	Shaft friction capacity in compression $[MN]$
Q_p	End bearing capacity $[MN]$
R^2	Coefficient of determination $[-]$
U	Wind speed $[km/h]$
V	Transverse shear force $[MN]$
Z	Plastic modulus $[m^3]$
α	Angle of the wedge in the horizontal direction $[^\circ]$
β	Angle of the wedge with the ground surface $[^\circ]$
γ	Unit weight $[kN/m^3]$
γ_w	Unit weight of water $[kN/m^3]$
δ	Lateral displacement $[m]$
μ	Mean value $[parameterdependent]$
ν	Poisson's ratio $[-]$
ρ	Density of air $[kN/m^3]$
σ	Standard deviation $[parameterdependent]$
σ'_0	Effective vertical stress $[kPa]$
ϕ	Friction angle $[^\circ]$
ψ	Dilation angle $[^\circ]$

CHAPTER 1

INTRODUCTION

1.1 Offshore wind turbines

With increasing population and limited energy sources, renewable energy gains importance for it conserves natural resources [106]. Wind energy, tidal energy, bio-fuels, solar energy, geothermal energy are some examples of renewable sources. Kinetic energy of wind power is transformed into rotational mechanical power, then mechanical power into electrical power through generators of wind turbines. Wind turbines have attracted the attention of researchers, companies, and governments in the past few decades. Therefore, the technology used for wind turbines is relatively more grown than other renewable energy sources [22]. According to the report published by Wind Europe [64] Europe now has 220 GW of wind energy capacity. Besides, new turbines to produce 105 GW of wind energy are expected to be installed by the end of 2025.

Wind turbines can be either onshore or offshore. Wind turbines consist of rotor-nacelle assembly (including blades, hub, and nacelle), tower, and foundation components. Blades, hub, nacelle, and tower are usually supplied by the turbine manufacturer [22]. Offshore wind turbines also have a transition piece and a substructure (Figure 1.1). The transition piece is a steel tube that supports the boat landings and ladders to reach the turbine. Mass of these components and the dimensions of the tower are required for the design. The manufacturer provides this information.

Wind turbines are generally installed in groups over an extensive area. A group of turbines is named as a wind farm. As an illustration, an offshore wind farm is presented in Figure 1.2. According to the report published by Wind Europe [90], the total wind energy capacity of Europe consists of 194 GW onshore (89 %) and 25 GW offshore

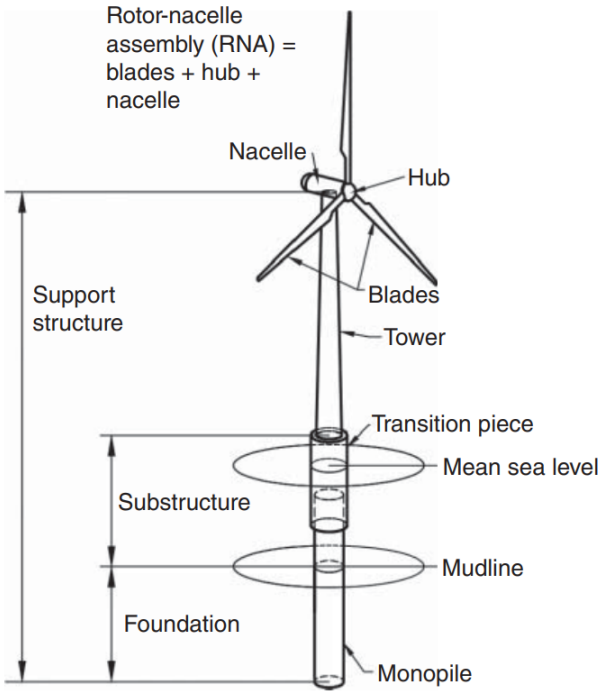

Figure 1.1: Wind turbine components [22]

(11 %). This gap is derived from the fact that wind turbines were constructed onshore initially. Yet, considering stronger and more consistent wind in the seas, no effects of topography on wind as compared to onshore turbines, noise and societal acceptance problems caused by onshore wind turbines, limitations and alternative uses for land area required for onshore turbines, offshore wind turbines have started to be installed [63]. Offshore wind farms are known to be more efficient in producing energy as the wind speed is higher than onshore [22].

Depletion of nearshore locations and seeking for more stable wind resources lead offshore wind farms to be constructed farther from shore, thus in deeper areas mostly [90]. In 2020, while the average power rating of new offshore turbines was 8.2 MW, new onshore wind turbines had only 40% of this value, 3.3 MW. In 2019, these values were 7.2 MW for offshore and 3.1 MW for onshore [89]. For offshore wind farms, the average values for distance to shore and water depth were 52 km and 44 m in 2020, respectively, and 59 km and 33 m in 2019, respectively [89, 90]. As more extensive and thus more efficient turbines are possible with offshore structures, the turbine capacity of offshore structures has risen by 16% every year between 2014 and

Figure 1.2: An offshore wind farm [7]

2019 [89]. Additionally, in the last decade, offshore wind farms have grown their sizes by 100% (from 313 MW in 2010 to 621 MW in 2019). These numbers indicate that both power generated from turbines and turbine sizes have increased.

Financing offshore wind is very complex and requires innovative structuring to reduce risks and ensure bankability [88]. Although offshore wind projects have high capital expenditures (often more than $2 billion) and risks due to the complexity of offshore construction, economic factors play a significant role in the energy market demand. As stated in the report published by Wind Europe, with the wind energy generated last year, it was possible to meet 16.4% of the EU and UK's electricity demand by onshore (13.4 %) and offshore (3 %) wind. This expected trend and an additional low expectation scenario in between 2021-2025 period are given in Figure 1.3 for onshore and offshore wind turbine installations. According to the figure, yearly expected added capacity is expected to rise. In spite of the fact that more than 70% of the new turbines are expected to be onshore [64], offshore engineering, particularly the offshore wind market, is gaining considerable and growing importance, both in terms of development and resource management [88].

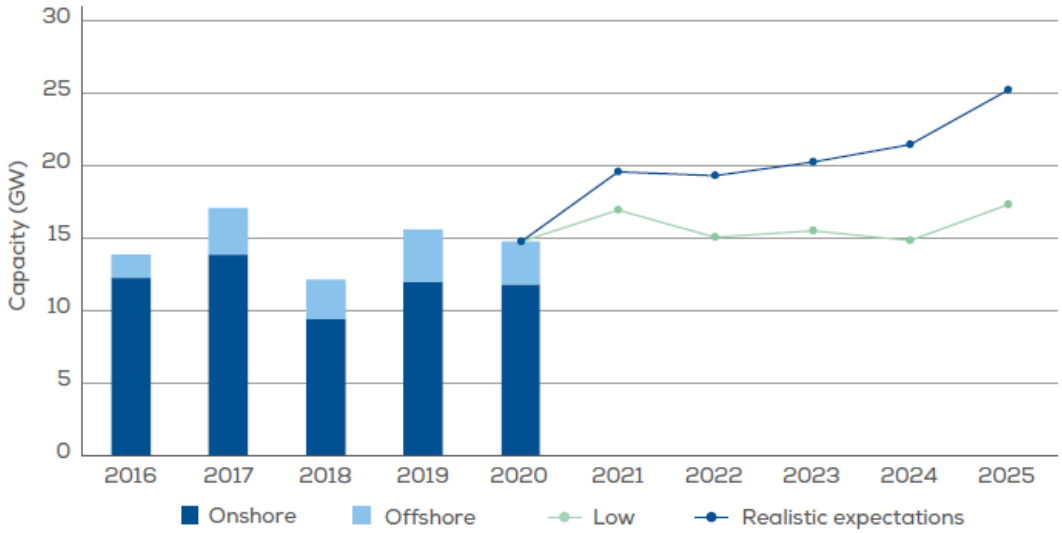

Figure 1.3: Offshore and onshore wind installation expectations for 2021-2025 [64]

In the design of an offshore wind turbine project, efficiency and economy are two of the essential points [68]. While the substructures of onshore wind turbines cost approximately 6.5% [56, 44] of the capital cost, the foundations of offshore wind turbines represent approximately 16 to 35% [56, 76, 22] depending on the size and the location of the structures, leading to be the second most expensive part of the structure after the turbine itself. If the installation stage is considered only, they are even the most costly elements [44]. For these reasons, enhancing economic efficiency is required for offshore wind turbines [56]. The wind power (P) can be calculated as is:

$$P = \frac{1}{2} C_p \rho A U^3 \tag{1.1}$$

where,

A_m : Area of rotor-swept area

C_p : The power coefficient

ρ : the density of air

U : wind speed

From the equation, it can be interpreted that for a given wind speed and air density, the power can be increased by either improving the power coefficient or enlarging rotor-swept area [22]. Because of the facts that 1) the swept area is proportional to the square of the rotor diameter and 2) the theoretical maximum power coefficient is 0.59 (for a properly designed wind turbine [21], it is usually around 0.35-0.45), it is more logical to increase the rotor diameter than investing in blades for enhancing the power coefficient [22]. Conversely, increasing the rotor diameter requires taller towers, larger nacelle, and stronger foundations.

There are various foundation types available for offshore wind turbines, including grounded (fixed-bottom) systems such as gravity-based, monopiles, suction caissons, and jackets and floating systems such as tension leg platform and spar buoy [22]. Simple sketches for these foundation types can be seen in Figure 1.4. Among these various foundation types, monopile is the most widely employed foundation type for offshore wind turbines around the world placed at shallow to intermediate water depths [68]. According to Wind Europe [90], monopiles have a ratio of 80.5% of all wind turbine foundations installed in 2020. The overall percentage of this type of substructures is 81.2% with 4,681 units, including both with and without grid installations. Although in Figure 1.4 typical water depths for monopiles are indicated, deeper waters such as 50 m [112] is possible and 60 m is being considered [6]. The distribution of foundation substructures among foundations installed in 2020, including both with and without grid installations, is given in Figure 1.5. As can be interpreted from the figure, it represents the majority of recent wind turbine foundations. The remarkable simplicity in design and production stages is believed to be the reason for this prevalence [62].

Monopile is made of an open-ended hollow steel tube with commonly a diameter of 3.5-6 m, length of 30-40 m [22], slenderness ratio between 2 and 10 [5]. Different steel grading can be selected depending on the design. An example monopile structure cross-section is presented in Figure 1.6 for better comprehension. The loads acting on a monopile are structural loads, wind loads, and loads derived from waves and currents. The typical mass of a structure is 600 to 1500 t. These structures are predominantly subjected to cyclic lateral loads. An example showing the loads on a monopile structure is given in Figure 1.7. The monopile resists these forces by its

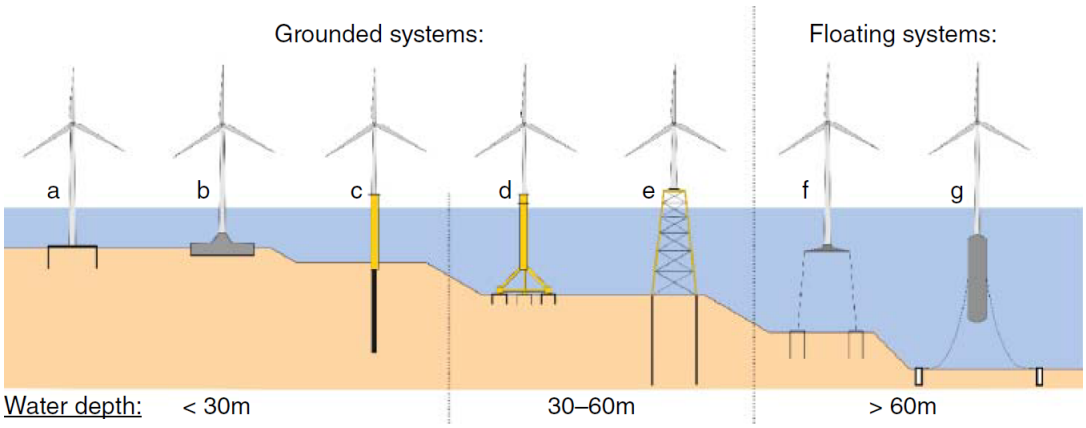

Figure 1.4: Different foundation types for offshore wind turbines [22] (a) bucket/suction caisson, (b) gravity-based, (c) monopile, (d) tripod on bucket/suction caisson, (e) jacket/lattice structure, (f) tension leg platform, and (g) spar buoy floating concept

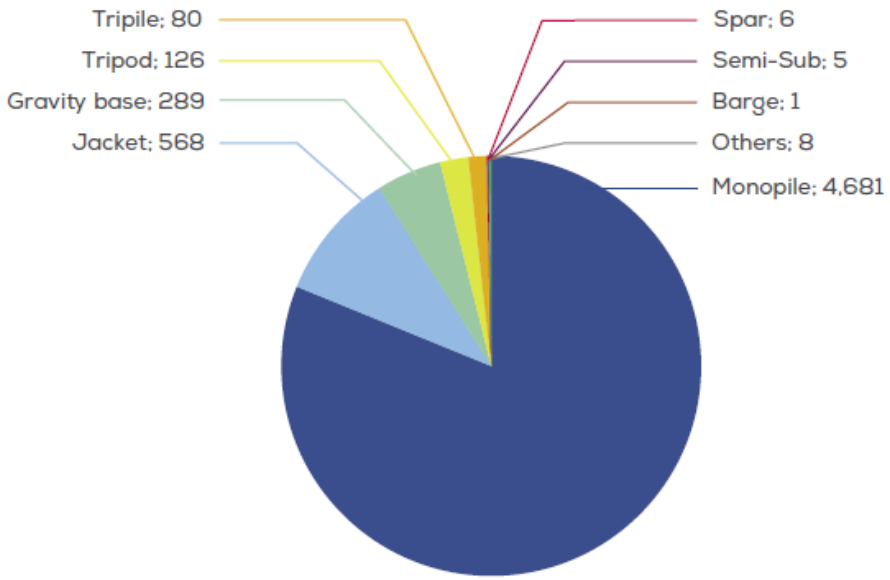

Figure 1.5: The distribution of the substructures among the foundations installed in 2020 [90]

embedment into the seafloor.

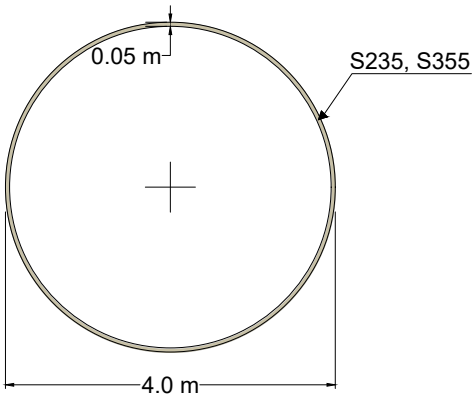

Figure 1.6: Example monopile structure cross section

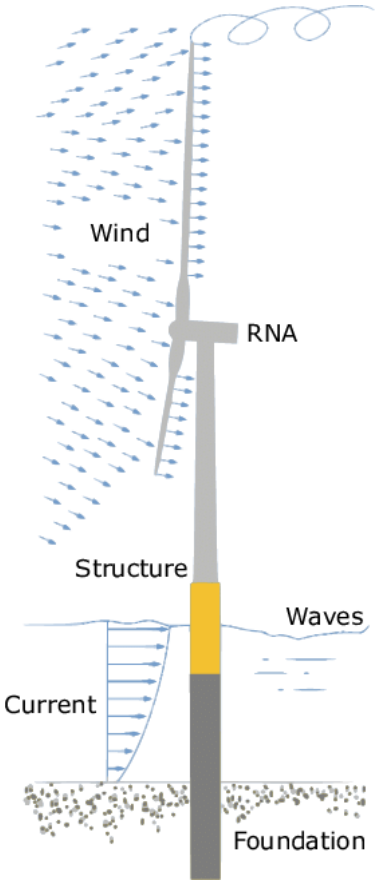

Figure 1.7: Loads on a monopile structure [85]

In offshore wind farms, the typical spacing between individual turbines is 3 to 10 times the rotor diameter of the turbines, depending on the prevailing wind direction [22]. That being the case, small to medium scale wind farms usually cover 20 km

x 65 km area, which is quite large. This fact causes a remarkable variation in the subsurface and geotechnical conditions. This variation makes it necessary to design each turbine, thus each foundation individually. Nevertheless, considering the economic aspects of projects, it may not be the case. Figure 1.8 shows five different monopile locations in the given geological model located at The Westermost Rough Offshore Wind Farm [61]. As can be interpreted from the figure, each monopile come across different geological formations such as Holocene Surface Deposits, Hc, Botney Cut Formation, BC, Boulders Bank Formation, Bo, Swarte Bank Formation, Sw, and chalk, Ch.

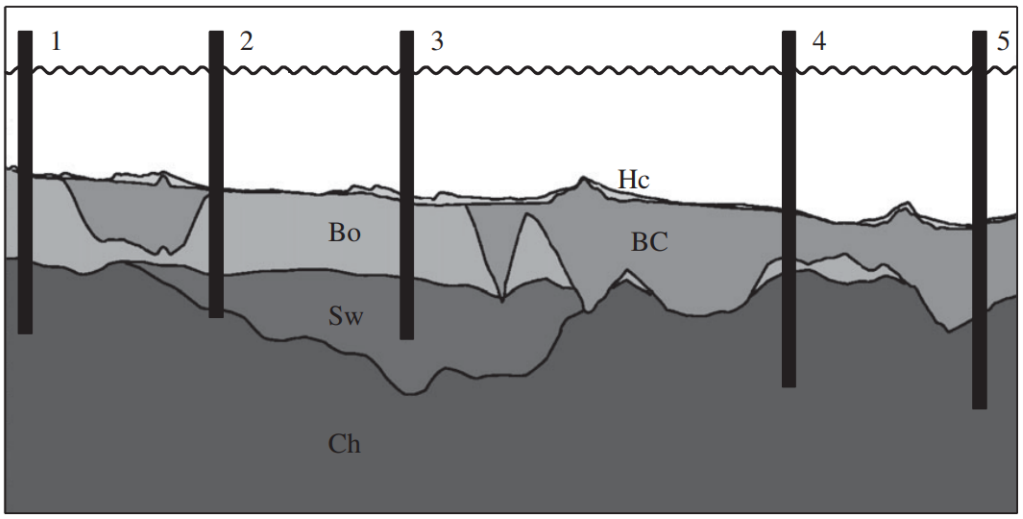

Figure 1.8: Geological cross section for 5 different monopiles at The Westermost Rough Offshore Wind Farm [61]

According to Cai et al. [28], even if a site-specific CPT test is conducted at a planned monopile location, the soil strength may be variable in the lateral direction (in a plane) at a given depth. This may be more important, especially for large diameter piles. Then, the statistics of the geotechnical investigations available could be used to collate, compare, and confirm the geotechnical conditions estimated. A horizontal soil profile at a certain depth, at a monopile location, is given in Figure 1.9, demonstrating the soil strength variation in a plane. The footprint of a large diameter pile is indicated, at the center of which the CPT location is pointed with a dot on the figure. How the lateral distribution of soil strength is obtained, or the depth at which this data is obtained, are not explained in Cai et al. [28]. However, there are examples of

such studies employing spatial variability via random field theory and scale of fluctuation [42] as well as using other geostatistics-based probabilistic techniques such as Bayesian Kriging in spatial interpolation [4, 74]. It can be visualized from Figure 1.9 that even for a small-diameter pile, there would be some variation in soil properties in a plane, as well as with depth.

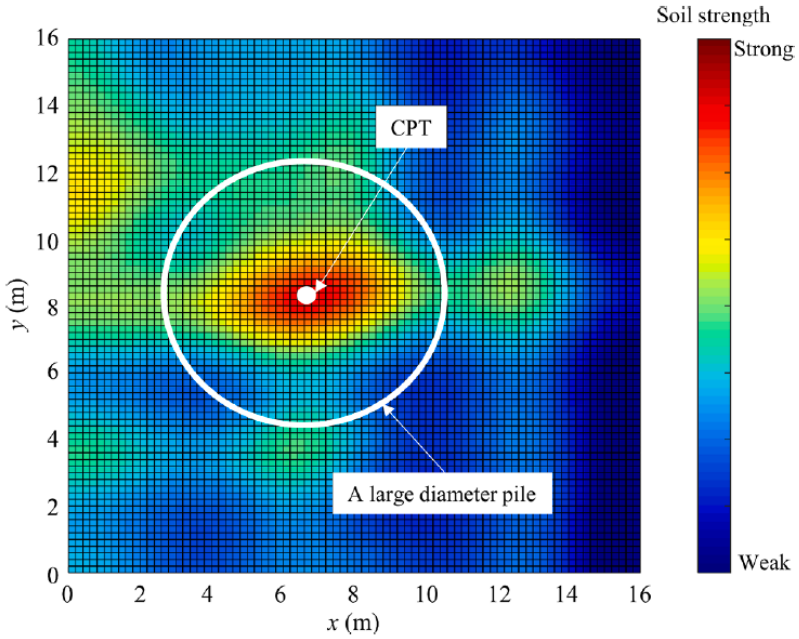

Figure 1.9: A horizontal soil profile with variability of soil strength (depth unknown) [28]

1.2 Research question and objectives of the study

The research question of this study is "how to account for uncertainty in estimating soil parameters in offshore monopile design". In order to answer this question, the main aim is set to estimate the probability of unsatisfactory performance (unsatisfactory performance = unsatisfactory cases of analyses / all cases of analyses %), taking into account variations in soil material properties. In this regard, the objectives of this thesis can be categorized as:

- quantifying variation of soil material properties by implementing coefficients of variation values (COV),

- designing and evaluating the performance of a monopile off the shore of Belgium via Monte Carlo simulation

In the light of the previous studies in the literature, this thesis is formed and tailored. The novelty of this thesis is a site-specific statistical analysis. Therefore, it aims to give more realistic results on interpreting the probability of unsatisfactory performance of a monopile in sand. It should be noted that though the magnitude of model uncertainty is hard to assess, it can be easily included in statistical analyses [11]. Model uncertainty is also claimed to be presented by the capacity calculation methods [28]. Therefore, for this study, it is not a point of concern. Besides, model uncertainty also exists for a deterministic analysis.

1.3 Scope

This chapter introduced renewable energy technologies with an emphasis on offshore wind turbines. Available design methods and guidelines are presented in Chapter 2. Chapter 2 also presents background for probabilistic evaluation of soil properties. The methodology to calculate the performance of a monopile under static loading conditions by Finite Element Method (FEM) and its verification by a case study are given in Chapter 3. Probabilistic analysis approach to account for the variability is discussed in Chapter 4. Conclusions and future recommendations are presented in Chapter 5.

CHAPTER 2

BACKGROUND

2.1 Introduction

This chapter aims to introduce the available knowledge on the topic and soil properties collected from different sources. Initially, analysis methods, as one of the 1 Dimensional (1D) analysis methods, and the p-y method, its origin, and development so far will be explained for cohesionless soils. In a similar fashion, the axial load-displacement curves (t-z and Q-z curves), which are utilized for the analysis, are introduced. The general presentation of these three types of curves is given in Figure 2.1. Later, variability and probabilistic evaluation of soil parameters are introduced. Finally, the soil parameters gathered from the literature and their variability are presented.

2.2 Analysis methods

Offshore wind turbines should be designed to withstand high wind speeds of 50-year mean recurrence interval without any damage [22]. In order to evaluate whether the monopile structure is safe in terms of statics and serviceability, related forces, stresses, and moments acting on the system with the deflections need to be examined.

The procedures applied for the offshore wind power industry initially followed the technology utilized by offshore oil and gas structures [22]. Yet, there are some differences in the design of offshore oil and gas structures and offshore wind turbines in terms of structure size, thus natural frequencies and pile behavior under loading.

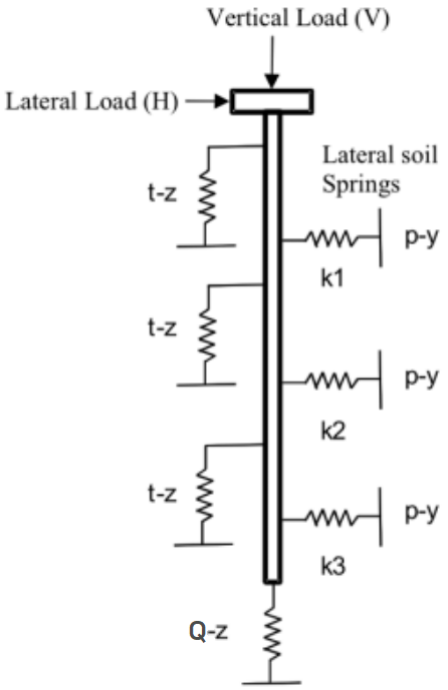

Figure 2.1: Load-displacement curves [100]

There are 1 Dimensional (1D) and 3 Dimensional (3D) methods that can be utilized to evaluate the safety of the design. Both approaches have their advantages and disadvantages. Available 1D methods are quite simple; however, they may be insufficient to reflect realistic structural behavior. Finite element or finite difference methods are usually employed for these analyses [11]. 1D methods include the p-y method, PISA design method, and the macro element model. On the other hand, 3D methods are more advanced. 3D methods are usually finite element methods with proper soil constitutive model assignment.

The most widely known and used 1D (beam-spring) method is the p-y method, where independent Winkler springs are attached to the 1D beam element to account for the soil-structure interaction throughout the pile length. In current industry design, this method is practiced. An example sketch for the technique is given in Figure 2.2(a). Spring properties can be assessed according to American Petroleum Institute (API) [101] and Det Norske Veritas - Germanischer Lloyd (DNV-GL) [40] guidelines. This model is fast, and various commercial and noncommercial software is available. However, these springs are derived for relatively small diameter piles and may be

inadequate to reflect the soil-structure interaction for large diameter piles. This inadequacy is derived from two different aspects. Firstly, as the available lateral displacement - lateral force (p-y curves) were initially semi-empirically derived to reflect small-diameter oil and gas industry piles [13], they are limited to reflect the behavior of large-diameter offshore monopiles. Secondly, as structural behavior under loading plays an important role, whether the structure is slender or rigid is essential to decide on the method. As the p-y method only uses simplified springs in the lateral and axial direction, it can not represent the actual behavior of a large-diameter pile. Whereas oil and gas industry piles translate loads laterally without showing a rotation, offshore monopiles are free headed and can rotate [22]. Additional moment springs should be added to the system to better approximate the actual deformed shape. As the current p-y method does not propose these curves, it is poor in representing the structure. In the literature, the discrepancies between the actual monopile behavior and results by the p-y method were discussed [69, 41]. Although some scaling/correction factors account for these problems, it requires further improvements. There are various papers in the literature to improve p-y method in some assumptions [38, 105].

PISA design method [26, 27] represents the soil with distributed loads and moments, base shear, and base moment. An example sketch for the method is given in Figure 2.2(b). Analysis results provide similar results to 3D analysis results, and the computational time for the technique is low. However, the application of the method is only possible with the software PLAXIS MoDeTo.

The macro-element model considers the soil-structure interaction by nonlinear load-displacement curves located at a point between the foundation and the rest of the structure, typically located at seabed [37]. An example sketch for the method is given in Figure 2.2(c). According to Page et al. [85], this method provides accurate foundation stiffness and damping. However, the quality of the results is directly linked to the accuracy of the load-displacement curves. These curves can be determined by 3D Finite Element Analysis or calibrated by model tests. In order to reproduce the actual pile behavior by 3D FEM, a proper constitutive model should be assigned to the soil. Likewise, experimental results from model tests can be used to calibrate the model. Whereas the p-y method has distributed springs along the pile, this method computes the structure's response at one point only. This fact indicates fewer degrees

of freedom for the system and easier overall stiffness and damping response calculation. This model also considers side and base shear soil resistance, which is neglected in the p-y method.

On the other hand, 3D methods represent this interaction better. Yet, they are computationally costly and require a better understanding of available soil models. This method defines the soil as a continuum via interface elements. An example sketch for the method is given in Figure 2.2(d). There are several different constitutive models to reflect soil behavior. Some of them are Mohr-Coulomb (MC), Hardening Soil (HS), Hardening Soil for small strain stiffness increase (HSsmall), Hypo Plastic (HP) [5]. While clays are examined under undrained conditions, sands are examined under drained conditions. There are also advanced material models such as UDCAM-S model to represent cyclic degradation in which strains are accumulated, and loosening and re-compaction are observed.

2.3 p-y curves

Deformations along the pile depend on the pile and surrounding soil type. With an applied loading (which could be seismic, static, or dynamic), an exchange of mutual stress is expected in the system. This relation is named as soil-structure interaction in the literature. The p-y method has been developed to reflect this interaction for lateral loading. The p-y curves are lateral load-displacement curves where independent Winkler springs are attached to the 1D beam element throughout the pile.

The initial stiffness of these curves is affected by 1) the shear strain, 2) confining pressure [95]. However, as there are complex strain fields around the pile, obtaining this stiffness is not trivial. Moreover, while lateral stress is expected to be zero at the surface, approximately linear increase is expected with increasing depth.

The starting point for the methods to solve laterally loaded pile response was about 65 years ago, and it includes the Terzaghi curves [108], and p-y curves [92, 78]. Then, some assumptions are made to calculate the ultimate soil resistance, p_u. This analytical solution is employed in current p-y methods. Reese et al. [93], American Petroleum Institute (API) [101], and Det Norske Veritas - Germanischer Lloyd (DNV-

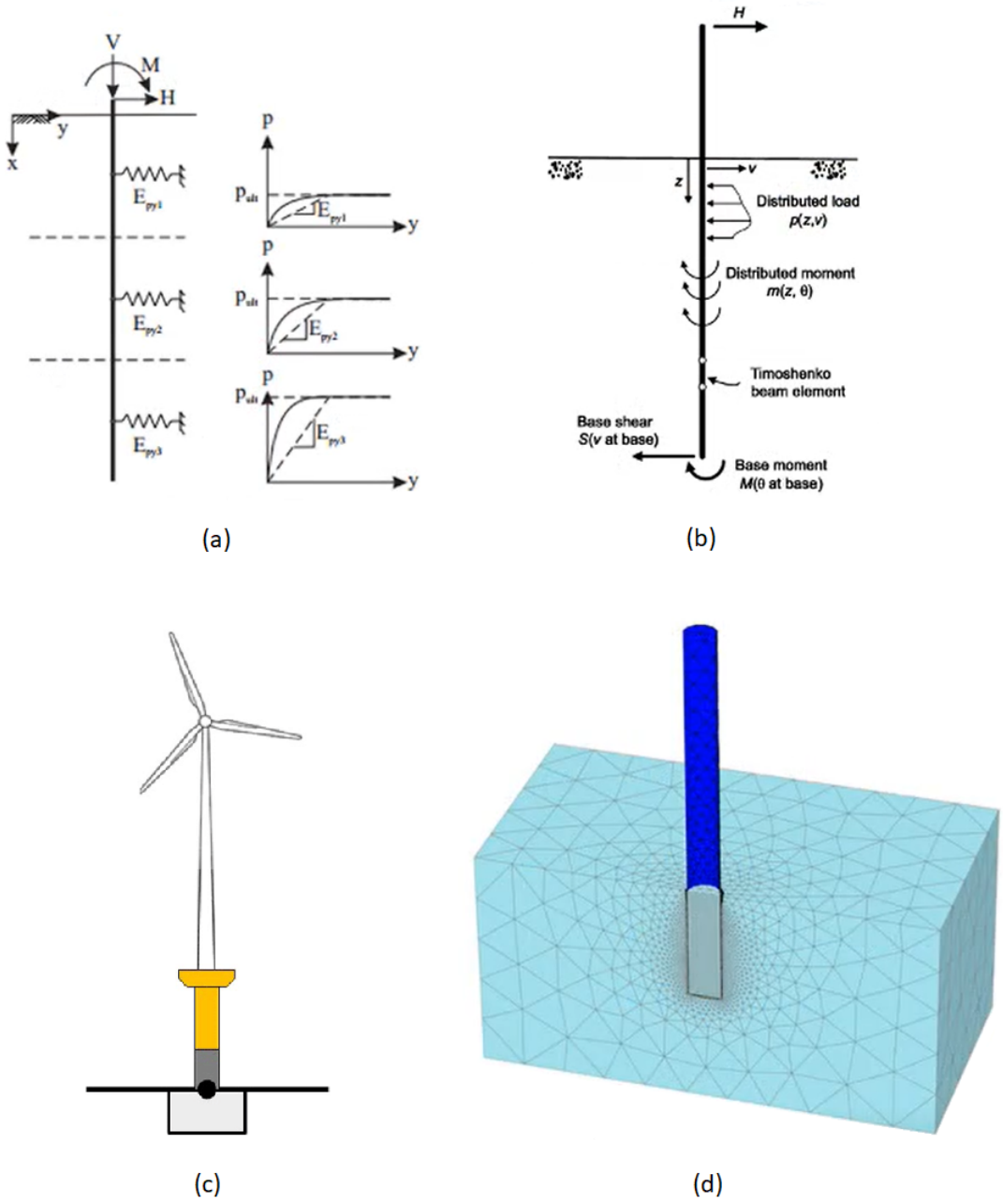

Figure 2.2: Basic sketches for analysis methods (a) p-y method, (b) PISA design method, (c) macro element model and (d) 3D FEM method [5, 20]

GL) [40] guidelines presented this p-y method with minor nuances. LPile software has also discussed this method with some improvements on the initial modulus of subgrade reaction in their technical report [95].

2.3.1 Terzaghi curves

Terzaghi recommended stiffness coefficients to be used in Equation 2.1 to calculate the soil modulus with changing depth. He recommended using these coefficients until the depth where the soil resistance calculated equals one-half of the ultimate bearing stress. The recommended coefficients are given in Table 2.1.

$$E_s = kz \tag{2.1}$$

where,

k : constant for soil modulus

z : the depth of the spring below ground surface

Table 2.1: Terzaghi's recommended modulus values for laterally loaded piles in sand [108]

Relative Density	k for Dry/Moist Sand (MN/m^3)	k for Submerged Sand (MN/m^3)
Loose	0.95 - 2.8	0.53 - 1.7
Medium	3.5 - 10.9	2.2 - 7.3
Dense	13.8 - 27.7	8.3 - 17.9

However, now these numbers are known to be conservative. Besides, these coefficients may be recognized to reflect secant modulus instead of initial modulus [95]. These values are based on a literature review conducted in the early 1950s. Therefore, other values based on soil investigations and load tests should be considered instead of these coefficients. Later, Terzaghi also ceased the recommendation of these values.

2.3.2 Analytical solutions for ultimate resistance

The method to calculate the ultimate soil resistance, p_u, for piles in sand is different depending on the depth below the ground surface. Therefore, at a given depth, it is recommended to examine both shallow and deep ultimate soil resistance and use the smaller one in the calculations [101].

For the shallow ultimate soil resistance, the geometry of a wedge that satisfies Mohr-Coulomb failure condition is given in Figure 2.3. The total lateral force, F_{pt}, is the difference between active, F_a, and passive, F_p, forces acting on the pile (see Figure 2.3(c)). The active pressure can be computed by use of Rankine theory. The passive pressure can be computed by the use of the Mohr-Coulomb failure condition, assuming that failure occurred on the sloping wedge surface (AEFB) and vertical wedge side planes (ADE and BCF) (see Figure 2.3(a)).

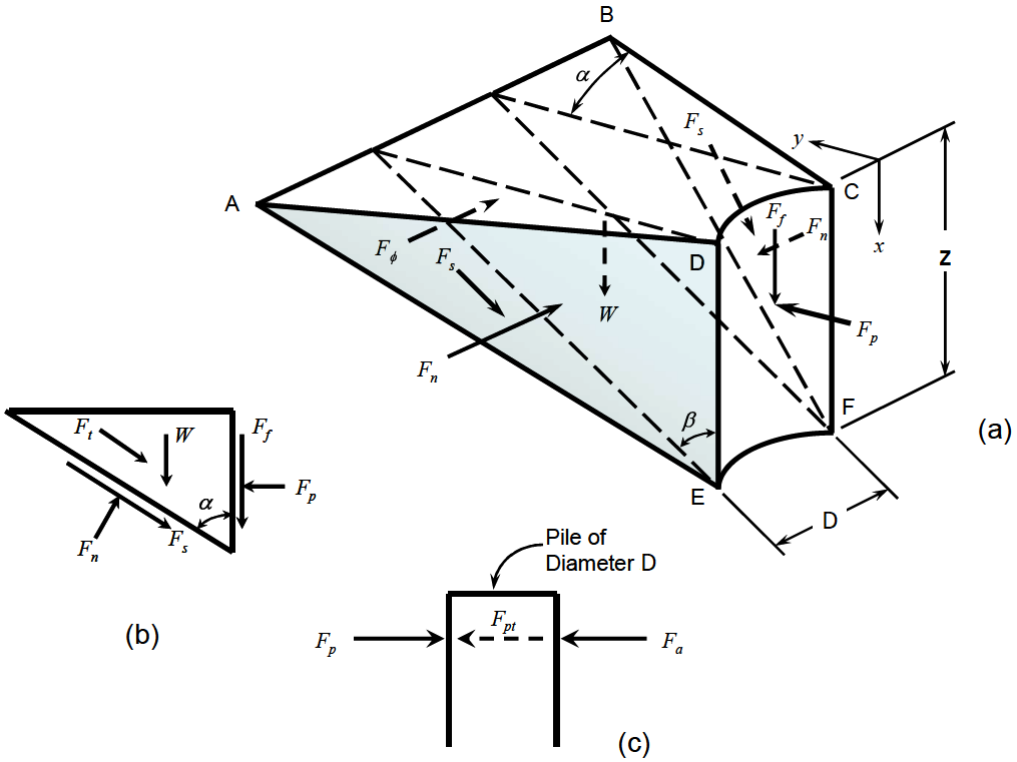

Figure 2.3: Passive wedge failure assumption for piles in sand [95]

Note that β is the angle between the wedge and the ground surface, and α is the angle of the wedge in the horizontal direction. For α, according to conducted laboratory

experiments [24], it is suggested to use $\phi/3$ to $\phi/2$ for loose sands and up to ϕ for dense sands. The approximated formulas for these angles by the guideline are given in Equation 2.2.

$$\alpha = \frac{\phi}{2}\,, \qquad \beta = 45^\circ + \frac{\phi}{2} \tag{2.2}$$

The active force, F_a, is given in Equation 2.3 where K_a is the coefficient of active earth pressure as is given in Equation 2.4.

$$F_a = \frac{K_a \gamma D H^2}{2} \tag{2.3}$$

$$K_a = \frac{1 - sin\phi}{1 + sin\phi} \tag{2.4}$$

The resultant forces are given in Figure 2.3(b). The equilibrium equations are solved in x and y directions with these assumptions: 1) the friction force at the pile and soil interface is zero, and 2) the water table is constant and within the wedge. Following, the passive force, F_p, is quantified as is given in Equation 2.5 remarking K_0 is the coefficient of earth pressure at rest and can be assumed as 0.4 [101]. Moreover, z is the height of the wedge.

$$\begin{aligned} F_p = \gamma\, z^2 \Bigg[\frac{K_0\, z\, tan\phi\, sin\beta}{3\, tan(\beta-\phi) cos\alpha} + \frac{tan\beta}{tan(\beta-\phi)} \left(\frac{D}{2} + \frac{z\, tan\beta\, tan\alpha}{3} \right) \\ + \frac{K_0\, z\, tan\beta}{3} (tan\phi\, sin\beta - tan\alpha) \Bigg] \end{aligned} \tag{2.5}$$

If the active force, F_a, is subtracted from the passive force F_p, and differentiated with respect to depth, the ultimate soil resistance for shallow depths p_{us} can be found as is given in Equation 2.6.

$$\begin{aligned} p_{us} = \gamma\, z \Bigg[\frac{K_0\, z\, tan\phi\, sin\beta}{tan(\beta-\phi) cos\alpha} + \frac{tan\beta}{tan(\beta-\phi)} (D + z\, tan\beta\, tan\alpha) \\ + K_0\, z\, tan\beta\, (tan\phi\, sin\beta - tan\alpha) - K_a\, D \Bigg] \end{aligned} \tag{2.6}$$

For the deep ultimate soil resistance, p_{ud}, the assumed soil failure mode is given in Figure 2.4. In the figure, assumed pile movement is given. For this failure mode, lateral flow around the pile is expected. Therefore, the stress at the back of the pile (indicated in the figure as σ) should be smaller than the minimum active earth pressure. In this case, soil fails by slumping. The related formula for this condition is given in Equation 2.7.

$$p_{ud} = K_a\, D\, \gamma\, z\, (tan^8\beta - 1) + K_0\, D\, \gamma\, z\, (tan\phi\, tan^4\beta) \tag{2.7}$$

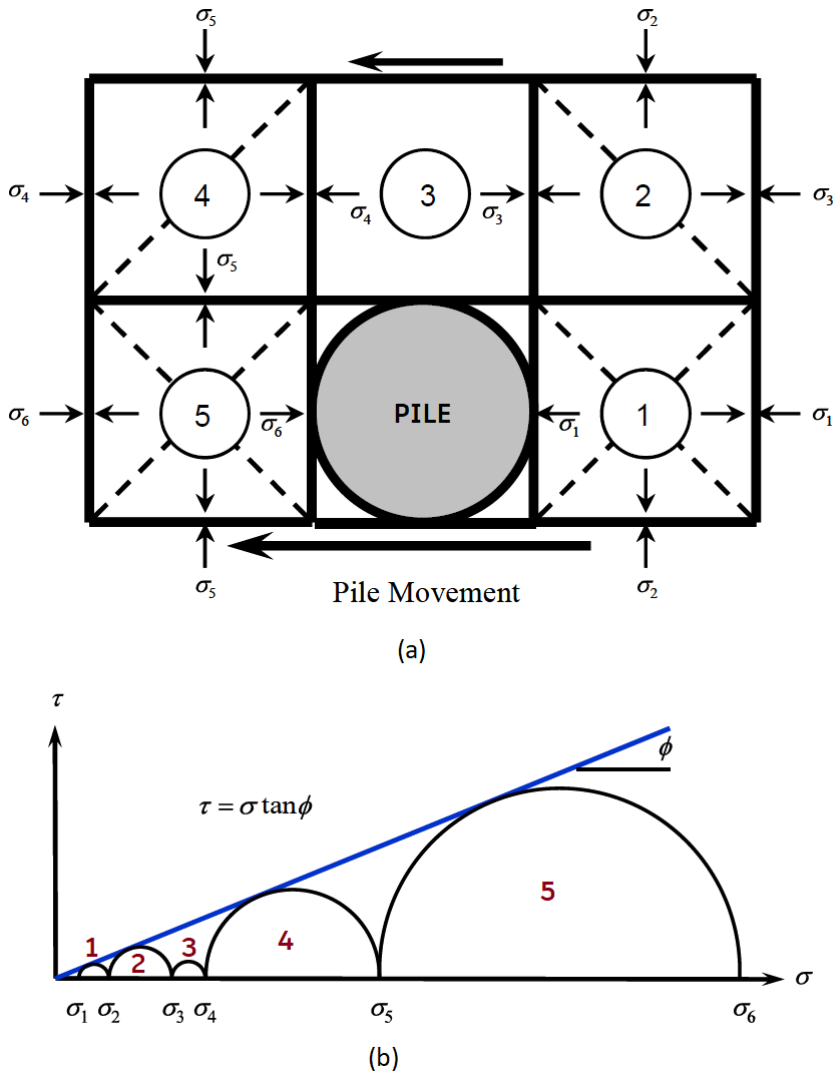

Figure 2.4: Passive wedge failure assumption for piles in sand [95]

2.3.3 API curves

API [101] suggests offshore structure design standards on the basis of design assessments and requirements of offshore structures utilized by the petroleum and natural gas industries all around the world. API presented the p-y method for small diameter piles. The guideline suggests that finite element modeling should confirm the results for complex situations because of the fact that the finite element method is more advanced. According to the guideline, for the p-y method, the lateral soil resistance - displacement curves for sand can be approximated by Equation 2.8.

$$p = A\, p_u\, tanh\left[\frac{k\, z}{A\, p_u} y\right] \tag{2.8}$$

where,

A : cyclic or static loading condition factor

k : initial modulus of subgrade reaction

p : lateral soil resistance at a given depth, z

p_u: the ultimate soil resistance

y : lateral deflection at a given depth, z

z : the depth of the spring below the mudline level

For the calculation of the ultimate soil resistance, p_u, the ultimate soil resistance for shallow depths p_{us} and deep depths p_{ud} should be evaluated. The minimum of these two is employed as p_u. In spite of the fact that the guideline uses the same assumption for the analytical solution for the ultimate soil resistance, which is given in previous sections, it defines some coefficients (C_1, C_2, and C_3) for simplification. Formulas related to p_{us} and p_{ud} are given in Equation 2.9, and 2.10, respectively.

$$p_{us} = (C_1\, z + C_2\, D)\gamma'\, z \tag{2.9}$$

$$p_{us} = C_3\, D\, \gamma'\, z \tag{2.10}$$

These coefficients are derived from Equations 2.6 for shallower depth and Equation 2.7 for deeper depths. Whereas C_1 and C_2 are the coefficients for shallow depth ultimate soil resistance, C_3 is a coefficient for ultimate soil resistance at deeper depths. The equations for these coefficients are given in Equations 2.11, 2.12, and 2.13, respectively.

$$C_1 = \frac{K_0\, tan\phi\, sin\beta}{tan(\beta-\phi)cos\alpha} + \frac{tan^2\beta\, tan\alpha}{tan(\beta-\phi)} + K_0\, tan\beta\, (tan\phi\, sin\beta - tan\alpha) \tag{2.11}$$

$$C_2 = \frac{tan\beta}{tan(\beta-\phi)} - K_a \tag{2.12}$$

$$C_3 = K_a\, (tan^8\beta - 1) + K_0\, (tan\phi\, tan^4\beta) \tag{2.13}$$

There also exists a chart presented by the guideline for the coefficients, and it is given in Figure 2.5

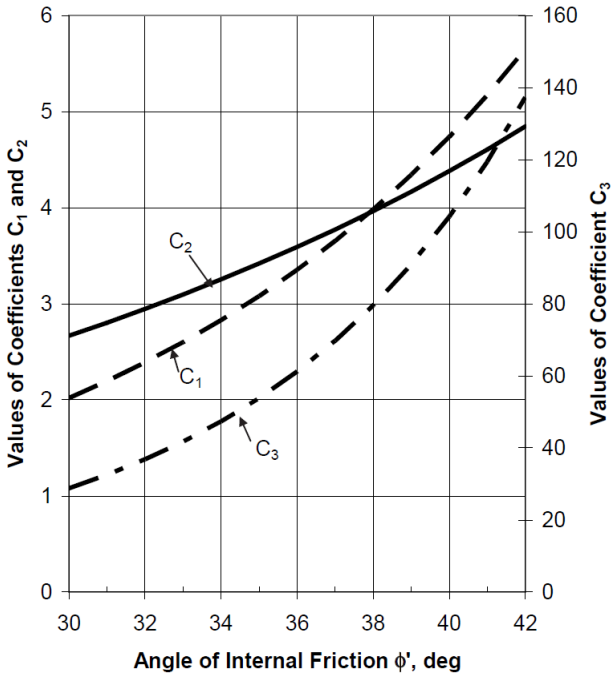

Figure 2.5: C_1, C_2, and C_3 coefficients versus friction angle [101]

On the other hand, A is 0.9 for cyclic loading and can be calculated as is given in Equation 2.14 for static loading.

$$A = \left[3 - \frac{0.8\,z}{D}\right] \geq 0.9 \tag{2.14}$$

For the initial modulus of subgrade reaction, k, suggested values by API guideline are given in Table 2.2.

Table 2.2: Friction angle versus initial modulus of subgrade reaction [101]

$\phi(^\circ)$	k (MN/m^3)
25	5.4
30	11
35	22
40	45

However, the database used for the calibration of the method consists of free-head tests on piles in clean sands having a friction angle between 34° and 42°. These friction angle values were determined by drained triaxial tests, shear box tests, or correlations with in situ tests. If extrapolation is needed to calculate the initial modulus of subgrade reaction based on the data given in Table 2.2, extra caution is required. Especially sands, having friction angles less than 30°, require further investigation. In this case, conducted laboratory test results should be critically examined to check whether there exists an unexpected behavior or not. In addition, the sample should be inspected to check the fraction of cohesive soil in it. Both of these two cases could require a different formulation for the curves [101].

2.3.4 Reese, et al. (1974) procedure curves

For cyclic and short term static loading, Reese et al. [93] proposed lateral load-displacement curves. The main characteristic shape of these curves is given in Figure 2.6. As can be interpreted from the figure, a curve consists of four parts.

- $y = 0$ to $y = y_k$: linear portion with slope kz
- $y = y_k$ to $y = y_m$: parabolic portion
- $y = y_m$ to $y = y_u$: linear portion with slope m
- $y = y_u$ to $y = y_\infty$: constant portion where $p = p_u$

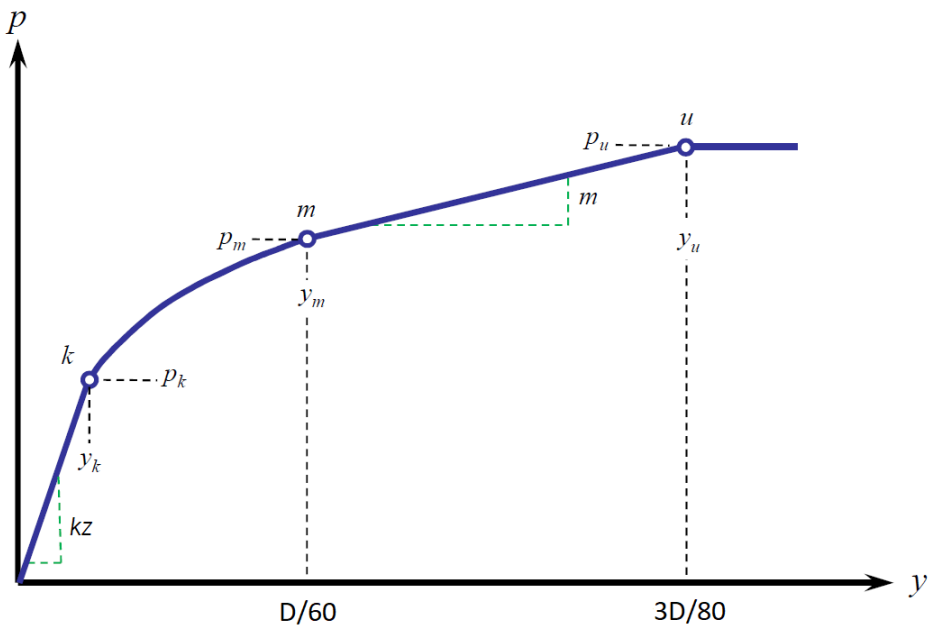

Figure 2.6: Characteristic shape of laterally loaded piles in sand [93]

where

D : diameter of the pile

k : initial modulus of subgrade reaction

p : lateral soil resistance at a given depth, z

p_u: the ultimate soil resistance

y : lateral deflection at a given depth, z

z : the depth of the spring below the mudline level

The ultimate soil resistance is calculated according to analytical solutions for ultimate resistance. As it is explained in the previous sections, it is the smaller value of the

ultimate soil resistance for shallow depths p_{us} and deep depths p_{ud}. In order to calculate the soil resistance, in line with the API guideline, α and β values should be taken as is given in Equation 2.2 (both in degrees). Compatibly, K_0 is assumed as 0.4, and K_a definition is as given previously in Equation 2.4. However, this method requires that the calculated minimum value should be multiplied by A_s for static loading and A_c for cyclic loading to get the ultimate resistance p_u. Values for these coefficients are given in Figure 2.7(a). Moreover, y_u is 3/80 times the diameter of the pile. In a same manner, p_m is calculated by multiplying p_s by B_s for static loading and B_c for cyclic loading. Values for these coefficients are given in Figure 2.7(b). Furthermore, y_m is 1/60 times the diameter of the pile.

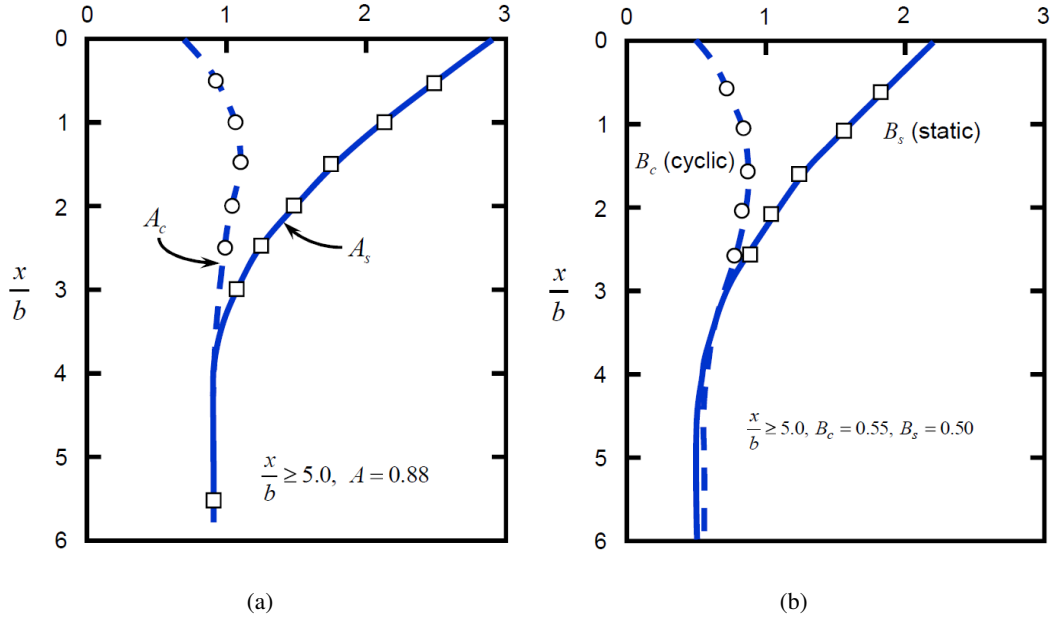

Figure 2.7: Values for: (a) A_s and A_c, (b) B_s and B_c [93]

For the first linear portion of the curve where the initial modulus of subgrade reaction applies, k values are given in Table 2.3. The slope can be found by multiplying the k value to the depth of the p-y spring from the ground surface. The right endpoint of this portion, y_k, is calculated as given in Equation 2.15.

$$y_k = \left[\frac{C}{kz}\right]^{\frac{n}{n-1}} \quad where \quad C = \frac{p_m}{y_m^{1/n}} \quad and \quad n = \frac{p_m}{my_m} \tag{2.15}$$

The parabolic part may or may not exist depending on the k value. If it is too low,

Table 2.3: Reese et al.'s recommended modulus values for laterally loaded piles in sand below water table [93]

Relative Density	k for Dry or Moist Sand (MN/m^3)	k for Submerged Sand (MN/m^3)
Loose	6.8	5.4
Medium	24.4	16.3
Dense	61.0	34.0

then y_k will be greater than y_m; thus, there will be no parabolic part. If there exists a parabolic portion, then the equation given in Equation 2.16 should be used to plot it.

$$p = Cy^{1/n} \tag{2.16}$$

2.3.5 DNV-GL curves

DNV-GL [40] provides suggestions for soil investigations, prediction of soil capacity, and guidance for modeling and analysis of offshore foundations. Yet, these curves were calibrated with long slender jacket piles having diameters smaller than 1.0 m. Therefore, the method is not valid for large-diameter piles; however, it is still being used in monopile design practice worldwide. For cohesionless soil, DNV-GL presents a p-y curve model adopted from API guideline [101]. The only difference is handling the initial modulus of subgrade reaction values. DNV-GL guideline suggests two different equations. The first one is based on the sand layer's relative density, D_r. The related equation is given in Equation 2.17. The other approach is based on friction angle values of the sand layer. The related expression is given in Equation 2.18. Both equations give results in MN/m^3. While the first expression is valid for the range of D_r, which is 0 to 100%, the second expression is valid for friction angle values between 34° to 42°.

$$k = 2.21 + 0.0584D_r + 0.0166D_r^2 \tag{2.17}$$

$$k = 226 - 20.6\phi + 0.423\phi^2 \tag{2.18}$$

2.3.6 LPile curves

LPile is a well-known software by Ensoft Inc which can analyze laterally loaded piles. The behavior of a beam column with nonlinear support is reflected by a differential equation. LPile offers both API [101] and Reese et al.'s [93] methods. The users expected to define the initial modulus of subgrade reaction. However, if it is not defined, in other words, if the actual data is not available, then the program suggests a value for fine sands. As is presented on its technical manual [101], for piles in sand above and below water table, equations for the initial subgrade reaction are given in Equation 2.19 and 2.20, respectively in MN/m^3. The equations are valid between 27.6° to 45° of friction angle. k value at friction angle of 0° is 0 MN/m^3. Whereas k value is linear between 0° to below 27.6°, the value corresponding to 45° is assigned as constant above 45° of friction angle. Related sketch is given in Figure 2.8.

$$k = 0.4168\phi^2 - 8.1254\phi - 83.664 \tag{2.19}$$

$$k = 0.0166\phi^3 - 1.5526\phi^2 + 58.43\phi - 769.18 \tag{2.20}$$

2.4 t-z curves

API guideline [101] suggests a table for z/z_{peak} versus t/t_{max} tables for both clays and sands. The table for clay and sand layers is given in Table 2.4. As a typical value for z_{peak}, one percent of the pile outer diameter as is mentioned in the guideline (i.e. $z_{peak}/D = 0.01$) is recommended for routine design purposes. On the other hand, t_{max} is the maximum shaft friction, and it is the product of maximum unit shaft

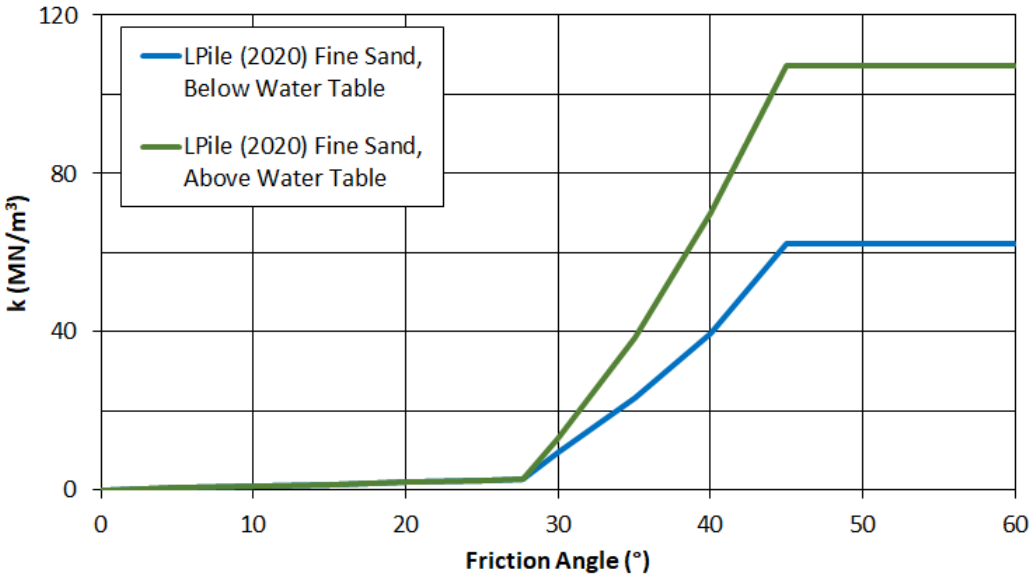

Figure 2.8: Initial modulus of subgrade reaction for fine sands suggested by LPile

friction and side area of the pile. Maximum unit shaft friction is calculated as is given in Equation 2.21.

Table 2.4: Definition of t-z curves [101]

z/z_{peak}	t/t_{max} for clays	t/t_{max} for sands
0.16	0.30	0.30
0.31	0.50	0.50
0.57	0.75	0.75
0.80	0.90	0.90
1.0	1.00	1.00
2.0	0.70-0.90	1.00
∞	0.70-0.90	1.00

$$f(z) = \beta\sigma_0'(z) < \ limiting\ shaft\ friction \tag{2.21}$$

$\sigma_0'(z)$ is effective vertical stress at depth z. Furthermore, limit values and shaft friction

factor, β, can be found in Table 2.5.

Table 2.5: Design parameters for t-z curves [101]

Relative Density (-)	Shaft Friction Factor (kPa)	Limiting Shaft Friction
medium dense	0.29	67
medium dense to dense	0.37	81
dense to very dense	0.46	96
very dense	0.56	115

The relative density definitions are as follows:

- **Very loose:** 0 – 15 %
- **Loose:** 15 – 35 %
- **Medium dense:** 35 – 65 %
- **Dense:** 65 – 85 %
- **Very dense:** 85 – 100 %

In order to transform given friction angle to relative density, the graph given by the previous API guideline is employed [57]. Related chart is given in Figure 3.4.

There are also Cone Penetration Test (CPT) based methods formalized in the API guideline. These methods are:

- **Method 1, Simplified ICP-05:** research work performed at Imperial College on axial pile design criteria for open and closed-ended piles in clay and sand
- **Method 2, Offshore UWA-05:** research work at the University of Western Australia on the development of axial pile design criteria for open and closed-ended piles driven into silica sands
- **Method 3, Fugro-05:** a modification of Method 1 and was developed as part of a research project for API

- **Method 4, NGI-05:** developed by Norwegian Geotechnical Institute

For these methods, CPT cone-tip resistance, q_c, is required to be employed in the equations.

2.5 Q-z curves

API guideline suggests a table for z/D versus Q/Q_p tables for both clays and sands. The table for clay and sand layers is given in Table 2.6. Q_p is the end bearing capacity, and it is the product of the maximum unit end bearing and tip cross-sectional area of the pile. The maximum unit end bearing is calculated as is given in Equation 2.22. There is a limit value for this maximum unit end bearing, as can be understood from the equation.

Table 2.6: Definition of Q-z curves [101]

z/D	Q/Q_p
0	0
0.002	0.25
0.013	0.50
0.042	0.75
0.073	0.90
0.100	1.00
∞	1.00

$$f(z) = N_q\,\sigma'_0(z) < \ maximum\ unit\ end\ bearing \tag{2.22}$$

where $\sigma'_0(z)$ is effective vertical stress at depth z. Furthermore, limit values and end bearing factor, N_q, can be found in Table 2.7.

In the same way with the CPT-based t-z curves, there are CPT-based Q-z curves by the same four methods in the API guideline. For these methods, average CPT cone-tip

Table 2.7: Design parameters for Q-z curves [101]

Relative Density	End Bearing Factor (-)	Limiting Unit End Bearing (MPa)
medium dense	12	3
medium dense to dense	20	5
dense to very dense	40	10
very dense	50	12

resistance, q_c, between 1.5 times diameter above the pile tip and 1.5 times diameter below the pile tip is required to use in the equations. While method 1 presents pile end bearing capacity for both plugged and unplugged piles, method 2, method 3, and method 4 only offer plugged pile end bearing capacity.

2.6 Variability in soil properties

For the p-y method analysis, spring properties should be calculated. However, API [101] and DNV-DL [40] guidelines only require friction angle, unit weight, and modulus of subgrade reaction for sandy soils and undrained shear strength and unit weight for clayey soils [94]. As the unit weight is also correlated to friction angle and undrained shear strength, only one parameter affects the analysis results. That is friction angle for sandy soils and undrained shear strength for clayey soils. Therefore, the representative and accurate selection of these single parameters is essential. For example, the effective friction angle should be selected from the Mohr envelope based on relevant triaxial test conditions performed at appropriate stress levels. But choosing one single parameter for a layer is not trivial and requires a statistical approach for better design.

According to Phoon and Kulhawy [86] inherent variability, measurement error, and transformation/correlation uncertainty are the primary sources of geotechnical uncertainty. Seabed soils involve inherent variability as well as uncertainty in material

properties, especially when there are multi-layered or mixed soils due to natural geologic processes. During or after collecting a sample from a site, equipment, procedure, or sampling method mistakes could be caused. A limited number of sampling also plays a role in these measurement errors. Even if the sample is collected with minimal error, the overall error increases due to the nature of empirical or correlation models while transforming or correlating the site data to engineering soil properties. Therefore, modifications to deterministic design approaches are suggested in the literature to account for uncertainties and to achieve target reliability [28]. Hence, the variability in soil properties in a probabilistic approach should be incorporated to reach a more reliable and cost-efficient monopile design.

Especially in offshore wind turbine applications, probabilistic analysis is necessary due to four reasons. First, soil conditions may vary considerably in offshore wind farm sites, such as the case in Sheringham Shoal Wind Farm in the UK [66]. Second, offshore site investigation programs are more expensive than the ones onshore, and site investigations should be conducted over large areas compared to offshore oil and gas platforms; thus, they need to be efficiently planned to provide optimization and economy. [66]. Therefore, conducting one Cone Penetration Test (CPT) for each turbine is not possible. Thus, the soil variability may not be captured accurately since a low number of geotechnical field tests are applied in offshore environments usually. For instance, 88 wind turbines exist in Sheringham Shoal Wind Farm in the UK, where 12 boreholes were drilled, including 5 during the preliminary investigation stage and 7 during the main investigation stage. The boreholes were approximately 4–5 km apart, and their depths ranged from 26 to 70 m. The number of boreholes is recommended to be at least 10% of the number of turbine locations, and a larger number might be required if the site condition is complex [66]. The information from boreholes was complemented by CPT's and geophysical investigations. However, site specific design is likely to bring cost savings to the project [28]. Third, the recent trends suggest new offshore wind farms be built further offshore, which increases the uncertainty in knowledge on soil conditions [91]. Finally, the fact that any revision or fixing a failure would be challenging in economic terms, uncertainties, and risks in soil conditions of offshore wind turbine foundations gain considerable importance [66].

The effect of variability in soil parameters has been studied by other researchers. Glisic et al. [48] studied the effect of site conditions and load parameters on an offshore monopile via random sampling. They evaluated Sobol' indices for sensitivity analysis. They assigned a coefficient of variation of 10% to friction angle and unit weight whereas 35% to undrained shear strength. They concluded that the variation of soil parameters has little effect on results, considering both minimum and maximum stresses. However, variation changed the structural system characteristics. Moreover, the variation of the load parameters was found to have the highest effect when accumulated fatigue damage was evaluated. Yet, they did not consider the correlation between soil parameters. Depina et al. [39] researched the effect of spatial variability of stiffness in cyclic performance of a monopile. They employed a stiffness degradation model through finite element analysis. Results showed that the variability affects both the displacement and the rotation of the pile. Andersen et al. [11] conducted Monte Carlo Analysis by taking undrained shear strength as a random variable. They employed 40% COV on that and considered 2.5 and 5.0 m correlation length with a lognormal distribution. They aimed to identify the variation of lower natural frequency. They concluded that although the variation of the first natural frequency has a lognormal distribution, the variation of natural frequency did not have a lognormal distribution. Charlton and Rouainia [31] also studied the cyclic performance of a laterally loaded monopile in clay. They used the finite element method coupled with Monte Carlo Simulation. The study showed that the overall monopile behavior and performance are governed by the spatial variability of the clay layer. In a similar manner, spatial variability of clay layer for monopiles under static and cyclic loading was studied by Le et al. [66]. They examined the spatial variability of undrained shear strength and small-strain stiffness on the structure and concluded that variability is important in design. Chan and Low [30], El and Fajoui [42], Haldar and Sivakumar [52], Haldar and Babu [51], Low et al. [71] and Vahdatirad et al. [109] also investigated the undrained static lateral capacity variation of piles in clay. Cai et al. [28] focused on CPT data quantification, and they evaluated this data in a probabilistic manner. They aimed to evaluate the probability of failure of a pile in sand with this changing parameter. They assigned 0%, 15%, 30%, and 45% COV to CPT cone tip resistance with a different horizontal scale of fluctuation values. On the other hand, the vertical scale of fluctuation was taken as 1 m constant as they worked on a single

soil layer. They concluded that the reliability of the vertically loaded pile depends on the ratio between pile diameter and horizontal scale of fluctuation and soil properties. Reale et al. [91] also studied the CPT data variability on offshore monopile. They generated data sets with soil profiles having COV 5%, 10%, 15%, 20%, and 30% with different scale of fluctuations in sand. They stated that this variability affects expected frequency. Last but not least, reliability-based optimization was conducted by Barakat et al. [17].

2.7 Probabilistic evaluation of soil properties

Fenton [43] stated that designs by assessing only mean values of the properties are insufficient. He declares that the uncertainty and variability in the whole system should be considered to address failure probabilities. Thus, a probabilistic model in which their properties are represented as realistic as possible is required. Random fields should be created for this purpose. Then, an analysis should be conducted for each field/simulation. Consequently, the overall picture of the system is evaluated.

As the study involves statistical analysis, this section aims to introduce some probabilistic analysis methods. Therefore, Monte Carlo Analysis and probabilistic analysis parameters used in this analysis are explained in this section. There are more advanced sampling methods such as Latin Hypercube Sampling [55], but these methods are beyond the scope of this study. Moreover, Denmark soil data from literature is also reviewed, for a case study introduced in the next chapter is an element of focus. Additionally, as the particular focus of this thesis is Belgium, a section presenting Belgium soil data is also added.

2.7.1 Monte Carlo analysis

By the law of large numbers [12], it is possible to evaluate an integral defining the expected value of a random variable by taking the mean of all independent samples. This law is the main idea behind Monte Carlo Simulation. The estimator is unbiased and dependent on neither the random variables nor the complexity of the problem [34]. Thus, this method is advantageous for geotechnical problems where uncertainty

and nonlinearity dimensions are generally high.

In Monte Carlo Simulations, material properties (e.g., friction angle, cohesion, and unit weight for geotechnical problems) are considered random variables with a particular statistical distribution having a mean value and a coefficient of variation. Accordingly, random samples are generated in line with the given parameters and the number of simulations predefined. Depending on the complexity and the nature of the problem, the required number of simulations changes. While deciding on this number, the convergence of the results should be examined. The point where the results are converged indicates the required minimum number of simulations.

2.7.2 Probabilistic analysis parameters

According to Phoon and Kulhawy [86] for a soil layer, variability can be defined by a mean value and a coefficient of variation as a stochastic random field. The distribution of material properties is also important. The aim with probabilistic parameters is to create soil samples representing the actual soil layering with material properties as realistic as possible. Therefore, the simulations generated should be checked to confirm the accurate representation of the soil [111]. Only the samples that are in line with the experimental data should be considered in the analysis [103].

2.7.2.1 Statistical distribution of material properties

In the scope of this study, three commonly used statistical distributions are considered, namely normal, lognormal, and uniform distributions. Site-specific data should be considered in determining the statistical distribution for soil properties; then, that data should be represented by reasonable data sets.

The selection of the best possible statistical distribution is unique for selected soil property and the site [81]. Thus, it should be decided with solid actual field and laboratory test data.

As one of these distribution functions, normal distribution allows continuous probability distribution for a random variable. It is also known as Gaussian or Gauss or

Laplace–Gauss distribution. This distribution method is usually used when the distribution of real-valued random variables is unknown [29]. It has been utilized for soil properties by many researchers [59, 72, 75, 104].

The upper and lower boundaries for normal distribution can be approximated by the three-sigma rule [49] in which nearly all values are taken into account within three standard deviations of the mean. Mathematically, it represents 99.73% of all data, which is almost 100%. This distribution is given in Figure 2.9 for better understanding.

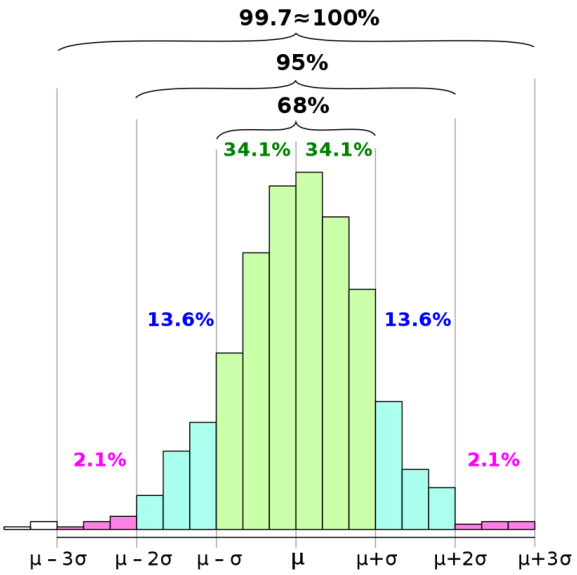

Figure 2.9: Boundary approximation for normal distribution [1]

This expression is given in Equation 2.23 for any arbitrary random X value.

$$P(\mu - 3\sigma \leq X \leq \mu + 3\sigma) \approx 99.73 \tag{2.23}$$

where,

μ : mean value

σ : standard deviation

As an example, a soil layer having 30° of friction angle as a mean value and 10%, 30%, and 50% of coefficient of variation with normal distribution is given in Figure

2.10.

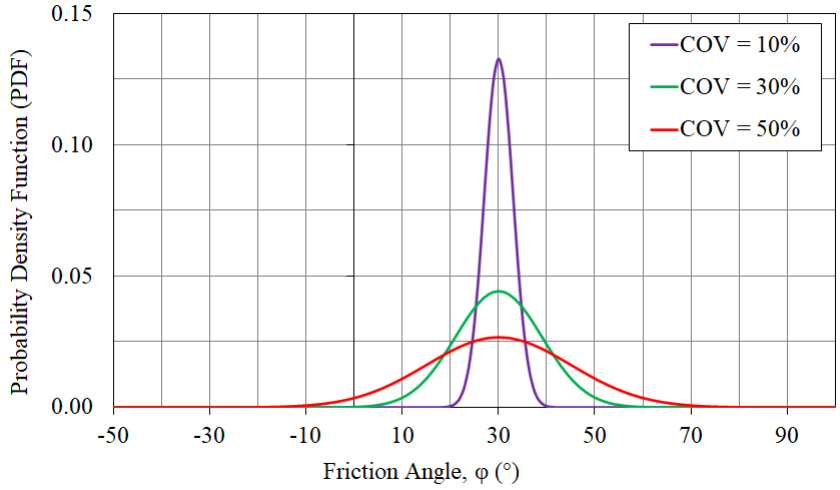

Figure 2.10: Normal material distribution

The second distribution function examined in the scope of this study is lognormal distribution. It does not allow any negative value, suiting the soil properties' physical meaning, thus avoiding any possible instabilities in analyses. However, due to the nature of this distribution, excessively high values are observed with a relatively high coefficient of variation values. It has been supported in geotechnical literature that this distribution represents the soil properties well [35, 50, 60, 107].

Similar to normal distribution, the upper and lower boundaries for lognormal distribution could be roughly approximated by the three-sigma rule [49]. However, it should be noted that as negative values are not allowed in lognormal distribution, its distribution is actually different from normal distribution. Same expression as given in Equation 2.23 could be used for any arbitrary random X value.

As an example, a soil layer having 30° of friction angle as a mean value and 10%, 30%, and 50% of coefficient of variation with lognormal distribution is given in Figure 2.11.

The last distribution function which is to be presented is uniform distribution. It enables the creation of data points defined with a lower and upper bound over which all data points have the same probability. The only required data to ultimately determine this distribution is the upper and lower boundary which can be readily available

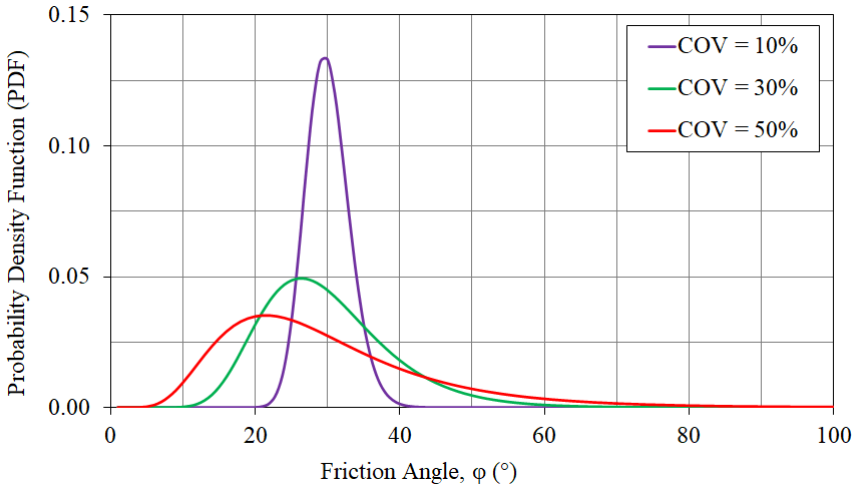

Figure 2.11: Lognormal material distribution

in geotechnical literature [113]. This distribution is given in Figure 2.12 for better understanding.

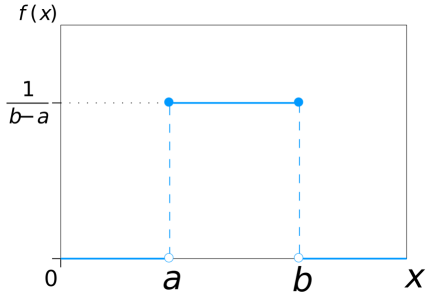

Figure 2.12: Boundary approximation for uniform distribution [2]

The upper and lower boundaries for uniform distribution can be calculated as is given in Equation 2.24 for any arbitrary random X value.

$$P(\mu - \sqrt{3}\sigma \leq X \leq \mu + \sqrt{3}\sigma) = 100\% \tag{2.24}$$

where,

μ : mean value

σ : standard deviation

As an example, a soil layer having 30° of friction angle as a mean value and 10%, 30%, and 50% of coefficient of variation with uniform distribution is given in Figure 2.13.

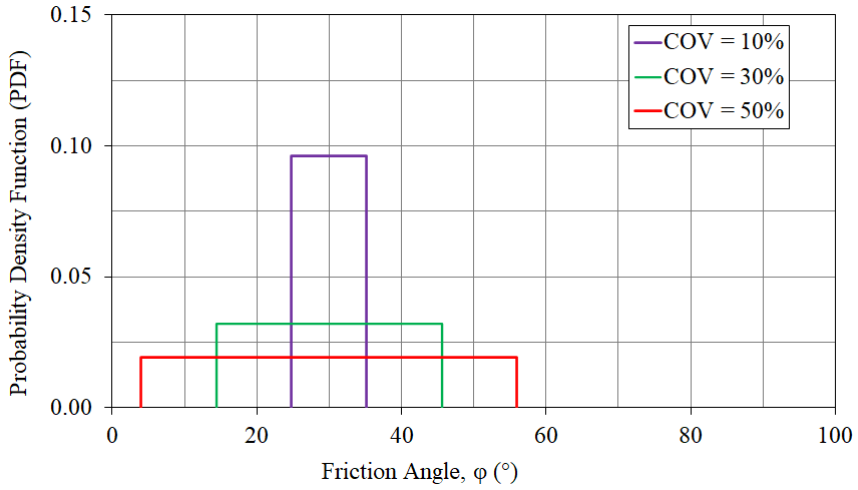

Figure 2.13: Uniform material distribution

2.7.2.2 Coefficient of variation

A coefficient of variation is a measure of dispersion/variability of a selected distribution from the mean value of the data set. It is the ratio of standard deviation to mean value in percentage. Whereas high values indicate a high dispersion from the mean, low coefficient of variation values indicate low variability of the data points. Besides, it is required to define stochastic random fields [86].

The coefficient of variation for friction angle for different sites; thus, soils have been reported by many researchers. Data from the literature are gathered in the scope of this study and presented in Table 2.8.

2.7.2.3 Correlation coefficient

A correlation coefficient is the measure of linear correlation between two data sets [19]. It indicates the strength and the direction of correlation. Whereas zero value means no correlation at all, as the correlation coefficients get closer to -1.0 or 1.0,

the correlation becomes stronger. A negative correlation coefficient means while one parameter has a higher value, the other correlated parameter has a lower value. Similarly, a positive correlation coefficient means while one parameter has a higher value, the other correlated parameter is expected to have a higher value from its span. Example sketches for a scattering of data sets with different coefficient of variation values are given in Figure 2.14.

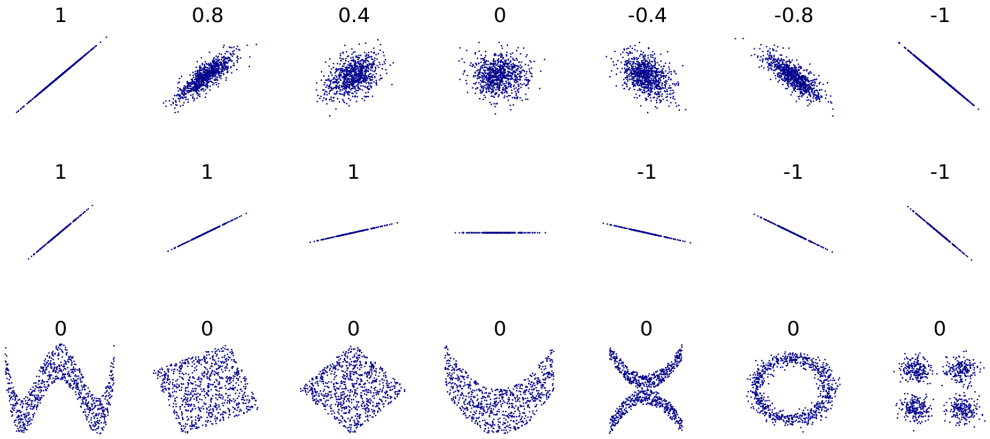

Figure 2.14: Scatter of data sets with different correlation coefficients [8]

The correlation coefficient between unit weight and friction angle for different sites; thus, soils have been reported by many researchers [114]. Data from the literature are gathered in the scope of this study and presented in Table 2.9. Note that c denotes the correlation coefficient.

Table 2.8: Coefficient of variation values from the literature for soil material properties

Reference	Friction Angle		Cohesion		Unit Weight		Location
	Mean (°)	CoV (%)	Mean (kPa)	CoV (%)	Mean (kN/m3)	CoV (%)	
Lumb (1970) [73]	-	0.8–5.9 (tan)	-	9–23	-	1–8	-
Matsuo & Kuroda (1974) [75]	-	5.8–46.6	-	20-40	-	-	-
Alonso (1976) [10]	-	13.8–22.9 (tan)	-	16.2–31.6	-	2.5–6.8	-
Lee et al. (1983) [67]	-	5-15	-	-	25-30	-	-
Nguyen & Chowdhury (1984) [80]	-	14–33	-	18-49	-	-	-
Harr (1984) [53], Kulhawy (1992)[65]	-	2-13	-	13-40	-	3-7	-
Becker (1997) [18]	-	5–25	-	12–85	-	4–16	-
Phoon et al. (1999) [86]	-	7-20	-	-	-	-	-
Phoon et al. (1999) [86]	-	10-15	-	-	-	-	-
Phoon et al. (1999) [86]	-	15-20	-	-	-	-	-
Phoon & Kulhawy (1999) [86]	-	5–15	-	-	-	3–20	-
Nadim (2007) [79]	-	2–5	-	-	15-21	0-10	-
Lee et al. (2014) [66]	46	6	-	-	19.5	-	Near shore
Lee et al. (2014) [66]	0.36	11	5	12	19.5	-	Near shore
Giampa & Bradshaw (2018) [47]	33	5.5	-	-	18	-	Near shore
Oguz et al. (2019) [83]	9-18	14-23	12	16.67	-	-	Near shore
Oguz et al. (2019) [83]	32-34	9-18	12	16.67	-	-	Near shore
Oguz & Huvaj (2020) [82]	27	4	12	16.67	18	-	Near shore
Cherubini (2000a) [33]	-	5–50	-	10–70	-	3–10	-
Cherubini (2000b) [32]	-	1–87.2	-	12–145	-	1–27.9	-
Forrest & Orr (2010) [45]	-	5–15	-	20–40	-	1–10	-
Hata et al. (2011) [54]	-	5.7–76	-	14.5–106.8	-	-	-

Table 2.9: Correlation coefficient values from the literature for friction angle and unit weight

Reference	Soil	Correlation		Test	No. of Samples	Drainage Condition	Location
		$\phi^{\smile}c$	tan$\phi^{\smile}c$				
Matsuo & Kuroda (1974) [75]	Soil 1: Clay, silty sand (Sr = 85-95%)	-	0.713	unconsolidated undrained triaxial test	-	undrained	near Watarase River, Japan
	Soil 2: Silt, sandy silt, clayey silt, silty sand (Sr = 85-95%)	-	0.656	unconsolidated undrained triaxial test	-	undrained	near Watarase River, Japan
	Soil 3: Silty sand (Sr = 16-22%)	0.927	0.926	direct shear test	60	undrained	mountain near Agigawa River, Japan
	Soil 3: Silty sand (Sr = 32-44%)	0.862	0.859	direct shear test	60	undrained	mountain near Agigawa River, Japan
	Soil 3: Silty sand (Sr = 49-66%)	-0.953	-0.943	direct shear test	60	undrained	mountain near Agigawa River, Japan
Chowdhury & Xu (1992) [36]	-	0.7	-	-	-	-	-
Low & Tang (1997) [70], Wu (2013) [114]	-	0.5	-	-	-	-	-
Babu & Srivastava (2007) [15]	Case 1	0.25	-	non-experimental	-	drained	-
	Case 2	0.5	-	non-experimental	-	drained	-
	Case 3	0.75	-	non-experimental	-	drained	-

2.7.2.4 Spatial correlation length

Spatial correlation length (SCL) is a scale of fluctuation and a key parameter for random field theory [84, 82]. An SCL can be defined as a distance in which soil material properties are spatially correlated. A high number of SCL means that the soil parameters are not much related. Likewise, a low number of SCL implies that the soil properties are highly similar. This correlation could be in the vertical direction (i.e. with depth), or in horizontal direction. Besides, these lengths may or may not be equal. If vertical and horizontal SCL are the same, the correlation is isotropic. If not, then it is anisotropic. However, Phoon and Kulhawy [86] stated that the horizontal SCL is much greater than the vertical and generally around 40-60 m for natural soils. Baecher and Christian [16] recommended the ratio of horizontal SCL to vertical SCL to be greater than 10. Yet, as the consideration of spatial correlation length requires more advanced analysis, SCL is omitted in the current study.

2.7.3 Denmark soil data

Denmark has 7% of the 220 GW total wind capacity of Europe [64]. According to the study conducted by Breuning-Madsen et al. [25], coarse sand is found to be a common soil type in Denmark, especially in the west, whereas fine sandy clay to clay soils are encountered in the center and south-east. Additionally, fine sands and fine clayey sands exist in the northern parts. They created the first soil map of Denmark based on analytical data and local expert knowledge. This mapping classifying Danish fields into eight major soil types can be seen in Figure 2.15.

These data are created by approximately 36,000 sample sites chosen throughout Denmark's agricultural area (around one sample per km^2). Moreover, soil samples were gathered from the topsoil (0-20 cm) and subsurface (35-55 cm) at selected sites, thus indicates surficial soils.

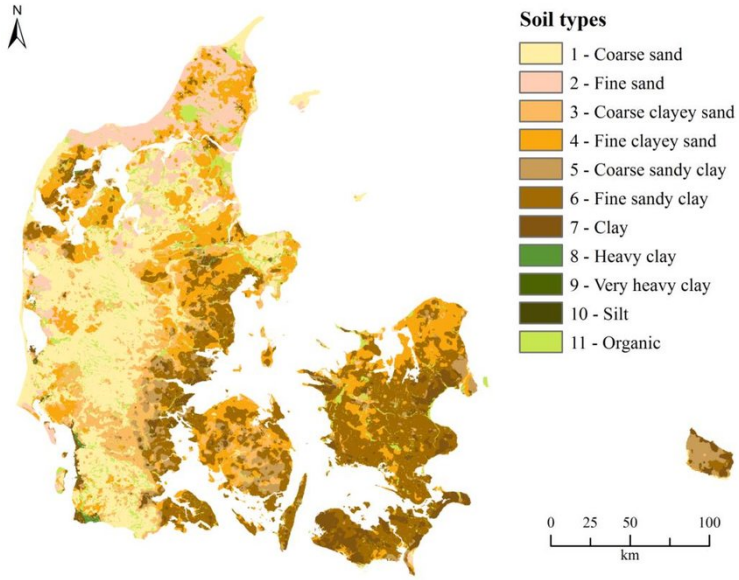

Figure 2.15: Soil types of Denmark according to the Danish Soil Classification [25]

2.7.4 Belgium soil data

Belgium has 9% of the 220 GW total wind capacity of Europe [64]. However, Belgium soil data published in the literature is very limited. Van Alboom and Baertsoen [110] examined triaxial test results for tertiary sands and tertiary boom clay. It is stated that sand layers have a friction angle of 33.6° (Kattendijk) and 36° (Antwerpen/Edegem) with no cohesion. Clay layer has 23° friction angle and 24 kPa cohesion. Another study by Rogiers et al. [99] published soil categorization for 480,000 soil samples located in northern Belgium according to Robertson soil classification charts [98, 96]. Results indicate that most soils consist of sands, clean sand to silty sand, and gravelly sand to dense sand. The classification charts of these points are given in Figure 2.16.

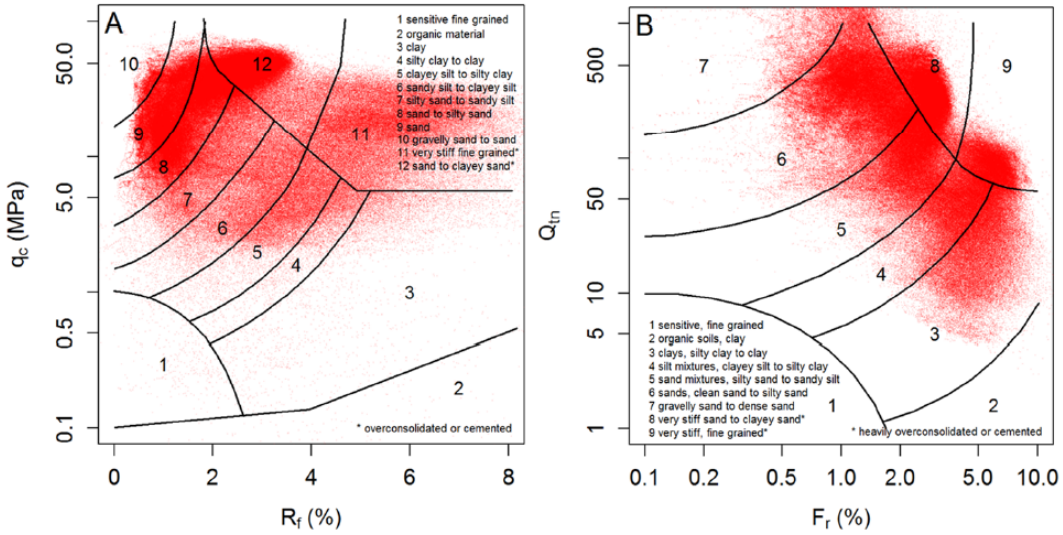

Figure 2.16: Soil classification results for northern Belgium with 480,000 soil samples [99]

CHAPTER 3

DETERMINISTIC ANALYSIS FOR MONOPILES

3.1 Introduction

In this chapter, the analysis methodology followed in this study is explained in a detailed manner. A single analysis by the p-y method is to be conducted to check the structural stability and serviceability of a monopile according to American Petroleum Institute (API) [101] and Det Norske Veritas - Germanischer Lloyd (DNV-GL) [40] guidelines.

This chapter aims to describe the methodology along with all the assumptions for a static monopile loading and prove its validity by a case study. Implementation of the design checks and interpreting these results are also the scopes of this chapter. In this regard, a methodology section, a verification of the analysis section, a design checks section, and an interpretation of the results section are presented in this chapter.

3.2 Methodology

The methodology used in this thesis can be summarized in 4 steps which are:

1. Designing monopile (i.e., diameter, length, thickness, and steel grade) using the mean value of friction angle and unit weight per soil layer,
2. Creating soil layers (having mean value, coefficient of variation (COV), and correlation) with random material properties by Monte Carlo simulation,
3. Analyzing each case from step 2,

4. Calculating probability of unsatisfactory performance (PUP).

For the analysis mentioned in step 3, the p-y method suggested by (API) [101] and summarized in Section 2.3.3 is followed with a minor modification for the initial modulus of subgrade reaction calculation. This modification is explained in Section 3.2.2. In the light of the guideline, a finite element based framework is developed in order to solve deflections for small diameter piles by applying lateral (p-y) and axial (t-z and Q-z) curves under static loading.

The calculations are executed in Python, and OpenSees is employed as a non-linear solver [77, 115]. Furthermore, material sections available in the OpenSees library for Python are utilized.

3.2.1 Pile properties

A hollow steel section is defined with its embedded length, L_e, free length, L_f, diameter, D, thickness, t, area, A, moment of inertia, I, Young's modulus, E, plastic modulus, Z, and radius of gyration, K.

The pile is considered as a 1D beam element and meshed with a mesh size of $s/2$ at the tips and s elsewhere. In other words, only the very top and bottom meshes have half of the predefined vertical mesh size. An example mesh of a pile with a mesh size s is given in Figure 3.1.

The pile is modeled as an Euler-Bernouilli beam that ignores shear deformation and rotary inertia. Hence, it could be considered as a special case of the Timoshenko beam model. As the model is simple and choosing between Timoshenko and Euler Bernoulli beam models does not affect the results much, the Euler Bernoulli beam model is employed.

The code is only applicable to the condition where the diameter over thickness ratio is smaller than 300. For the conditions above this limit, API [101] suggests using API 2U.

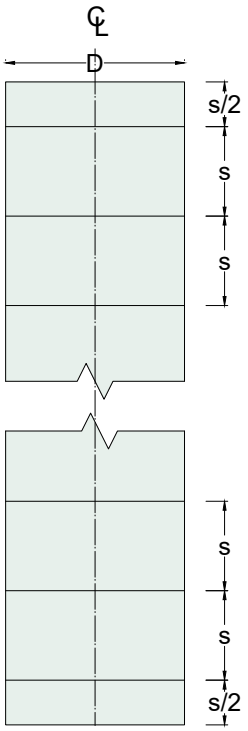

Figure 3.1: Pile mesh

3.2.2 Spring properties

Winkler springs are assessed to represent the soil-structure interaction as a boundary condition. In this regard, load versus deformation curves are to be formed by considering the material strength properties, namely friction angle and cohesion, of a soil layer. Note that, as sand and sandy soils are considered in this study, the only material strength property employed is friction angle. After forming these curves, they are assessed in line with the pile meshes given in Figure 3.1. An example mesh of a pile with a mesh size s including the springs is shown in Figure 3.2. Here, D denotes the diameter.

For these non-linear springs, lateral displacement - lateral force (p-y curves), axial deflection - axial force (t-z curve), and tip deflection - axial force (Q-z curve) behaviors are implemented for analyses in the light of the API guideline [101].

For axial deflection - axial force (t-z curves) non-linear springs, the pile is assumed to be driven unplugged. It is the practice suggested by the API guideline to use the

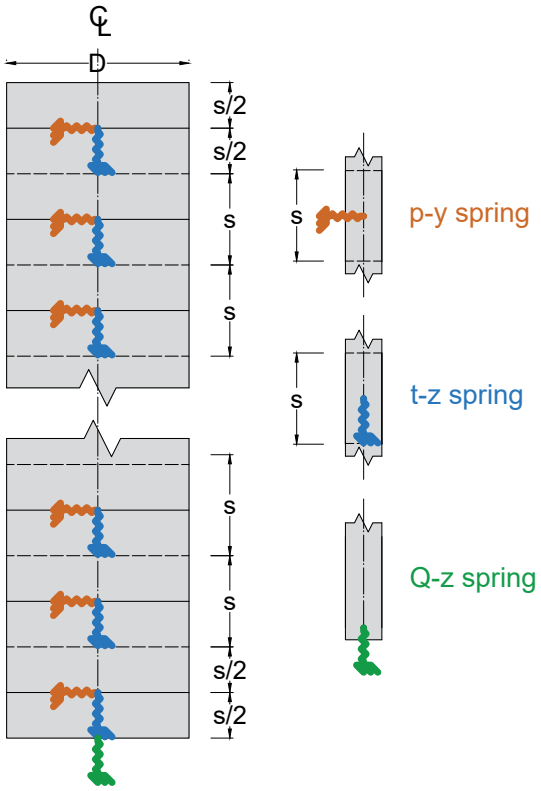

Figure 3.2: Spring assignment along the monopile

dimensionless shaft friction factors given in Table 2.5 in the absence of specific data. On the other hand, if the pile is plugged, the dimensionless shaft friction factors can be assumed 25% higher than the values given in the table. However, as the specific data for the monopile is not available, the unplugged assumption is followed, and the dimensionless shaft friction factors given in Table 2.5 are directly used for analyses.

All the initial modulus of subgrade reaction, k, values for piles below the water table given in the previous sections are plotted together in Figure 3.3 for comparison purposes. It is clear that there is no specific agreement on the subject, and the k values may change depending on the guideline selected for the design. Although LPile fine sand and DNV-GL relative density based methods define a boundary for the k value after some definite friction angle, API and DNV-GL friction angle based methods avoid giving a recommendation for layers having high friction angles.

Note that the DNV-GL relative density based method is transformed to friction angle domain by the graph given by previous API guideline [57] (Figure 3.4).

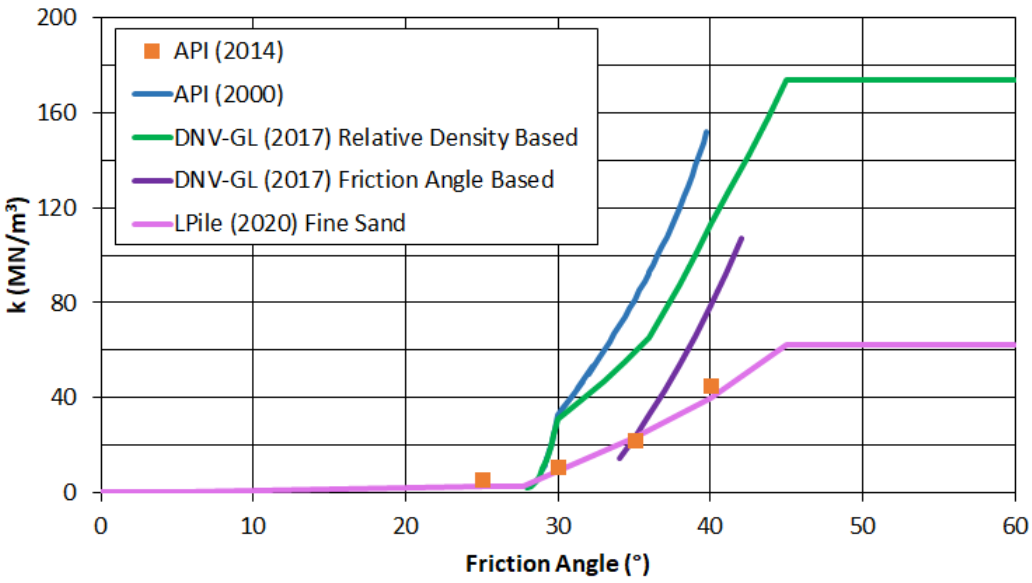

Figure 3.3: Comparison for initial modulus of subgrade reactions based on different guidelines

For the initial modulus of subgrade reaction, k, suggested values by API guideline as is given in Table 2.2 are used. However, instead of linear interpolation, a third-degree polynomial equation is fit to the points for better estimation. The related formula is given in Equation 3.1, with a coefficient of determination, $R^2 = 1$.

$$k = 0.0088\,\phi^3 - 0.684\,\phi^2 + 18.72\,\phi - 172.6 \tag{3.1}$$

On the other hand, layers having a friction angle value greater than 40° and less than 25° have to be handled separately. For the layers having less than 25° of friction angle, the method followed by LPILE software is followed [95]. In such regard, the initial modulus of subgrade reaction at 0° of friction angle is assumed to be 0 MN/m^3 and linearly varies up to 25°. The related formula considered is given in Equation 3.2, with a coefficient of determination, $R^2 = 1$.

$$k = 0.216\,\phi \tag{3.2}$$

Two different approaches are considered for the layers having greater than 40° of

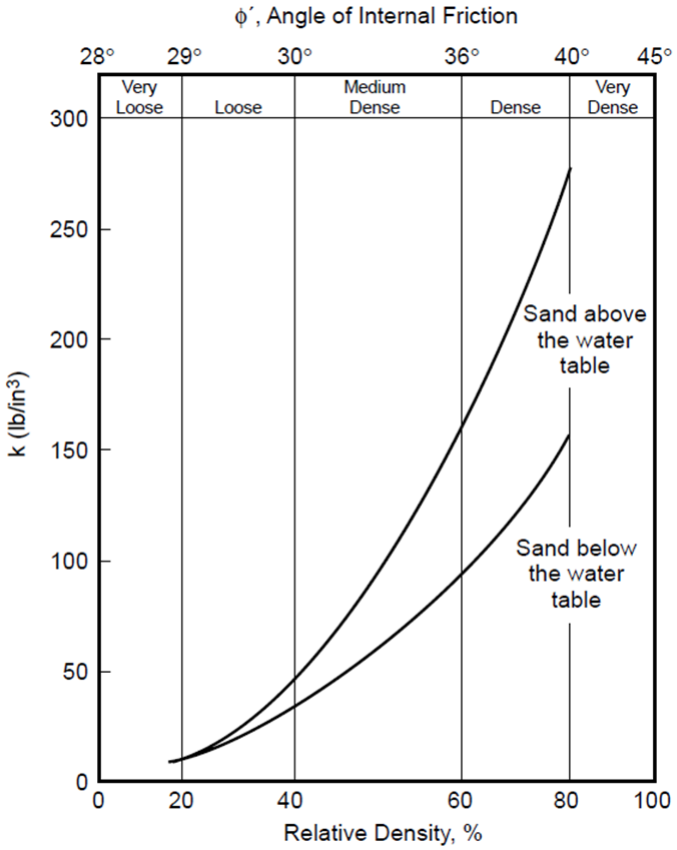

Figure 3.4: Relative density, angle of internal friction, and k chart given by previous API guideline [101]

friction angle. The first approach is similar to the method followed by LPILE software [95]. Therefore, the initial modulus of subgrade reaction is forced to be equal to the value related to the friction angle of 40° and constant for greater values. The related formula is given in Equation 3.3.

$$k = 45 \tag{3.3}$$

The other approach is considering the slope of the polynomial equation at the upper limit, 40°, and extending this slope beyond the limit for the values greater than 40° of friction angle. The related formula is given in Equation 3.4.

$$k = 6.24\,\phi - 204.6 \tag{3.4}$$

All of the portions explained are sketched and given in Figure 3.5. In the figure, A denotes the linear part (Equation 3.2), B denotes the portion with the third-degree polynomial (Equation 3.1), C denotes the limited k approach beyond 40° of friction angle (Equation 3.3), and D denotes the non-limited k approach (Equation 3.4) in terms of initial modulus of subgrade reaction.

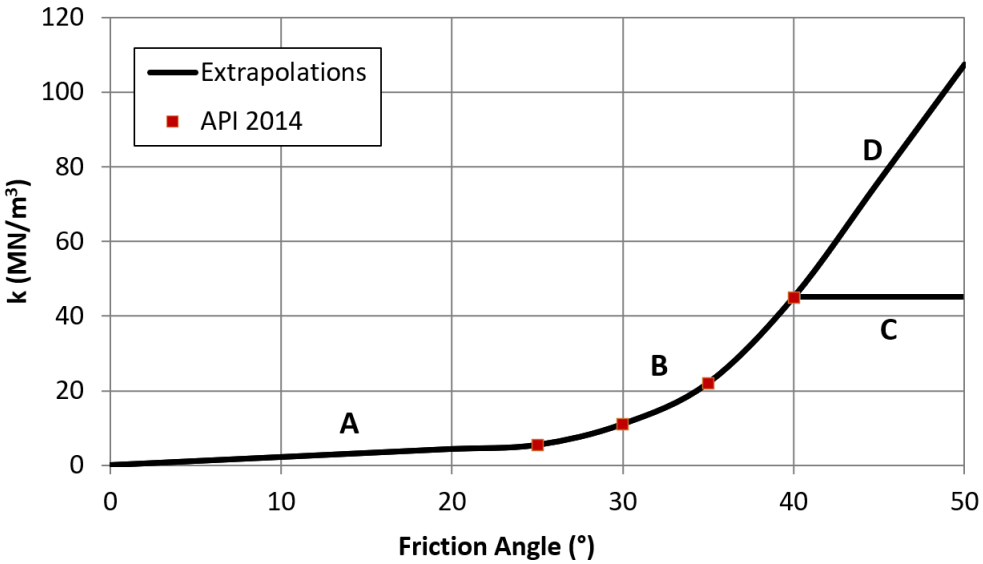

Figure 3.5: Friction angle versus initial modulus of subgrade reaction

The soil-structure interaction is accounted for using a p-y approach, using springs along the monopile. As a macro element, zero-length is employed as springs to reflect the soil behavior along the pile (in other words, soil-structure interaction). With this element, the force deformation relationship of the springs can be constructed. The related force deformation relationship is stored in elastic multi-linear objects. Note that, elastic multi-linear objects are used to build a multi-linear elastic uniaxial material object by defining the nonlinear stress-strain relationship.

3.2.3 Load definition

Applied forces and moment are simplified as point loads and a moment. The point of application of this loading is at the mudline level and has three components, namely lateral force, F_h, vertical force, F_v, and moment, M. These loads and the moment are applied concurrently. The point of loading can be seen in Figure 3.6. Dynamic and

cyclic loads are not considered for analyses.

In OpenSees, a load-controlled analysis is conducted. Analyses are performed in ten load steps with an increment of 0.1 times of the load in each step.

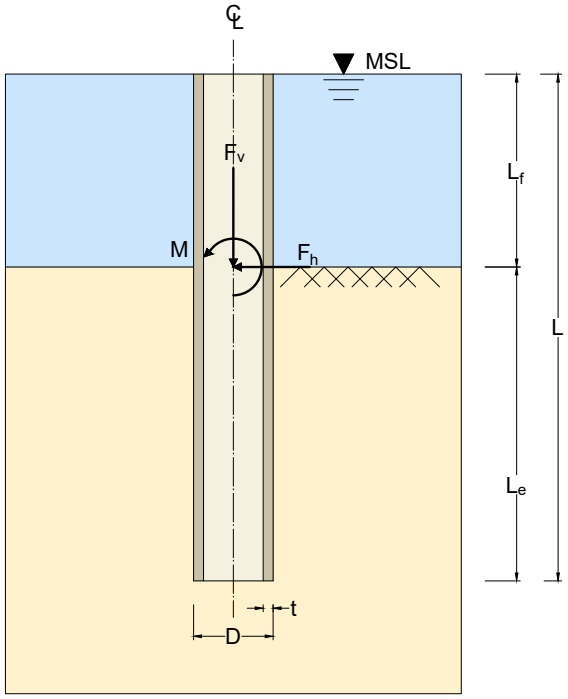

Figure 3.6: Point of loading

3.2.4 OpenSees analysis

A framework to conduct finite element analysis for monopiles is set. Only the static condition is considered. For solving nonlinear algebraic equations [77, 115], there are several different algorithms such as Linear, Newton, Modified Newton, Raphson Newton, and Krylov Newton method. Krylov Newton method is used in this study as this method accelerates the convergence of the Modified Newton with a Krylov accelerator.

The tower and the transition piece of the wind turbine are not modeled. For the analysis, related forces are transformed to the monopile structure. Hence, only the monopile is considered in the study. Moreover, a single thickness is considered throughout the pile rather than a varying thickness along the pile length for simplicity.

The number of dimensions and the degrees of freedom considered for the analysis are 2 and 3, respectively.

For analyses, tolerance criteria used to check for convergence is set as 10^{-7}, and the maximum iteration number is designated as 100,000. These numbers are found adequate, and there occurred no errors with the convergence. The constraints can be handled by either Plain constraints, Lagrange Multipliers, Penalty Method, or Transformation method. For the study, the transformation method is selected as it reduces the size of the system for multi-point constraints. It condenses out the constrained degree of freedoms and transforms the structural stiffness matrix. For mapping between the degrees of freedom at the nodes and the equation numbers, the RCM numberer using the Reverse Cuthill-McKee algorithm is selected among other numberers, namely Plain, AMD, Parallel Plain, and Parallel RCM. The reason for selecting this numberer is that the node numbering is optimized to decrease bandwidth using a numbering graph. This method also provides a warning output when the structure is disconnected.

Moreover, there are several methods as a system command, including Band General, BandSPD, and Profile SPD. For the analyses, full general system is employed. This selection is used to construct a linear system of equation object. As can be grasped by the name itself, there are no space-saving techniques to reduce the memory usage implied by this system.

3.3 Verification of the analysis

In this section, the case study of a monopile foundation in the North Sea, west of Esbjerg in Denmark, is studied in detail. This monopile structure is a part of the Horns Rev I offshore wind farm commissioned in December of 2002 [14, 68]. It is located 14 km away from the east shore, Blåvands Huk, and 28 km away from the south shore, Fanø approximately. The location of the wind farm is given in Figure 3.7. The wind farm has a total of 80 turbines, each having 60 m tower height and 80 m rotor diameter. Each turbine has a capacity of 2 MW; thereby, the wind farm has a total capacity of 160 MW. The wind turbine utilized for verification in this study is

also known as wind turbine 14 of the Horns Rev I offshore wind farm.

Figure 3.7: Location of the Horns Rev I offshore wind farm

The model idealization is an Euler-Bernoulli beam connected to p-y-springs below the mudline, as is explained in the previous section. A simplified version of the monopile structure is given in Figure 3.8.

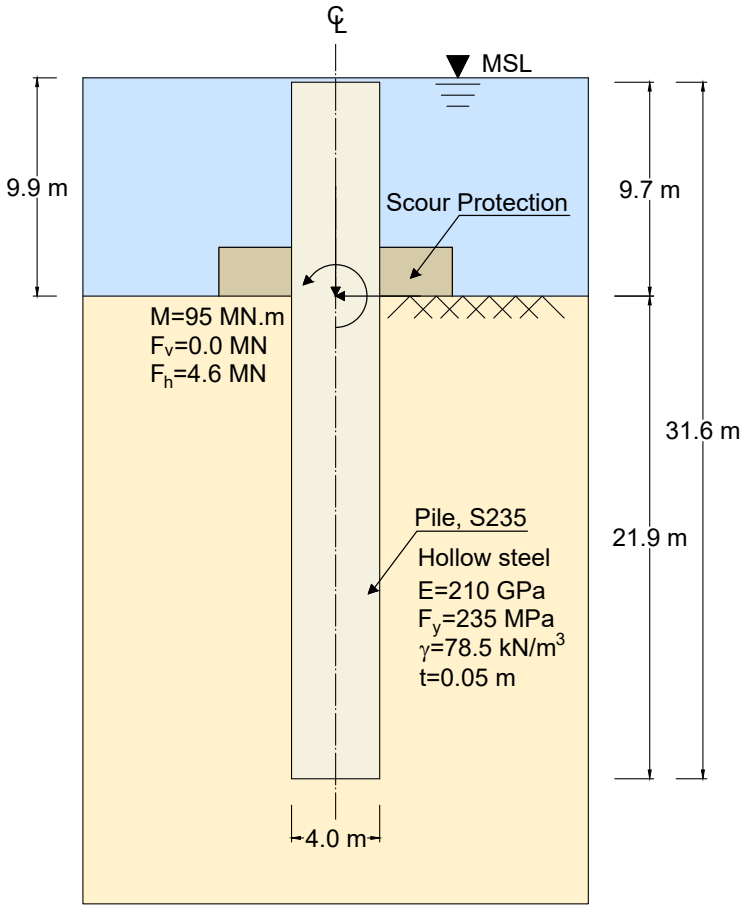

Figure 3.8: Model idealization

The results calculated by finite element analysis via p-y curves are compared to the case study results. However, the case study does not involve a shear force diagram along the pile. Therefore, an additional analysis via LPILE software is conducted for the sake of completeness. Assumptions and calculations are made in accordance with the reference paper [14].

3.3.1 Model parameters

This section includes monopile structural properties, soil properties, and the loading condition.

The wind turbine given in the case study is Vestas V80-2.0 MW model with 3 bladed rotor and 80 m rotor diameter. An example of this turbine is shown in Figure 3.9 for illustration. The monopile has a total length of 31.6 m, a diameter of 4 m, and varying wall thickness between 30-52 mm, denoting that the bending stiffness of the structure also varies along the pile. However, for the sake of simplicity, the wall thickness is considered as 50 mm throughout the verification. Steel is considered as linear elastic material with Young's Modulus of 210 GPa and Poisson's ratio of 0.3, in accordance with the case study. The steel section is considered as S235 with a unit weight of 78.5 kN/m^3.

Figure 3.9: Vestas V80-2.0 MW turbine [9]

The local soil profile consists of six layers, composed of sand, sand/silty sand, sand/silt/organic layers with varying thicknesses of 2.0 m to 5.4 m. There is a weak sand/silt/organic layer that is 4.2 m thick, which has relatively low material strength properties [14]. Figure 3.10 shows the soil layering with material properties.

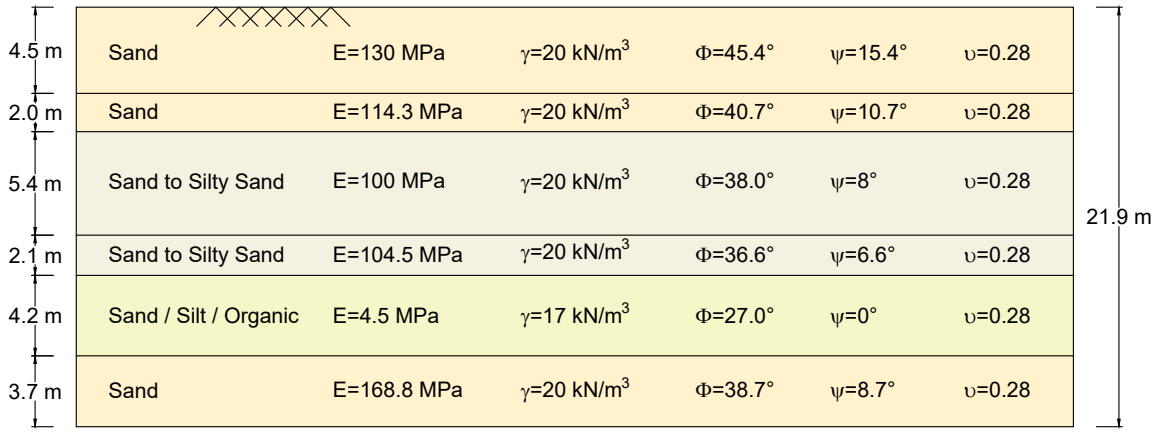

Figure 3.10: Soil layering and material properties

For the soil layering given, lateral displacement - lateral force (p-y) curves, axial deflection - axial force (t-z) curves, and the tip deflection - axial force (Q-z) curve are given in Figure 3.11, Figure 3.12, and Figure 3.13 respectively. These curves are assigned with a spring spacing of 0.1 m. In this manner, a total of 219 p-y curves, 219 T-z curves, and 1 Q-z curve at the pile tip are assembled. Each spring property is calculated according to the related soil layer in the light of the API guideline [101]. However, in API, the initial modulus of subgrade reaction for the sand layers having a friction angle lower than 25° and greater than 40° are not given. Therefore, handling soil layers with a friction angle outside the range 25-40° could differ depending on the approach. In order to be consistent with the case study and LPILE, the initial modulus of subgrade reaction for layers having friction angle lower than 25° are evaluated as zero. On the other hand, it is taken as 45 MN/m^3 as is given in Equation 3.3 for layers having friction angle greater than 40°.

At the mud line level, the applied horizontal force and moment are 4.6 MN, 95 $MN \cdot m$, respectively. The weight of the structure is the summation of 365 kN rotor load, 600 kN nacelle load [9], and 1.4 MN tower and pile load. Nevertheless, as the effect of the vertical load is negligible, the case study disregarded this load and

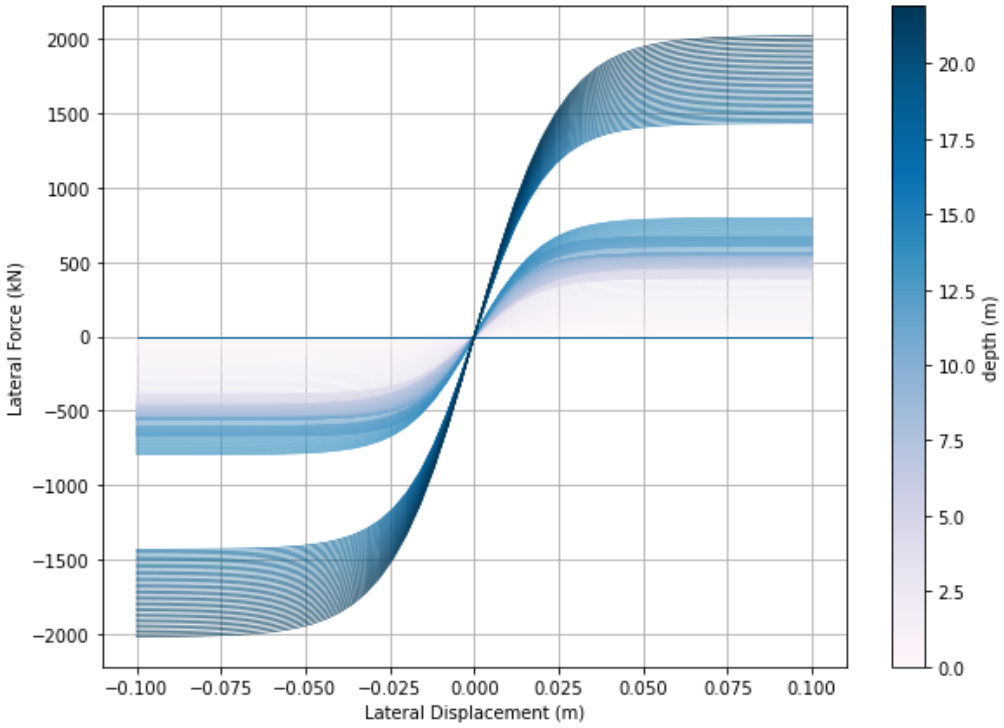

Figure 3.11: p-y curves

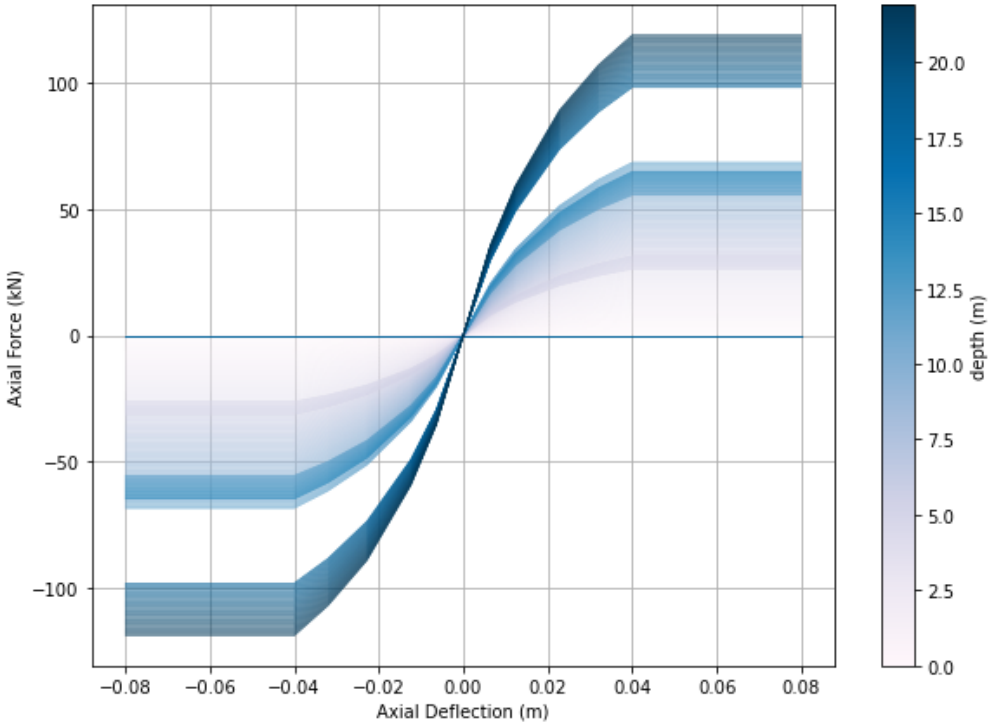

Figure 3.12: T-z curve

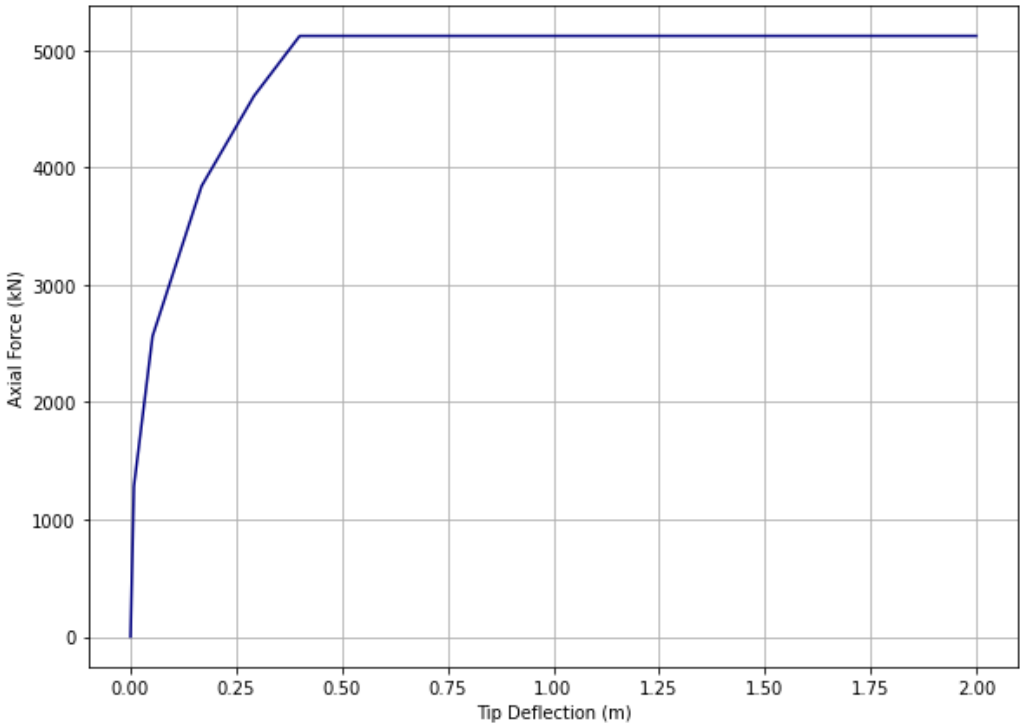

Figure 3.13: Q-z curve

evaluated vertical load as zero. Compatible with the study, the vertical load is taken as zero in this research.

3.3.2 Comparison of results

Comparison of the results agrees with the case study, validating the employed approach in this study. For comparison purposes, analyses results calculated via Python and LPILE are evaluated.

While all of the models employ p-y curves according to API, there are slight differences in each of them. The current study and the paper in which the case study is given use the previous version of API [57], while LPILE utilizes the latest version of API [101]. Therefore, some p-y curve parameters (such as initial modulus of subgrade reaction values) are different to a small extent. In all of the figures under this section, depth of zero meters indicates the mudline level.

3.3.2.1 Displacement

The comparison for displacement results is presented in Figure 3.14. The undeformed shape is also given in the figure for illustration purposes. The divergence between the case study results and the analysis results at the mud line level is found to be 2.9%. Monopile shows zero displacements around 10 m depth below the mudline level. The shallower and deeper depths show deformations in opposite directions. As expected, the maximum displacement is observed at the top and found to be 2.8 cm. On the other hand, the displacement at the bottom of the pile is -0.2 cm.

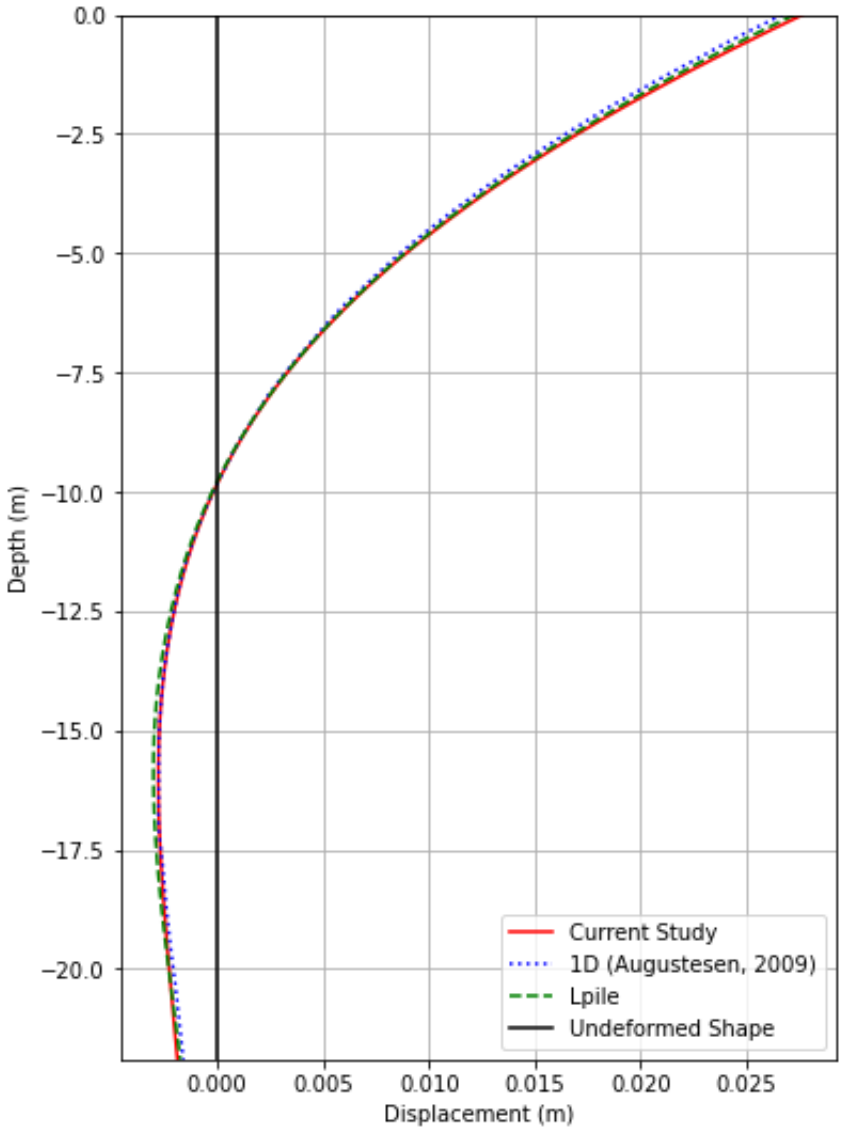

Figure 3.14: Displacement comparison

3.3.2.2 Shear force

The comparison for shear force results is given in Figure 3.15. There is no shear force diagram shown in the case study. Therefore, the comparison is only made with LPILE. The divergence between the LPILE results and the analysis results at the mud line level is almost zero. From the depth of -14 m to -18.2 m, there is a weak sand/silt/organic layer. As the initial modulus of subgrade reaction for this weak layer is evaluated as 0 MN/m^3, the assigned p-y springs are zero-valued. Therefore, there is no shear force change throughout these depths. The maximum shear force is observed as -8.5 MN at -9.75 m depth. While the shear force at pile top is calculated as 4.6 MN (the same value with initially applied horizontal force, F_h), the shear force at the bottom of the pile is 0 MN.

3.3.2.3 Moment

The comparison for moment results is given in Figure 3.16. The divergence between the case study results and the analysis results at the mud line level is 0.5%. The maximum moment is observed as 105 $MN \cdot m$ at -3.35 m depth. While the moment at pile top is calculated as 95 $MN \cdot m$ (which is the same value as initially applied moment, M), the moment at the bottom of the pile is 0 MN. The case study results slightly differ from the other results between approximately -10 m and -20 m. This behavior can be explained as the handling of the initial modulus of subgrade reaction for the weak sand/silt/organic layer, which is located from -14 m to -18.2 m.

3.4 Design checks

The probability of unsatisfactory performance is considered in terms of the serviceability and ultimate limit states in accordance with API [101] and DNV-GL[40] guidelines. While the ultimate limit states are considered by the API guideline, the serviceability design state is checked according to DNV-GL. The design checks are given in Table 3.1. These checks can be comprehended as performance measures for better understanding.

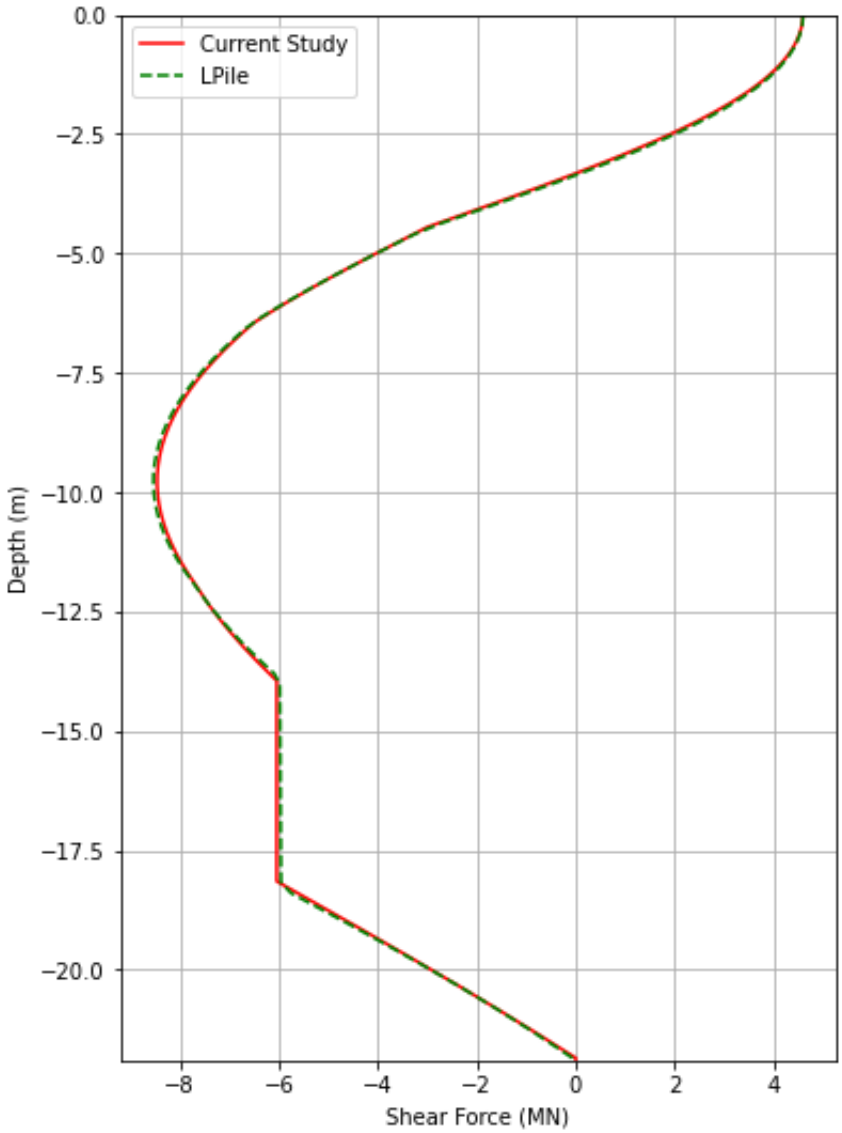

Figure 3.15: Shear comparison

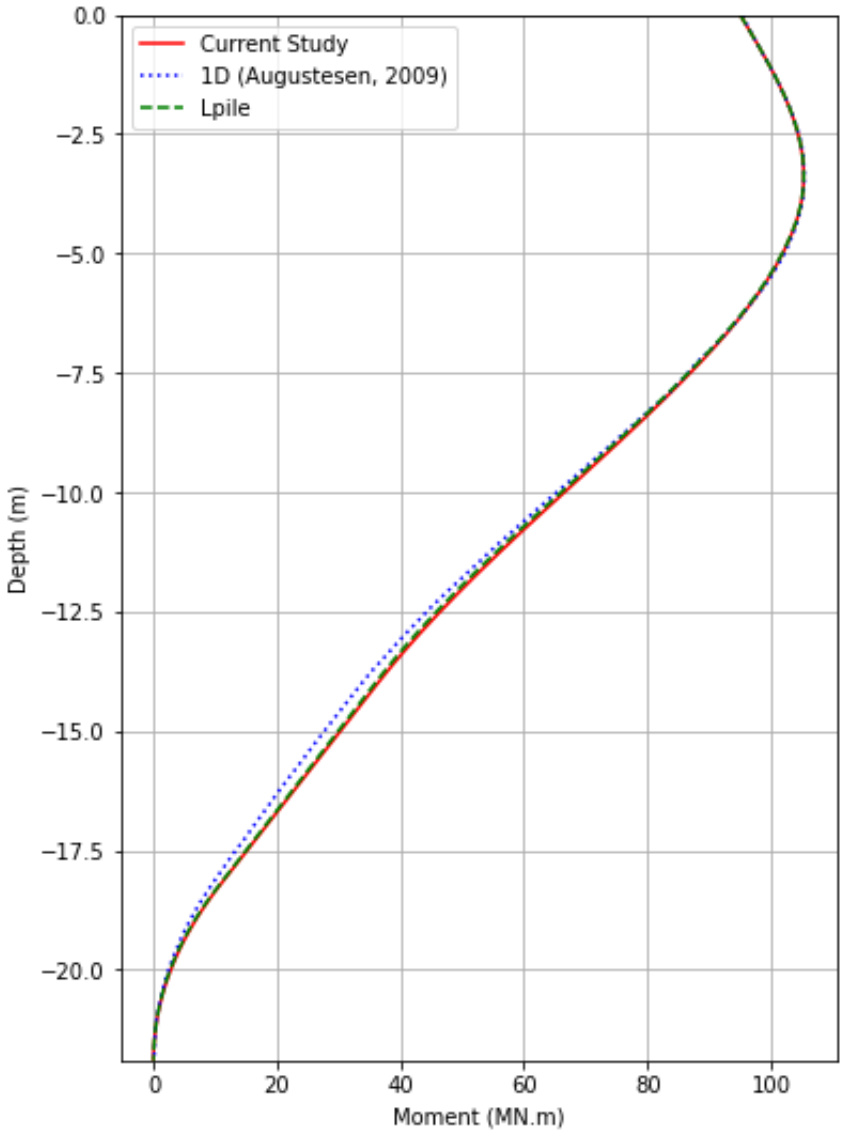

Figure 3.16: Moment comparison

Table 3.1: Ultimate and serviceability design checks

Guideline	Checks	Condition
API	Shear	$f_s = \frac{V}{0.5A} < F_s = 0.4F_y$
API	Combined	$\frac{f_a}{0.6F_{xc}} + \frac{\sqrt{f_{bx}^2+f_{by}^2}}{F_b} \leq 1.0$
API	Overload	$\frac{P_v/A}{F_{xc}} + \frac{2}{\pi}(\arcsin\frac{M/Z}{F_{xc}}) \leq 1.0$
API	Soil Bearing	$\frac{F_v}{A} \leq Q_c = Q_p + Q_{fc}$
DNV-GL	Service	$\delta < \frac{2L}{200}$

where,

f_a : Absolute value of acting axial stress

f_{bx} : Absolute value of acting resultant bending stress in x direction

f_{by} : Absolute value of acting resultant bending stress in y direction

f_s : Maximum beam shear stress

A : Cross sectional area

F_b : Allowable bending stress

F_s : Allowable beam shear stress

F_{xc} : Inelastic local buckling stress

F_y : Yield strength

L : Total length of the monopile

M : Bending moment

P_v : Axial loading

Q_c : Ultimate axial capacity of piles in compression

Q_{fc} : Shaft friction capacity in compression

Q_p : End bearing capacity

V : Transverse shear force

Z : Plastic modulus

δ : Lateral displacement

3.5 Interpretation of the results

After the calculation has been performed, analysis results are examined in terms of statics and serviceability performance. In this regard, resulting forces, stresses, and moments acting on the structure with the deflections are examined. The evaluation of these results is considered in the light of design guidelines [101, 40]. In such a manner, limit values given in Table 3.1 (such as shear, combined, overload, soil bearing, and service checks) are checked. If a monopile with given geometry and parameters fails to satisfy any of these checks, it is evaluated as unsatisfactory. This means that either further investigation or redesign is required for the structure under the given loading condition.

3.6 Conclusions

This chapter presented and verified the analysis methodology, explained design checks and their interpretation for monopiles. The maximum divergence between the case study results and the analysis results at the mud line level is found to be 2.9% for displacement, which is quite low. This points out that the methodology employed in this chapter is verified. Note that this methodology is only valid for sandy soils in static loading conditions.

CHAPTER 4

PROBABILISTIC ANALYSIS FOR MONOPILES

4.1 Introduction

In this chapter, the probabilistic analysis methodology is explained in detail. Monte Carlo Simulation is employed for statistical analyses. The required soil data for the study is gathered from the literature and real site data. This chapter aims to show and discuss the effects of coefficient of variation (COV) and distribution function selection on the structure's probability of unsatisfactory performance. In order to do so, first, the case study introduced in Chapter 3 is assessed with different COV and statistical distribution of soil parameters. These parameters are selected considering the soil data available in the literature for that region. Then, a monopile is designed in the light of American Petroleum Institute (API) [101] and Det Norske Veritas - Germanischer Lloyd (DNV-GL) [40] guidelines in Belgium offshore. This monopile is designed according to the soil data provided by Databank Ondergrond Vlaanderen [3]. Similarly, the effects of COV and distribution function selection on the structure's probability of unsatisfactory performance (PUP) is examined for this monopile. This time, both the soil data available in the literature for the Belgium coast and actual soil data for that region are considered in selecting probabilistic parameters. Finally, the findings are presented and discussed.

4.2 Methodology

Seabed soil parameters are assumed to have variability handled by statistical distributions in probabilistic analysis. As explained earlier, for a p-y analysis, the required

parameters for a sandy soil profile are friction angle, unit weight, and modulus of subgrade reaction [94]. In this study, different soil layers having correlated friction angle, unit weight, and modulus of subgrade reaction are created. Subsequently, the monopile is evaluated in terms of its performance in each simulation. Consequently, the overall performance of the same monopile is calculated by considering all simulations.

4.2.1 Analysis parameters

As there is a correlation between friction angle, unit weight, and modulus of subgrade reaction, the only required parameter is friction angle. The other parameters can be derived from correlation tables. Unit weight and friction angle are created by applying a correlation coefficient. In other words, they are dependent on each other. Therefore, both data sets have a mean value, a coefficient of variation, and a correlation coefficient. Correlation is reflected by a symmetric correlation matrix where diagonal elements are unity. An example for a correlation matrix is given in Equation 4.1.

$$[C] = \begin{bmatrix} c_{11} & c_{12} & c_{13} & \dots & c_{1n} \\ c_{21} & c_{22} & c_{23} & \dots & c_{2n} \\ c_{31} & c_{32} & c_{33} & \dots & c_{3n} \\ \dots & \dots & \dots & \dots & \dots \\ c_{n1} & c_{n2} & c_{n3} & \dots & c_{nn} \end{bmatrix} \tag{4.1}$$

where $c_{11}, c_{22}, c_{33}, ..., c_{nn}$ are unity, or in other words 1.0. In addition, c_{12} and c_{21} are the correlation coefficient between the first and the second element, and they are equal. Likewise, c_{23} and c_{32} are the correlation coefficient between the second and the third element, and they are also equal, indicating that the matrix is symmetrical.

In this study, as there are only two dependent parameters, a 2x2 correlation matrix is created as is given in Equation 4.2.

$$[C] = \begin{bmatrix} 1.0 & c \\ c & 1.0 \end{bmatrix} \tag{4.2}$$

where [C] is the correlation matrix. Correlation matrix refers to the symmetric array of correlation coefficients between parameters. Moreover, c is the correlation coefficient between friction angle and unit weight. In line with the literature (see Table 2.9), in this study, it is assumed to be 0.7.

Cholesky decomposition reduces a symmetric matrix into lower and upper triangular two matrices, [L] which are transpose of each other [87]. This relation is given in Equation 4.3 for correlation matrix, [C].

$$[C] = [L][L]^T \tag{4.3}$$

If the equation is solved for any correlation coefficient, c, it is seen that the lower triangular matrix, [L], is as given in the Equation 4.4.

$$[L] = \begin{bmatrix} 1.0 & 0.0 \\ c & \sqrt{1-c^2} \end{bmatrix} \tag{4.4}$$

In order to start creating data sets, matrix multiplication between the lower triangular matrix obtained by Cholesky decomposition and an array with 2x1 unit normals (having zero mean and unit variance) should be done. Then, a dot product between these created data points and the standard deviation of the relevant parameter should be done. Finally, this deviation is added to the related parameter's mean value to generate data sets with a predefined mean value, a COV value, and correlation. A similar example is given in [91].

On the other hand, the modulus of subgrade reaction is a function of friction angle. Therefore, it is assigned to soil layers by using the procedures explained in Chapter 3.

As an illustration, these codependent variables (namely, friction angle, unit weight, modulus of subgrade reaction, and scatter of friction angle versus unit weight to show

the correlation) are given with their probability density functions for normal distribution, lognormal distribution, and uniform distribution in Figure 4.1, Figure 4.2, and Figure 4.3, respectively. In these figures, the mean value for friction angle and COV are taken 30° and 20%, respectively. Furthermore, the mean value for effective unit weight and COV are taken 10° and 5%, respectively. The correlation coefficient between them is considered 0.7. For the assessment of modulus of subgrade reaction, the non-limited k approach (see 3.4 or Figure 3.5 portion D) is considered.

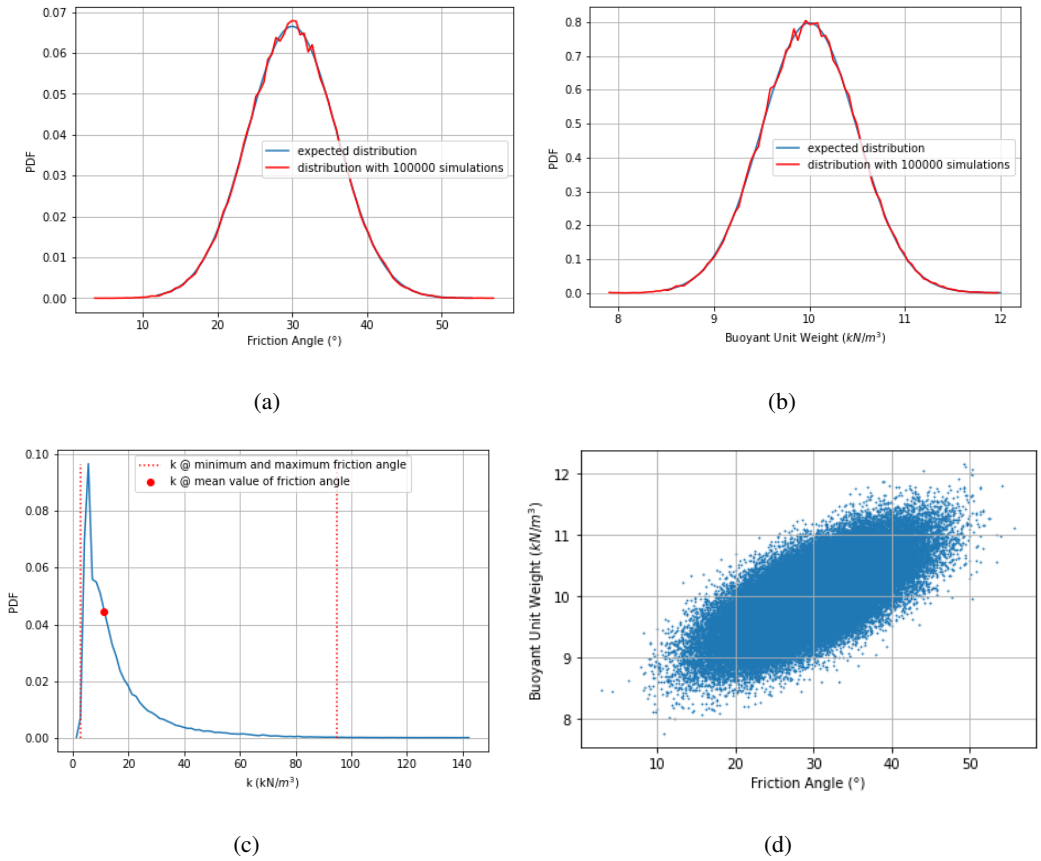

Figure 4.1: Probability of density functions for: (a) friction angle, (b) buoyant unit weight, (c) modulus of subgrade reaction. (d) Correlation between friction angle and unit weight for normal distribution

The figures show the minimum and maximum limits for the initial modulus of subgrade reaction, k, according to an expected minimum and maximum distribution values with the given mean value and COV. Moreover, the initial modulus of subgrade reaction calculated for the mean value of the friction angle is pointed on the figures as a red dot. Some abrupt changes in the k distribution can be associated with the

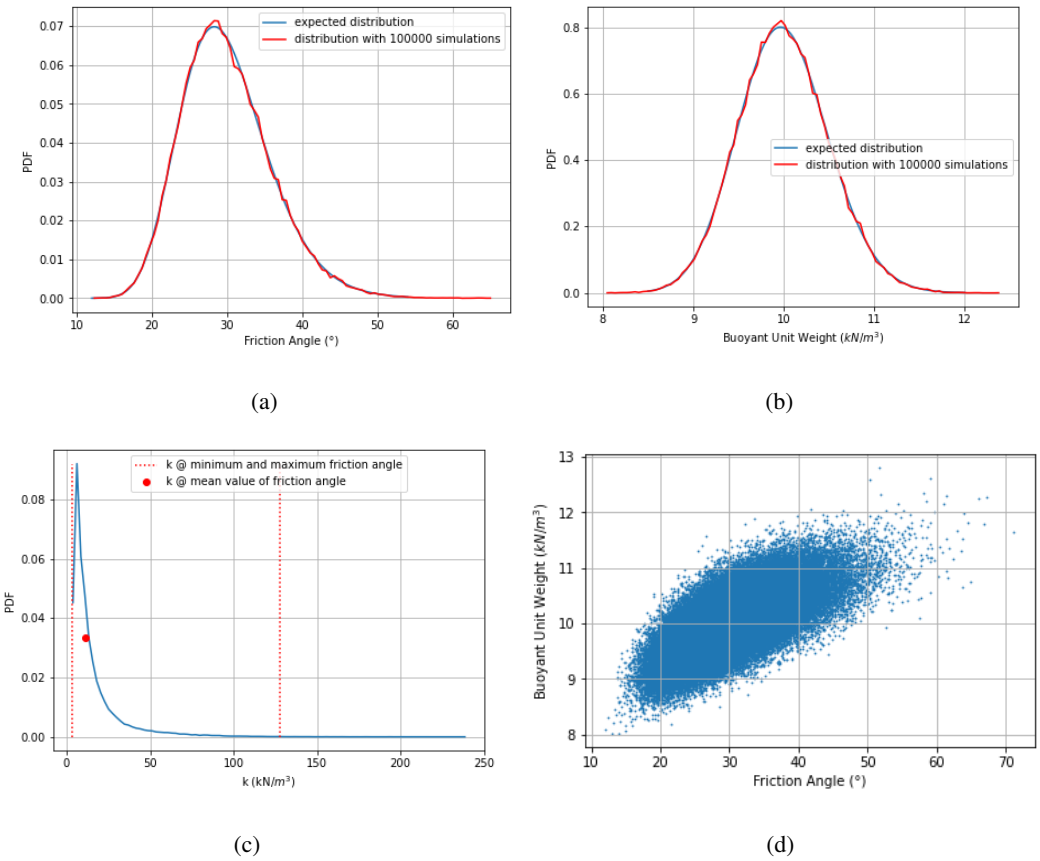

Figure 4.2: Probability of density functions for: (a) friction angle, (b) buoyant unit weight, (c) modulus of subgrade reaction. (d) Correlation between friction angle and unit weight for lognormal distribution

discontinuous nature of the k function introduced in the previous chapter (see Figure 3.5). As the function is piece-wise, the probability distribution is not smooth and shows some abrupt changes in behavior.

4.2.2 Monte Carlo simulations

As explained in the previous section, Monte Carlo Simulations are utilized to create data sets where friction angle and unit weight are considered random variables. These two parameters are correlated. Whether the simulation causes an unsatisfactory performance or not is checked for each simulation. The probability of unsatisfactory performance is considered in terms of the serviceability and ultimate limit states fol-

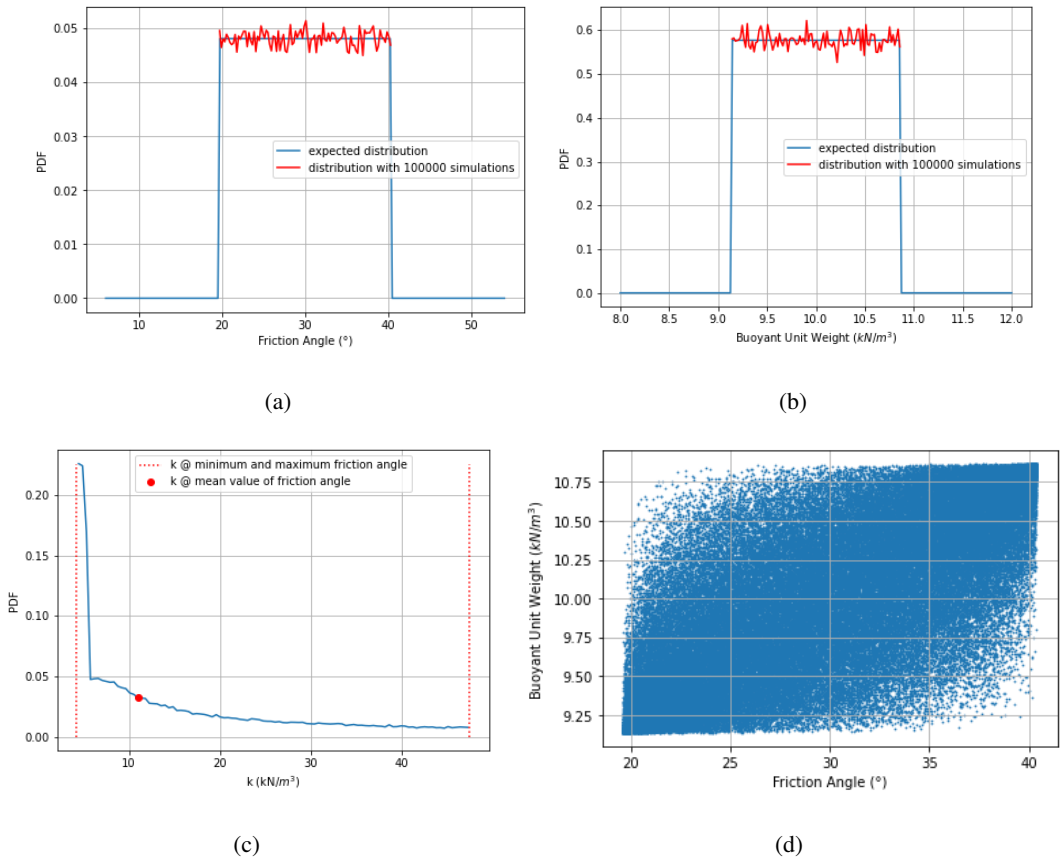

Figure 4.3: Probability of density functions for: (a) friction angle, (b) buoyant unit weight, (c) modulus of subgrade reaction. (d) Correlation between friction angle and unit weight for uniform distribution

lowing API [101] and DNV-GL[40] guidelines. In such a manner, limit values given in Table 3.1 (such as shear, combined, overload, soil bearing, and service checks) are checked.

PUP is calculated by considering limit values given in Table 3.1 (such as shear, combined, overload, soil bearing, and service checks) both individually and combined. For combined checks, a monopile is analyzed as a series system, where any unsatisfactory performance in any check directly affects overall structural performance. Hence, whenever even one condition fails to satisfy the requirements, the related trial with given soil properties is evaluated as "unsatisfactory performance.". This assumption is compatible with the literature [102]. If these criteria were set so that two or more condition failure is required for unsatisfactory performance, then PUP would

be even lower; in other words, this study considers the slightest chance of poor performance. PUP is calculated as the number of runs having unsatisfactory conditions divided by the total number of runs in Monte Carlo Simulations. For instance, for 100 simulations, each run selects randomly distributed variables. If the results show two unsatisfactory cases, that means the probability of unsatisfactory performance is 2%. As a result, the overall probability of unsatisfactory performance is calculated in percentage for a predefined number of simulations.

Because of the Monte Carlo Simulation's probabilistic behavior, a sufficient number of simulations should be run to minimize the deviation, thus, errors. In this regard, the required number of runs for analyses should be examined by checking the convergence with the increasing number of runs. Figure 4.4 shows that the results seem to converge after about 100,000 runs. This convergence implies that the number of simulations is sufficient, and the deviation becomes quite insignificant after about 100,000 runs. As the analyses have relatively low computational time, 100,000 simulations were created for the study.

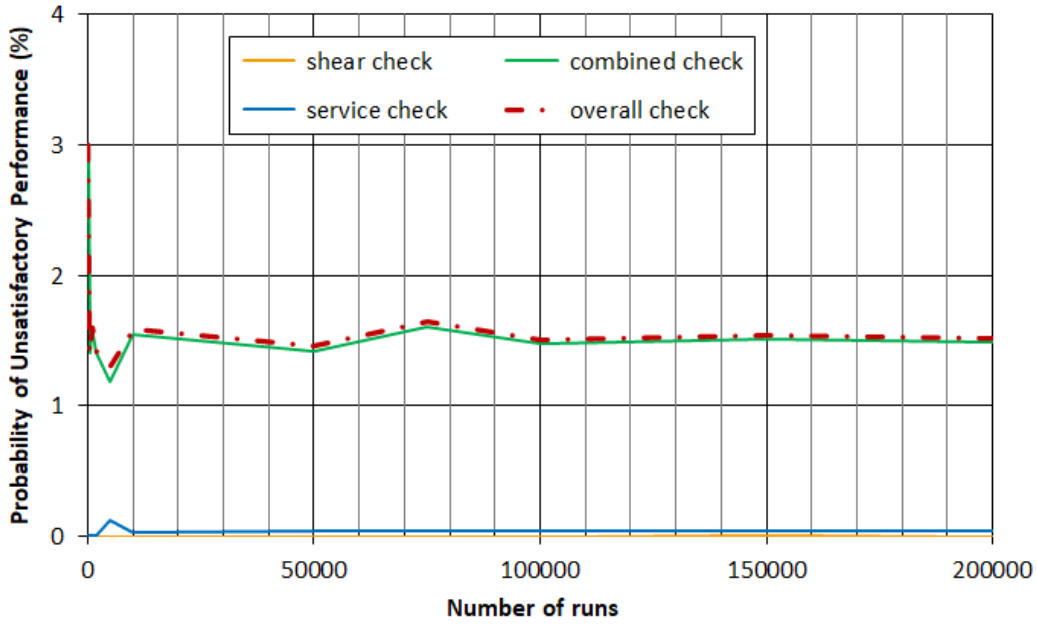

Figure 4.4: Number of runs vs. probability of unsatisfactory performance for Monte Carlo simulations

In order to create the convergence curves, for the probabilistic parameters, the COV

for friction angle is selected 40%, and for effective unit weight, the COV is 5%. The correlation coefficient between these parameters is taken as 0.7. A lognormal distribution is utilized to create the random fields.

As a reminder of the analysis parameters used in this section, Figure 4.5(a) gives the handling of the initial modulus of subgrade reaction, and Figure 4.5(b) shows the load conditions considered in the study.

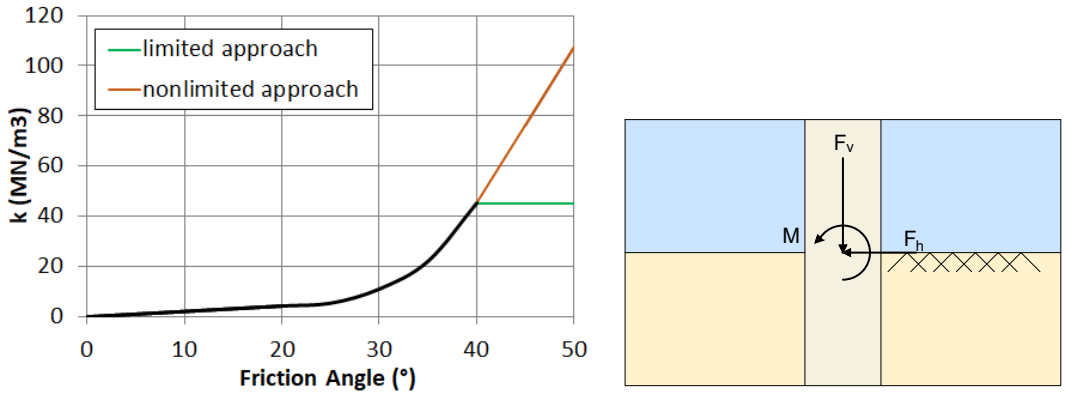

(a) (b)

Figure 4.5: Analysis parameters (a) the initial modulus of subgrade reaction, (b) load conditions

4.3 Probabilistic study for a monopile in Denmark

The effects of COV and distribution function selection on the structure's probability of unsatisfactory performance are investigated for the case study introduced in Chapter 3. Different COV values for friction angle and distribution functions are assigned to the soil layers for comparison purposes. Results for this study are given in Table 4.1 for non-limited k approach and in Table 4.2 for limited k approach. 100,000 simulations are evaluated as the convergence criteria explained in the previous sections in considered. In line with the case study, axial loading is considered as zero in this section.

Table 4.1: Probability of unsatisfactory performance (%) with different COV of friction angle with non-limited approach for modulus of subgrade reaction without axial loading for the case study in Denmark

COV	Normal Distribution				Lognormal Distribution				Uniform Distribution			
(%)	Overall	Shear	Comb.	Service	Overall	Shear	Comb.	Service	Overall	Shear	Comb.	Service
10	0.000	0.000	0.000	0.000	0.000	0.000	0.000	0.000	0.000	0.000	0.000	0.000
20	0.052	0.000	0.052	0.000	0.003	0.000	0.003	0.000	0.000	0.000	0.000	0.000
30	1.105	0.001	1.084	0.022	0.292	0.000	0.292	0.000	0.961	0.000	0.958	0.003
40	3.550	0.030	3.342	0.242	1.508	0.000	1.475	0.034	4.296	0.003	4.015	0.289
50	6.503	0.183	5.894	0.765	3.727	0.017	3.446	0.288	8.866	0.244	7.922	1.109

Table 4.2: Probability of unsatisfactory performance (%) with different COV of friction angle with limited approach for modulus of subgrade reaction without axial loading for the case study in Denmark

COV	Normal Distribution				Lognormal Distribution				Uniform Distribution			
(%)	Overall	Shear	Comb.	Service	Overall	Shear	Comb.	Service	Overall	Shear	Comb.	Service
10	0.000	0.000	0.000	0.000	0.000	0.000	0.000	0.000	0.000	0.000	0.000	0.000
20	0.020	0.000	0.020	0.000	0.000	0.000	0.000	0.000	0.000	0.000	0.000	0.000
30	0.750	0.000	0.716	0.036	0.090	0.000	0.090	0.000	0.262	0.000	0.258	0.004
40	2.684	0.006	2.455	0.264	0.724	0.000	0.690	0.034	2.984	0.000	2.712	0.283
50	5.373	0.099	4.708	0.910	2.201	0.003	1.940	0.278	7.272	0.135	6.171	1.344

Limit values given in Table 3.1 are examined for these analyses. However, as overload and soil bearing check has zero percentage failure probability for all cases, they are not given in the tables. For the probability of unsatisfactory performance (%) with different probabilistic parameters with non-limited approach for modulus of subgrade reaction with axial loading, as can be grasped from Table 4.1, the most critical check causing unsatisfactory performance is the combined axial and bending moment capacity exceeding. That means that the steel strength is exceeded in some simulations. Service limit is the second most crucial check, meaning that deformation tolerance is

exceeded in some simulations. Likewise, for the probability of unsatisfactory performance (%) with different probabilistic parameters with limited approach for modulus of subgrade reaction with axial loading, as can be seen in Table 4.2, the most critical check causing unsatisfactory performance is again the combined axial and bending moment capacity exceeding. However, PUP is relatively smaller than the cases with the unlimited initial modulus of subgrade reaction approach. These results can be associated with the increasing moment and forces as the pile gets stiffer. On the other hand, service checks are almost the same. Minor differences can be attributed to the probabilistic nature of the Monte Carlo analysis. That means that the handling of the initial modulus of subgrade reaction for higher friction angle has little to no effect on the serviceability performance check of the pile.

The distribution functions have a remarkable effect on the results. The tables clearly show that the uniform distribution causes the most critical cases. This behavior is expected as the mean and minimum values have an equal probability in the density function. Therefore, compared to a lognormal and normal distribution, the chances of getting layers with relatively low friction angle values are high. On the other hand, a normal distribution is also more critical than the lognormal distribution. This behavior is easily assessed with the nature of the distribution functions. Whereas normal distribution creates negative values, lognormal distribution only generates positive values. This behavior could be interpreted as the negative values in normal distribution being forced to be created as positive values, leading to a broader scatter of data in lognormal distribution. The monopile is bounded by more stiff springs as broader means higher random values. Therefore, the probability of failure is more negligible in lognormal distribution.

Another set of analyses is conducted by considering the vertical loading. Results for this study are given in Table 4.3 for the probability of unsatisfactory performance (%) with different probabilistic parameters with non-limited approach for modulus of subgrade reaction with axial loading and in Table 4.4 for probability of unsatisfactory performance (%) with different probabilistic parameters with limited approach for modulus of subgrade reaction with axial loading. 100,000 simulations are evaluated as the convergence criteria explained in the previous sections in considered.

Table 4.3: Probability of unsatisfactory performance (%) with different COV of friction angle with non-limited approach for modulus of subgrade reaction with axial loading for the case study in Denmark

COV	Normal Distribution				Lognormal Distribution				Uniform Distribution			
(%)	Overall	Shear	Comb.	Service	Overall	Shear	Comb.	Service	Overall	Shear	Comb.	Service
10	0.000	0.000	0.000	0.000	0.000	0.000	0.000	0.000	0.000	0.000	0.000	0.000
20	0.813	0.000	0.813	0.000	0.200	0.000	0.200	0.000	0.035	0.000	0.035	0.000
30	4.730	0.001	4.713	0.021	2.226	0.000	2.225	0.001	4.359	0.000	4.358	0.001
40	10.096	0.020	9.952	0.228	6.250	0.000	6.215	0.040	11.838	0.005	11.653	0.257
50	15.443	0.150	14.97	0.769	10.828	0.016	10.611	0.272	19.674	0.239	18.981	1.054

Table 4.4: Probability of unsatisfactory performance (%) with different COV of friction angle with limited approach for modulus of subgrade reaction with axial loading for the case study in Denmark

COV	Normal Distribution				Lognormal Distribution				Uniform Distribution			
(%)	Overall	Shear	Comb.	Service	Overall	Shear	Comb.	Service	Overall	Shear	Comb.	Service
10	0.000	0.000	0.000	0.000	0.000	0.000	0.000	0.000	0.000	0.000	0.000	0.000
20	0.677	0.000	0.677	0.000	0.109	0.000	0.109	0.000	0.000	0.000	0.000	0.000
30	4.221	0.001	4.199	0.032	1.486	0.000	1.485	0.001	3.038	0.000	3.036	0.002
40	9.303	0.012	9.109	0.281	4.734	0.000	4.710	0.030	10.488	0.001	10.26	0.307
50	14.448	0.107	13.890	0.929	8.916	0.001	8.679	0.308	18.232	0.136	17.412	1.312

It is seen from the table that results are higher than the cases without axial loading. The other interpretations done for the cases with axial loading are still valid for these analyses. Additionally, it is seen that consideration of the axial loading always gives larger PUP for all COV values and all different statistical distribution cases (e.g., when we compare Table 4.1 and Table 4.3 results).

If the data from literature is considered for the probabilistic analysis, then COV of friction angle can be taken 20% with a lognormal distribution. That selection would cause a 0.003% chance of failure as can be seen in Table 4.1. This number can be interpreted as almost zero probability of unsatisfactory performance. For the cases with axial loading, it is 0.2% as can be seen in Table 4.3. This number is greater than the case without axial loading as expected. Still, this number can be interpreted as zero probability of unsatisfactory performance.

For the same soil layering, the initial modulus of subgrade reaction values for all six layers are plotted as in Figure 4.6. For the probabilistic parameters, the COV for friction angle is selected 30%, and for effective unit weight the COV is 5%. The correlation coefficient between these parameters is taken as 0.7.

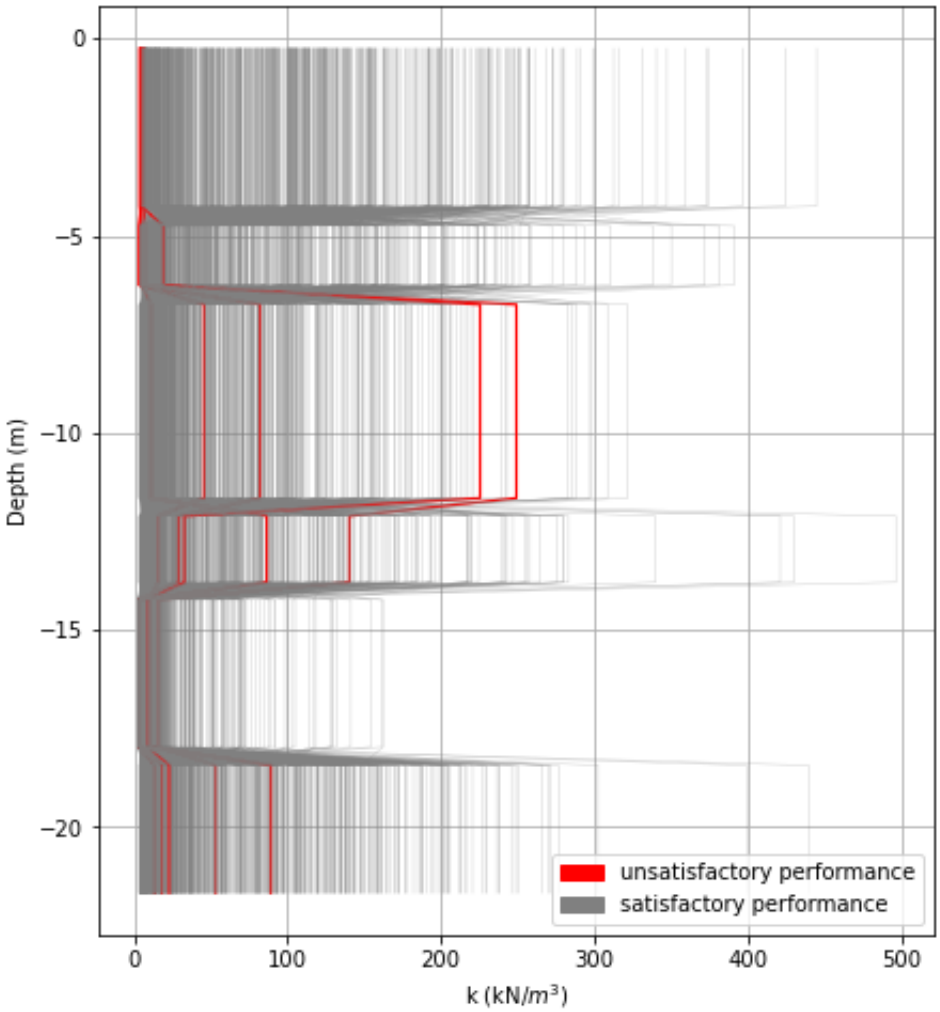

Figure 4.6: Modulus of subgrade reaction distribution along the pile

In this regard, the effect of the initial modulus of subgrade reaction on the structure's performance status (either satisfactory or unsatisfactory) is aimed to be explored. In the figure, red lines indicate the simulations showing unsatisfactory performance. It is clear from the figure that failure cases usually have 0 MN/m^3 or close to 0 MN/m^3 modulus of subgrade reaction somewhere along the pile. It is clear that this low stiffness causes large deformations.

As an additional analysis, in order to investigate the mean value effect on deterministic analyses, friction angle values of the soil layers are recalculated according to the characteristic value, which is the mean value minus the standard deviation of the soil layer for a given COV. The equation can be found in Equation 4.5.

$$\mu_{char} = \mu - \sigma = \mu - \frac{\mu\, COV}{100} \tag{4.5}$$

where,

μ : mean value

σ : standard deviation

If we consider given friction angles for the site in the case study and calculate characteristic values for each layer for changing COV values, we will obtain the values in Table 4.5. Friction angles given in the table are for the uppermost soil layer, which is 45.4°.

It is seen from the table that with 50% of COV for characteristic value, the monopile can not satisfy the serviceability limits; in other words, it shows excessive deformations (e.g., greater than 4 cm according to DNV-GL guideline for a monopile diameter of 4 meters). The behavior of the deformations with the COV increment is polynomial. The trends can be found in Figure 4.7 for different statistical distributions.

4.4 Probabilistic study for a monopile in Belgium

A monopile is designed in the light of API [101] and DNV-GL [40] guidelines in Belgium offshore. Location is selected considering the total length of the CPT data

Table 4.5: Analysis results with characteristic value for friction angle

COV (%)	Performance Result	Tip Displacement (m)	Characteristic Value of Friction Angle (°)
0	satisfactory	0.030	45.4
10	satisfactory	0.036	40.9
20	satisfactory	0.052	36.3
30	satisfactory	0.081	31.8
40	satisfactory	0.136	27.2
50	unsatisfactory	0.299	22.7

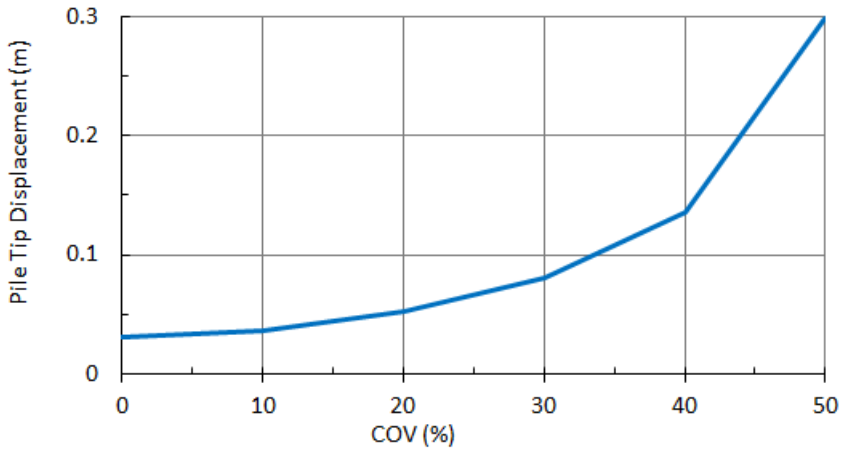

Figure 4.7: Pile tip deformations for different COV values of friction angle

available, provided by Databank Ondergrond Vlaanderen [3]. The chosen point has a Cone Penetration Test (CPT) data named ST-18/026-SZB11. It is electrical with a total depth of 30.38 meters. The location of this CPT is given in Figure 4.8. The related coordinates are X=77455.4 and Y=232728.6. CPT also has pore pressure measurement; thus, it is also called CPTU. Ground elevation is -10,73 m below the mean sea level.

The closest borehole to this CPT location is about 300 m away from the CPT location and named as GEO-76/484-b125. The total depth is 5.15 m. The ground elevation of

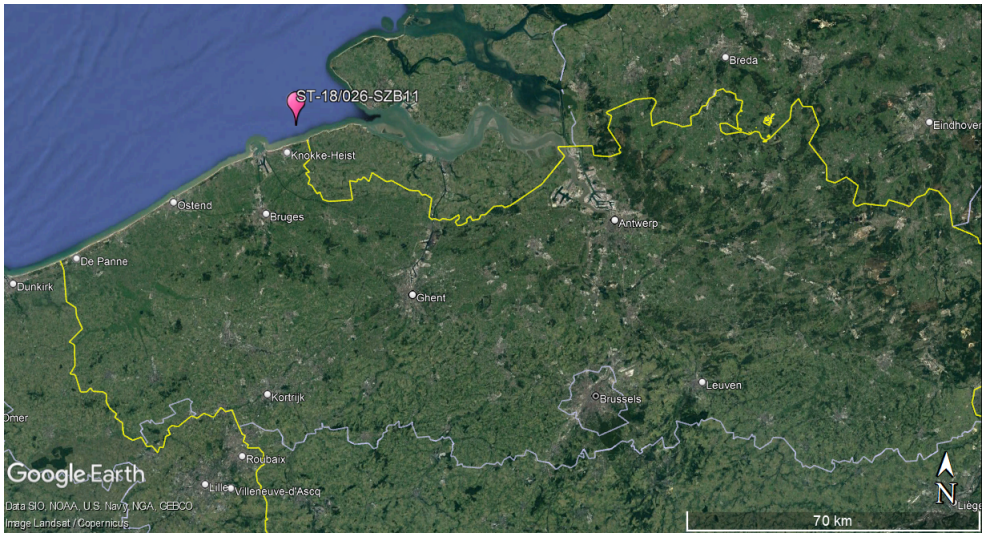

Figure 4.8: Selected CPT location in Belgium offshore

this borehole is -15.20 m. The related borehole sketch is given in 4.9.

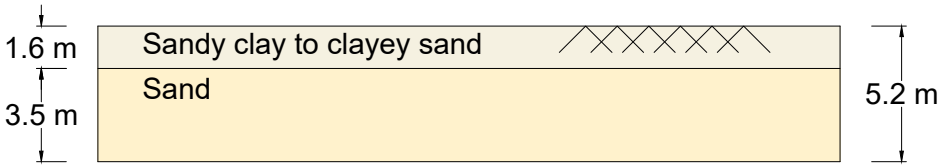

Figure 4.9: Borehole data near to the selected CPT location

The soil profile is mainly sand; however, there are thin clay layers between thick sand layers. These small portioned clay layers are omitted for the analyses. Additionally, the borehole depth is insufficient in terms of depth. Therefore, a correlation from the literature should be made to estimate soil parameters.

4.4.1 Soil idealization and material properties

Initially, the soil layers are idealized. Typically, idealization should be made by comparing in-situ test results and laboratory results. However, as the offshore data is limited, only CPT data is employed for this analysis. Soil classification is completed according to the Robertson soil classification chart [98, 96]. The chart used for the study is given in Figure 4.10.

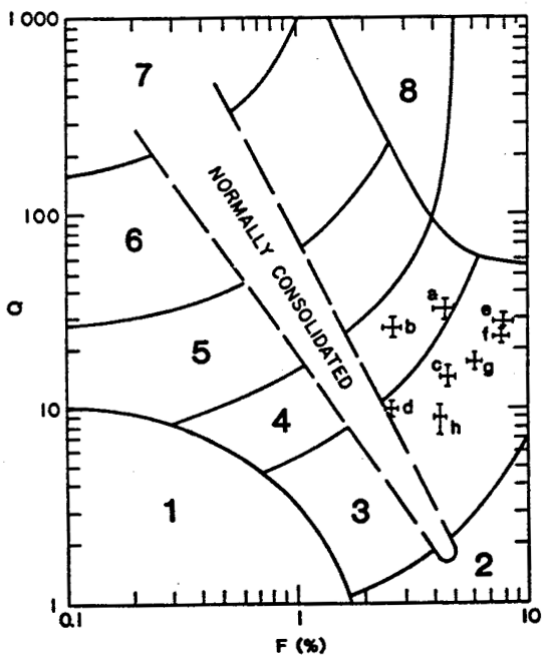

Figure 4.10: Soil classification charts by Robertson [96]

where soil behavior types are:

1- Sensitive, fine grained

2- Organic soils – peats

3- Clays – clay to silty clays

4- Silt mixtures

5- Sand mixtures

6- Sands

7- Gravelly sand to sand

8- Very stiff sand to clayey sand

While completing soil classification, material properties should also be calculated. Only the friction angle and the unit weight are subjects of interest as they are the only required parameters for the p-y method. Thus, the correlation charts in the literature are to be used to get the friction angle and unit weight of the layers. The correlation

chart to get friction angle from CPT data is formed by Jaeger and Maki [58], and it is given in Figure 4.11.

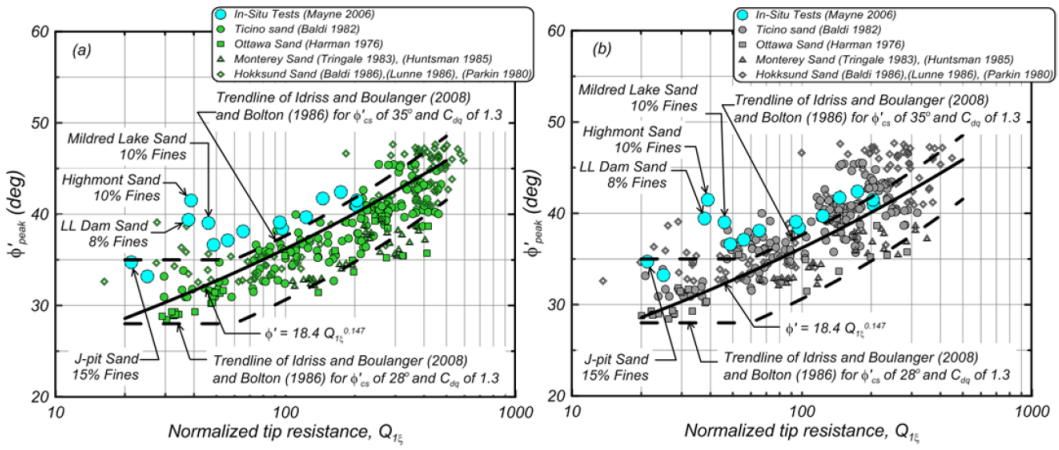

Figure 4.11: CPT tip resistance versus friction angle correlation graph with different calibration chamber corrections [58]

Both figures in Figure 4.11 with different calibration chamber corrections give the same equation to calculate peak friction angle from normalized tip resistance. The related formula is shown in Equation 4.6 [58].

$$\phi'_{peak} = 18.4\, Q_{1\zeta}^{0.147} \tag{4.6}$$

where

ϕ'_{peak} : peak friction angle

$Q_{1\zeta}$: the net tip resistance that a soil at a given initial state condition would have at a reference stress of $\sigma_{v0} = P_a$

$Q_{1\zeta}$ formula is given in Equation 4.7.

$$Q_{1\zeta} = \frac{q_t - \sigma_{v0}}{P_a}\, C_{N\zeta} \tag{4.7}$$

where

q_t : CPT tip resistance

$C_{N\zeta}$: mapping function

P_a : atmospheric pressure

σ_{v0} : vertical stress

The Boulanger and Idriss $C_{N\zeta}$ factor [23] formula is given in Equation 4.9.

$$C_{N\zeta} = C_\zeta C_{Ne} \tag{4.8}$$

where C_{Ne} is defined as given in Equation 4.9.

$$C_{Ne} = \left(\frac{P_a}{\sigma_{v0}}\right)^{0.784-0.521\,D_{R0}} \tag{4.9}$$

where D_{R0} is the initial relative density. The paper also states a formula for D_{R0}. This formula is given in Equation 4.10.

$$D_{R0} = 0.465\,\left(\frac{Q_{1e}}{1.3}\right)^{0.264} - 1.063 \tag{4.10}$$

Q_{1e} formula is given in Equation 4.11. As there is a circular reference between D_{R0} and Q_{1e}, D_{R0} value can be calculated by trial and error, satisfying this circular reference.

$$Q_{1e} = \frac{q_t - \sigma_{v0}}{P_a}\,C_{Ne} \tag{4.11}$$

Moreover, C_ζ factor can be calculated as given in Equation 4.12.

$$C_\zeta = \left(\frac{D_{R0} - \Delta D_{R,CS} + 1.063}{D_{R0} + 1.063}\right)^{3.788} \tag{4.12}$$

where $D_{R,cs}$ is calculated as given in Equation 4.13.

$$\Delta D_{R,cs} = \frac{1}{Q - ln\left(100\frac{1+2K_0}{3}\frac{\sigma'_{v0}}{P_a}\right)} - \frac{1}{Q - ln\left(100\frac{1+2K_0}{3}\right)} \tag{4.13}$$

where K_0 is the coefficient of earth pressure at rest. Here it is taken as 0.4, following the initial assumption made. In addition, Q is an empirical factor and is taken as 10.

Before using these correlations, the validity of the correlation between peak friction angle and normalized tip resistance should be investigated by regional soil data. Databank Ondergrond Vlaanderen [3] is employed with borehole data. 15 points located in sand to sandy soils in this database are scattered on the same figure provided by Jaeger and Maki [58]. This plot is shown in Figure 4.12. In the figure, red dots represent the Belgium onshore data points. Points used in the analysis are given in Table 4.6 with properties.

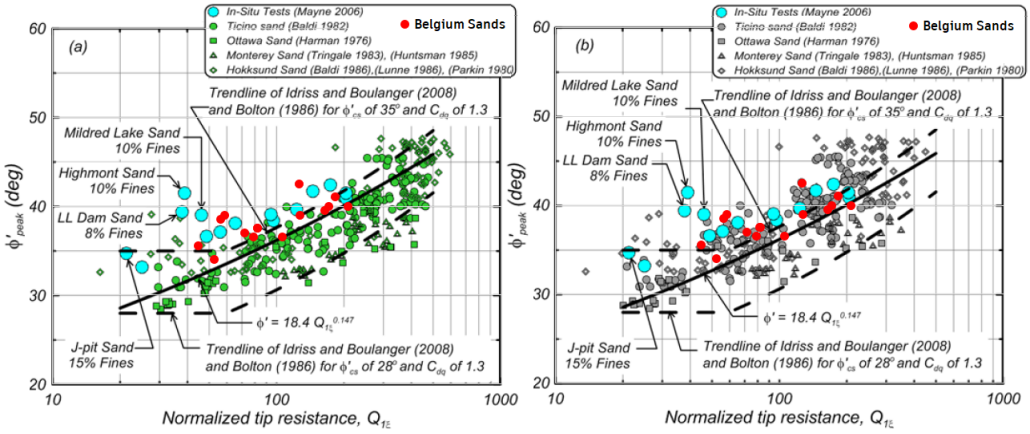

Figure 4.12: CPT tip resistance versus friction angle correlation graph with different calibration chamber corrections with Belgium soil data

It is clear from Figure 4.12 that the equation could be safely used for Belgium soil data as the Belgium data points and previously marked points are in agreement.

Unit weight for a layer is calculated by using the Robertson correlation charts [97]. These charts are given in Figure 4.13

There is also an equation available for this relationship. It is given in Equation 4.14.

$$\frac{\gamma}{\gamma_w} = 0.27\ log(R_f) + 0.36\ log\left(\frac{q_t}{P_a}\right) + 1.236 \tag{4.14}$$

where R_f is the CPT friction ratio (i.e., $(f_s/q_t)\ 100\%$), and γ_w is the unit weight of water which is 9.81 kN/m^3.

Table 4.6: Belgium CPT and Borehole data used in Figure 4.12 [3]

Borehole	CPT	Distance (m)	x	y
GEO-10/140-B28	GEO-10/139-S28	1	68645,38	223513,85
GEO-10/140-B37	GEO-10/139-S37	3	68888,22	223227,25
GEO-10/140-B39	GEO-10/139-S39	12	68902,96	222802,71
GEO-10/140-B41	GEO-10/139-S41	3	68934,05	222697,35
GEO-10/140-B45	GEO-10/139-S45	15	68926,40	222503,40
GEO-10/140-B72	GEO-10/139-S69	35	69062,57	221810,29
GEO-10/140-B89	GEO-10/139-S89	2	68222,50	224571,00
GEO-10/140-B112	GEO-10/139-S112	4	68507,00	223737,302

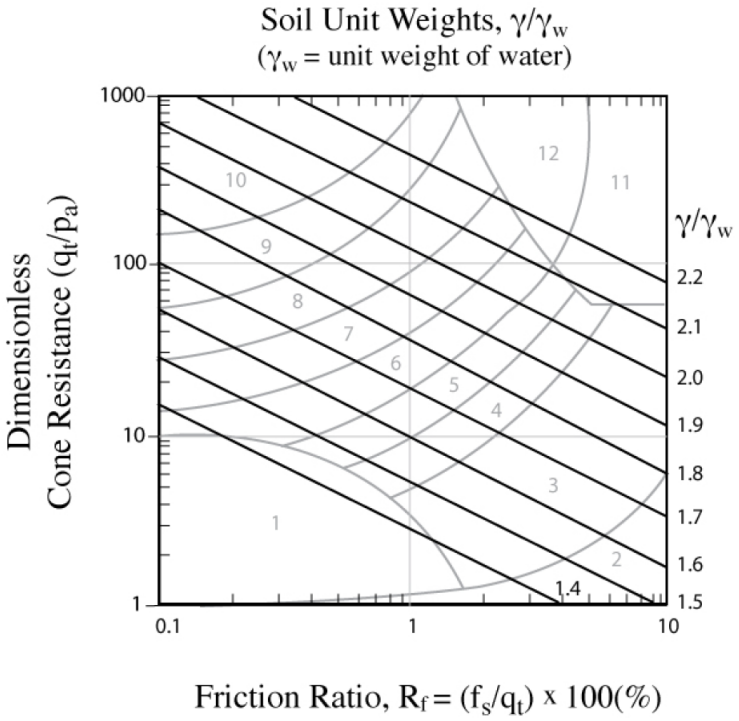

Figure 4.13: Correlation between CPT results and unit weight [97]

Following the calculation of the parameters, the analysis can be conducted by any given monopile geometry. The soil idealization on CPT data as mentioned above is shown in Figure 4.14.

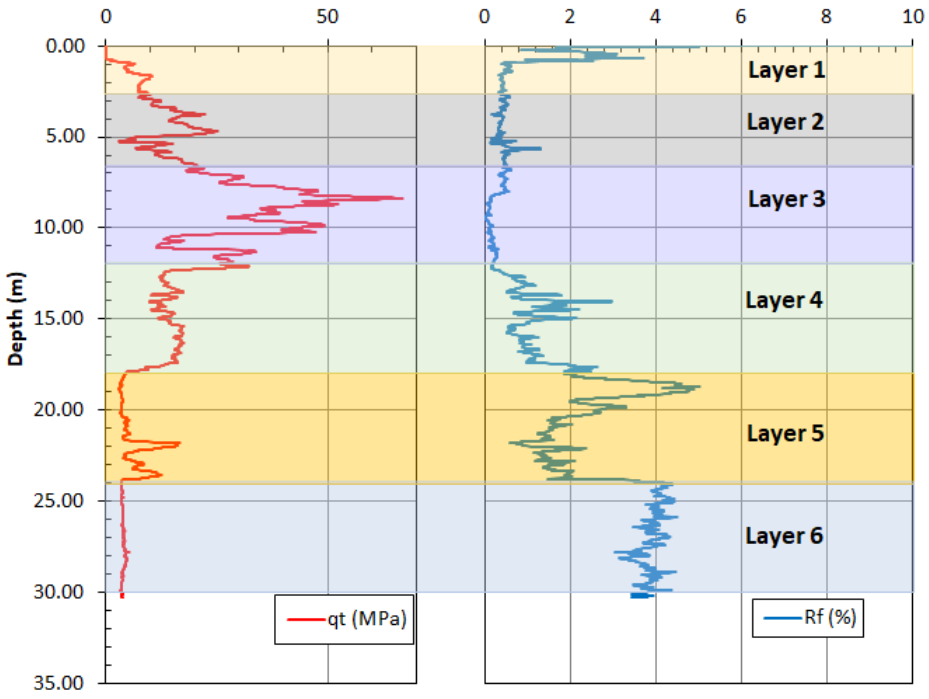

Figure 4.14: Idealized soil data on CPT data in Belgium offshore

The Robertson's chart and the sketch of this idealization with related geotechnical parameters and designed monopile are given in Figure 4.15 and Figure 4.16, respectively. Although Layer 3 is clay, it is treated as sand for the study.

4.4.2 Monopile design

A monopile for the same turbine with the case study is designed (see Chapter 3 for details). It is a Vestas V80-2.0 MW model with 3 bladed rotors and an 80 m rotor diameter. The monopile is designed considering all the design checks presented by the guidelines (see Table 3.1). The aim is to find the geometry which shows satisfactory performance under given boundary conditions. Note that an optimization study could also be done for that purpose. However, as it is beyond the scope of this study, geometry is selected based on engineering judgment. The designed monopile with

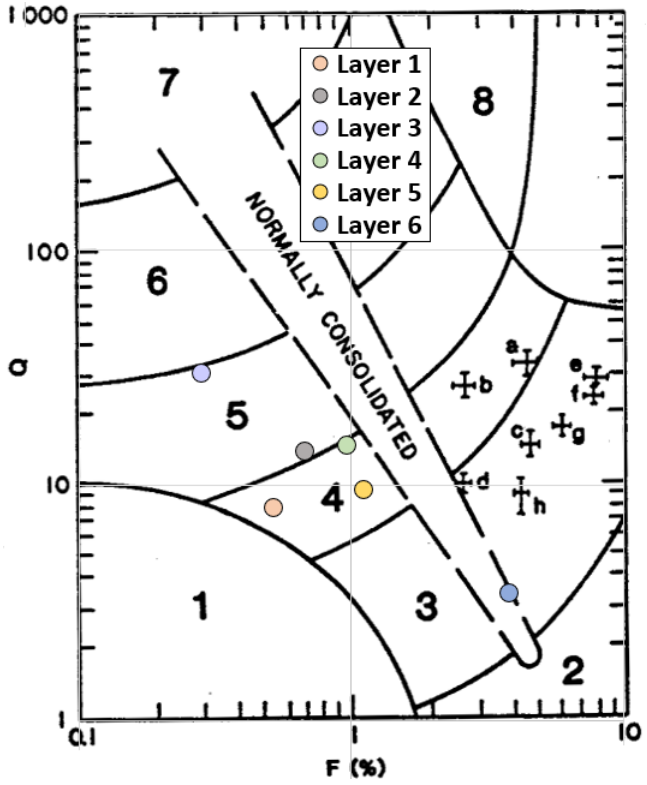

Figure 4.15: Robertson chart for the CPT in Belgium offshore

dimension and properties is given in Figure 4.17. It shows a zero percentage of unsatisfactory performance under the issued design checks and the same loading with the case study. The monopile is laterally loaded in static conditions. The tower and monopile weight are considered as axial loading.

4.4.3 Probabilistic analysis

The effects of COV and distribution selection on the probability of unsatisfactory performance is examined for this monopile. This time, both the soil data available in the literature for the Belgium coast and actual soil data for that region are considered in selecting probabilistic parameters.

With the site data, the mean values of friction angles for each layer is given in Figure 4.16, and COV of the friction angle is found to be 10.5% for the first layer, 4.7% for the second layer, 5.8% for the third layer, 4.7% for the fourth layer, 7.6% for the fifth layer, 1.8% for the sixth layer. The maximum COV for the friction angle of these

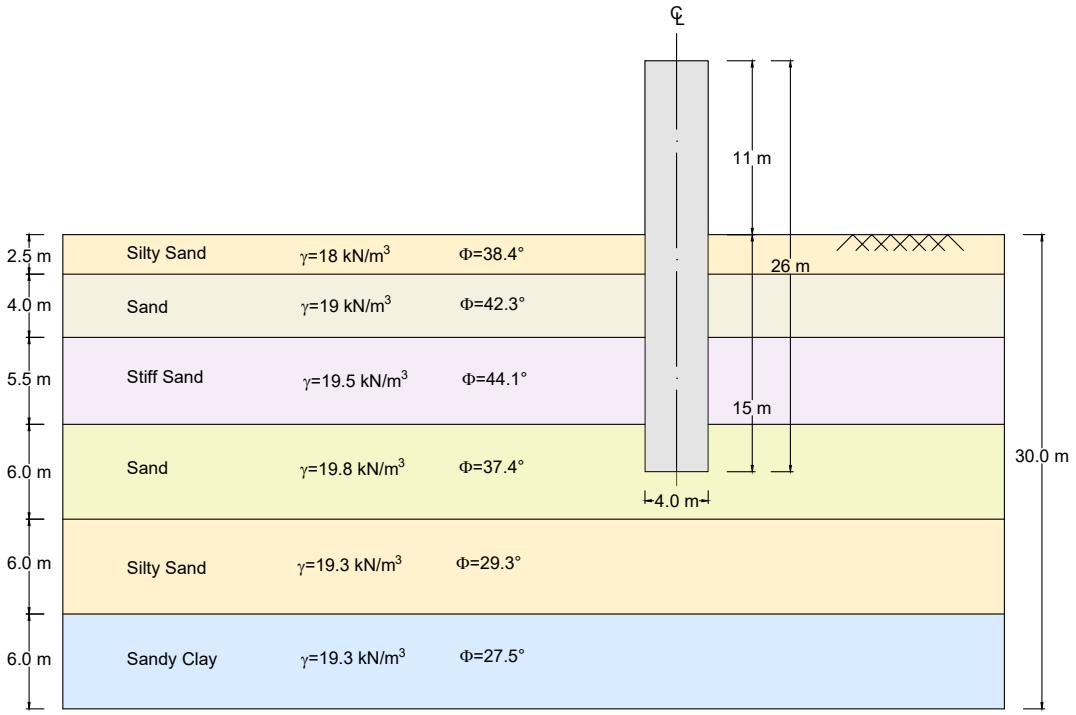

Figure 4.16: Idealized soil sketch for the CPT in Belgium offshore with designed monopile

sixth layers is used as the COV of the analyses, which is 10.5%.

As an illustration, these codependent variables (namely, friction angle, unit weight, modulus of subgrade reaction, and scatter of friction angle versus unit weight to show the correlation) are given for Layer 3 with their probability density functions for normal distribution, lognormal distribution, and uniform distribution in Figure 4.18, Figure 4.19, and Figure 4.20, respectively. In these figures, the COV for friction angle is taken as 10.5%. Furthermore, the COV for effective unit weight is taken 5%. The correlation coefficient between them is considered 0.7.

The figures show the minimum and maximum limits for the initial modulus of subgrade reaction, k, according to an expected minimum and maximum distribution values with the given mean value and COV. Moreover, the initial modulus of subgrade reaction calculated for the mean value of the friction angle is pointed on the figures as a red dot. Some abrupt changes in the k distribution can be associated with the discontinuous nature of the k function introduced in the previous chapter (see Figure

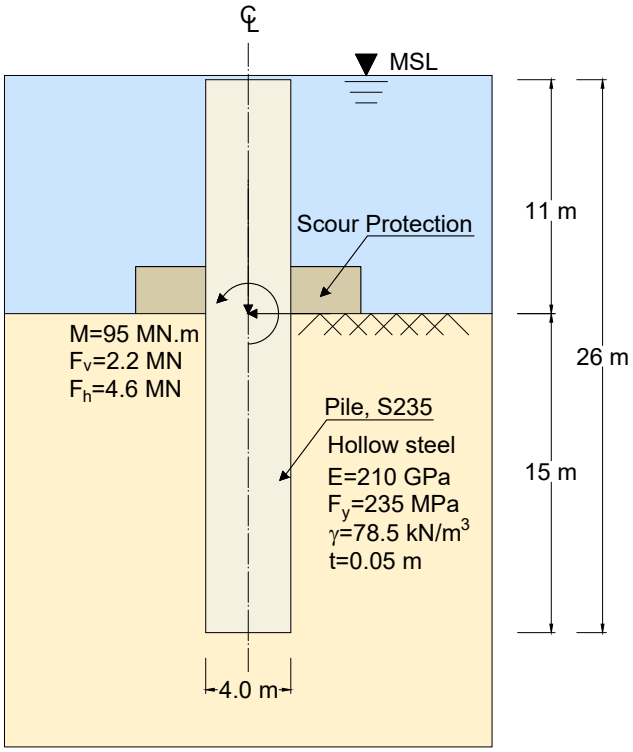

Figure 4.17: The designed monopile geometry and properties on Belgian offshore

3.5). As the function is piece-wise, the probability distribution is not smooth and shows some abrupt changes in behavior.

10.5% is given as the final COV of friction angle for all layers. That selection would cause a 12.6% chance of failure for normal distribution, 12.5% chance of failure for lognormal distribution, and 12.1% chance of failure for uniform distribution. The main issue causing unsatisfactory performance is serviceability, followed by bearing check. These numbers are higher than the ones calculated with the case study. Besides, as the friction angle values of the layers are pretty high, and its COV is relatively low, now the effect of the distribution function is changed. As this monopile is designed in the scope of this thesis, an optimal monopile mass was the only consideration. However, results indicate that design should also involve space for variability and uncertainty.

Inspecting the values from the literature, COV of the friction angle for this area is expected to be around 10%. That selection would cause to almost similar results. Hence, the expected PUP for this case is 12%.

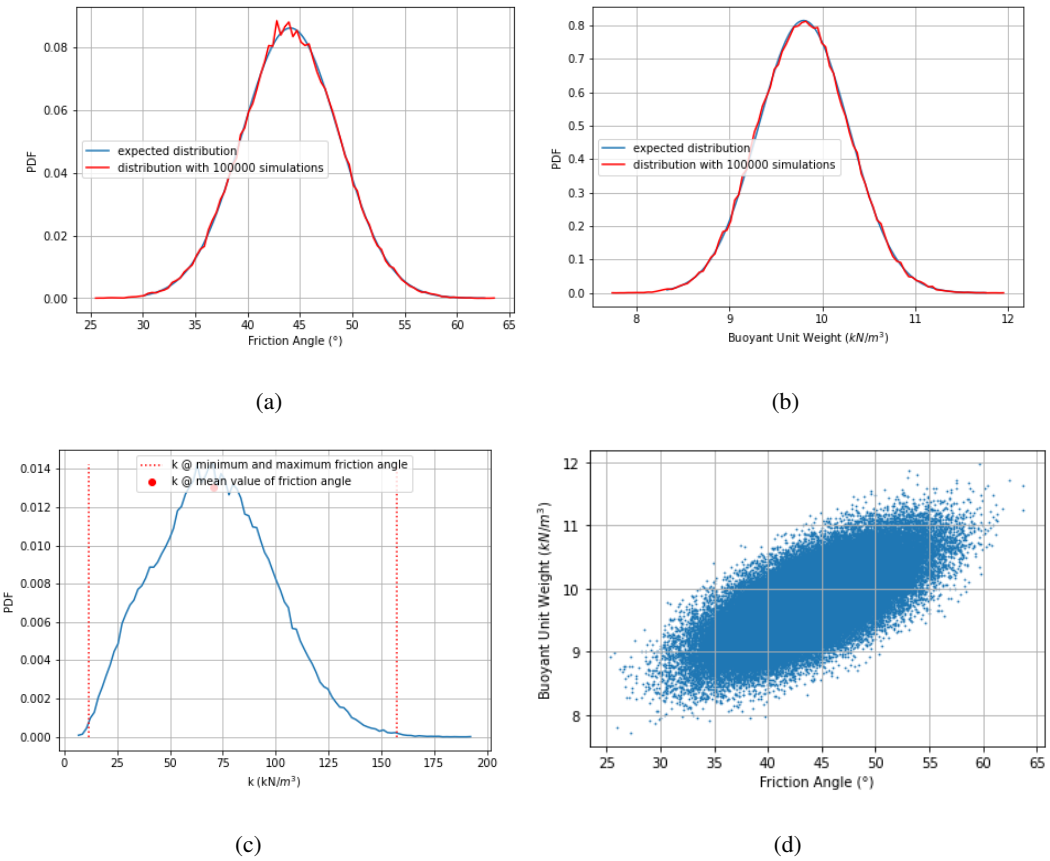

Figure 4.18: Probability of density functions for: (a) friction angle, (b) buoyant unit weight, (c) modulus of subgrade reaction. (d) Correlation between friction angle and unit weight for normal distribution

4.5 Discussion and conclusions

In the analyses, both limited and the non-limited k approach (check Equation 3.3 and 3.4 or see Figure 3.5 portion C and D for limited and unlimited k approach, respectively) is concerned for the assessment of modulus of subgrade reaction. Therefore, there might be unrealistically high stiffness values for a relatively high COV for the friction angle with non-limited k approach. In both cases, overload and soil bearing check has zero percentage failure probability. For both limited and non-limited approaches for modulus of subgrade reaction, the most critical check causing unsatisfactory performance is the exceeded combined axial and bending moment capacity. That means that the steel strength is exceeded in some simulations. Service limit is the

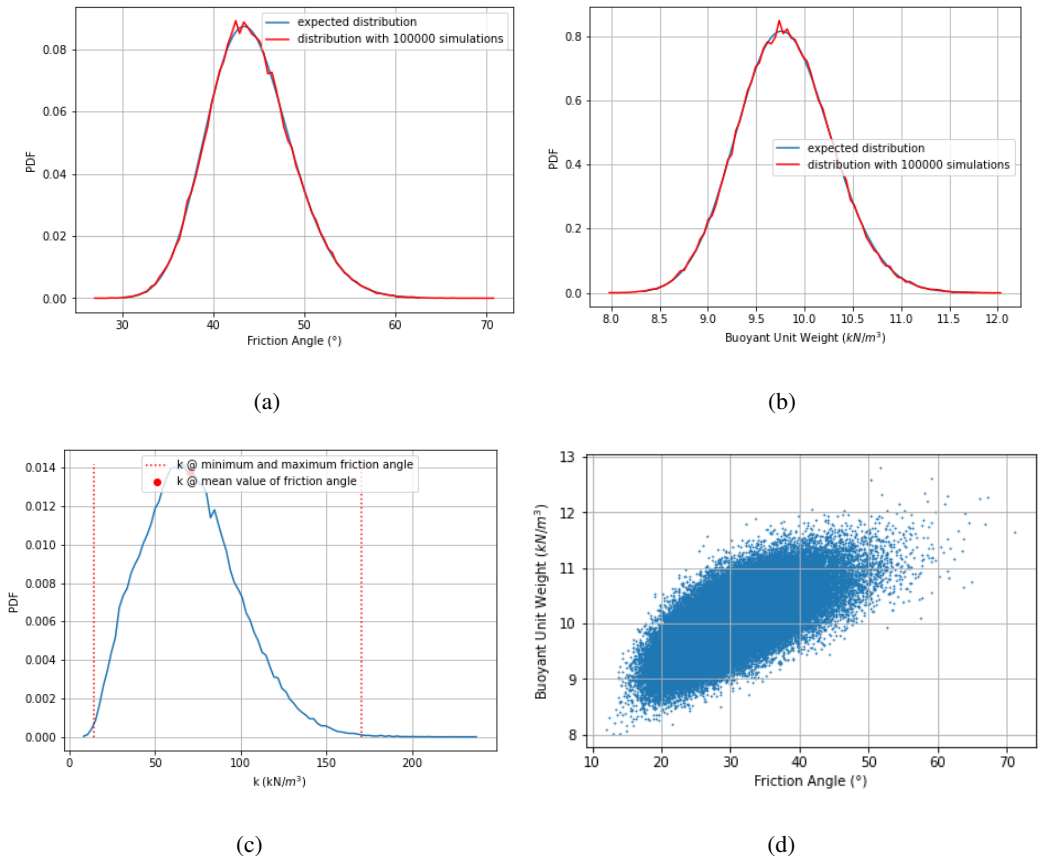

Figure 4.19: Probability of density functions for: (a) friction angle, (b) buoyant unit weight, (c) modulus of subgrade reaction. (d) Correlation between friction angle and unit weight for lognormal distribution

second most crucial check, meaning that deformation tolerance is exceeded in some simulations. However, PUP is relatively more minor for the limited approach than the cases with the unlimited initial modulus of subgrade reaction approach. These results can be associated with the increasing moment and forces as the pile gets stiffer. On the other hand, service checks are almost the same. Slight differences can be attributed to the probabilistic nature of the Monte Carlo analysis. That means that the handling of the initial modulus of subgrade reaction for higher friction angle has little to no effect on the serviceability performance check of the pile.

Results show that although the selection of these probabilistic parameters, such as COV and distribution function, play a role in the results, consideration of seabed soil variability and uncertainty does not significantly affect the PUP for the sandy

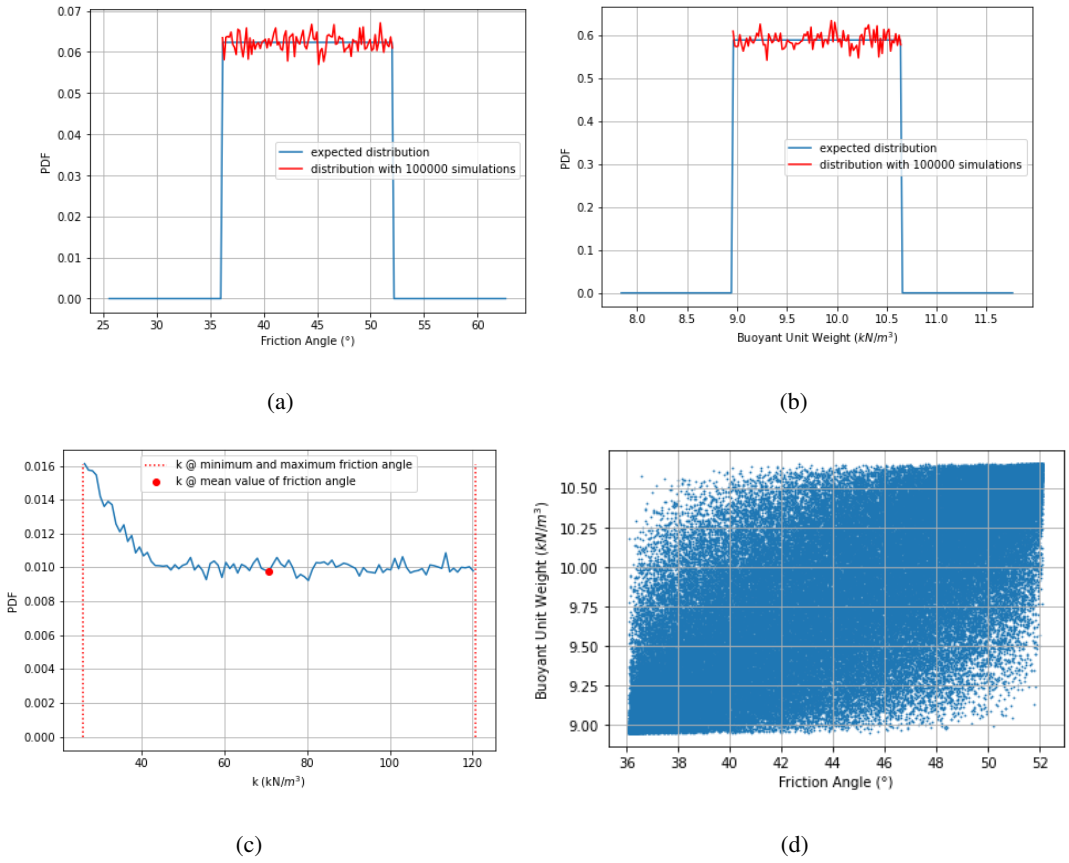

Figure 4.20: Probability of density functions for: (a) friction angle, (b) buoyant unit weight, (c) modulus of subgrade reaction. (d) Correlation between friction angle and unit weight for uniform distribution

soils in Belgium case in this study. This behavior can be understood from the tables. For instance, even with 50% COV, which is relatively high, the maximum PUP is 5.38% for normal distribution, 2.2% for lognormal distribution, and 7.3% for uniform distribution for the case study. Furthermore, selecting the soil parameter distribution function is vital as it has remarkable effects on the results.

On the other hand, for the designed monopile, a relatively high probability of unsatisfactory performance is observed. Although there was no implemented optimization method, monopile mass tried to be kept small considering the pile tip displacement. The wind turbine designed in Belgium offshore has the same material properties and loading conditions as the case study given in the Denmark case. Only the length of the monopile is adjusted to satisfy design checks for the deterministic analysis. On

the design, the limit checks introduced in this study are applied. The main issue causing unsatisfactory performance is serviceability, followed by bearing check. PUP is expected to be around 12%, which is relatively high for this small COV value. The high percentage of the probability of unsatisfactory performance can be attributed to the Danish conditions assumed for the case. In the end, results indicate that design should also involve space for variability and uncertainty.

CHAPTER 5

CONCLUSIONS AND FUTURE RECOMMENDATIONS

In the scope of the thesis, offshore wind turbines as a source of renewable energy with a particular emphasis on the ones having a monopile foundation are introduced. Available design methods and guidelines to design such structures are summarized. In the light of American Petroleum Institute (API) [101] and Det Norske Veritas - Germanischer Lloyd (DNV-GL) [40] guidelines, an analysis method is developed to check whether the system shows satisfactory performance or not. These performance measures include shear, combined, overload, soil bearing, and service checks. If all these checks are satisfied, the system is evaluated as satisfactory. On the other hand, if even one of the checks fails to meet the necessary condition, the system is evaluated as showing unsatisfactory performance. However, for sands, as the only variable to be used in the analysis is friction angle, selecting this value is crucial. Therefore, a probabilistic analysis is conducted to account for the uncertainty in the soil properties. Monte Carlo Simulation is implemented to examine a predefined number of samples. Each sample has different material properties, depending on the distribution, mean value, and coefficient of variation (COV). In the end, for a given COV, the probability of unsatisfactory performance (PUP) is evaluated.

The research question of this thesis is answered by taking into account the COV and probabilistic distribution of a given soil layering to consider the uncertainty in estimating soil parameters in offshore monopile design. A methodology is developed to ensure safe and economical monopile design.

A monopile utilizing a Monte Carlo simulation by introducing COV to soil properties is designed. The uncertainty in terms of statistical variation of soil material properties by introducing coefficients of variation is quantified with selected probability distri-

bution functions from the literature and real sites. The probability of unsatisfactory performance with the selected probabilistic parameters is observed.

For both limited and non-limited approaches for modulus of subgrade reaction, the most critical check causing unsatisfactory performance is the combined axial and bending moment capacity exceeding the case study. That means that the steel strength is exceeded in some simulations. Service limit is the second most crucial check, meaning that deformation tolerance is exceeded in some simulations. However, PUP is relatively more minor for the limited approach than the cases with the unlimited initial modulus of subgrade reaction approach. These results can be associated with the moment and force increment as the pile gets stiffer. On the other hand, service checks are almost the same. Slight differences can be attributed to the probabilistic nature of the Monte Carlo analysis. That means that the handling of the initial modulus of subgrade reaction for higher friction angle has little to no effect on the serviceability performance check of the pile.

On the other hand, for the designed monopile in Belgium, a relatively high probability of unsatisfactory performance is observed. Although there was no implemented optimization method, monopile mass tried to be kept small considering the pile tip displacement. On the design, the limit checks introduced in this study are applied. The main issue causing unsatisfactory performance is serviceability, followed by bearing check. PUP is expected to be around 12%, which is relatively high for this small COV value for friction angle. The difference in PUP can be attributed to the assumed Danish conditions. There is no set standard for defining an "acceptable max. level of PUP" in the offshore geotechnical practice. However, as risk and reliability concepts gain more attention, an acceptable level of risk and which parties must be in charge of remediation of this risk may become critical. In the end, results indicate that design should also involve space for variability and uncertainty.

The main conclusions of this research is, for the sandy soil profiles with relatively small diameters of monopiles considered in this study:

1. Seabed soil variability can affect the probability of unsatisfactory performance (PUP) depending on the specific soil conditions (i.e., Denmark Case Study: PUP < 1%, Belgium Case Study: PUP 12%).

2. The selection of soil parameter distribution function can have an effect on PUP for high COV values.

The novelty of this thesis is that a site-specific statistical analysis is conducted. Therefore, it aims to give more realistic results on interpreting the probability of unsatisfactory performance of monopile in sand. This thesis only evaluates the monopiles under static loading in sandy soils. Therefore, further studies are needed for the locations, including clay or clayey soil content. Moreover, for mixed soil layering (both sandy and clayey soils), layering correction methods (such as the method of Georgiadis [46]) should be applied. Furthermore, only static loading is considered in simple conditions (scour effect is omitted for the calculations). For future studies, mixed soil layering under the effect of both monotonic and cyclic loading should be investigated. As the scouring effect is essential, it is also advised to be examined in future studies. This study is conducted in light of the API and DNV-GL guidelines, which are invalid after 4-5 m of pile diameter. Therefore, in consideration of large diameter monopiles, this should be taken into account.

REFERENCES

[1] 68–95–99.7 rule. https://en.wikipedia.org/wiki/68-95-99.7_rule#cite_note-2, n.d. Accessed: 2022-01-15.

[2] Continuous uniform distribution. https://en.wikipedia.org/wiki/Continuous_uniform_distribution, n.d. Accessed: 2022-01-15.

[3] Databank ondergrond vlaanderen. https://www.dov.vlaanderen.be/portaal/?module=verkenner, n.d. Accessed: 2021-11-16.

[4] Geostatistical analysis for offshore windfarms. https://ramboll.com/-/media/files/rgr/documents/markets/transport/g/geophys/20_datablad_geostastistic_offshore_vb.pdf?la=en, n.d. Accessed: 2022-03-01.

[5] Geotechnical analysis special interest group learning path. https://learn.bentley.com, n.d. Accessed: 2022-01-05.

[6] N depth: Cost imperative drives monopiles to new depths. https://www.windpowermonthly.com/article/1210058/depth-cost-imperative-drives-monopiles-new-depths, n.d. Accessed: 2022-02-20.

[7] Offshore wind energy. https://windeurope.org/policy/topics/offshore-wind-energy/, n.d. Accessed: 2021-12-30.

[8] Pearson correlation coefficient. https://en.wikipedia.org/wiki/Pearson_correlation_coefficient, n.d. Accessed: 2022-01-15.

[9] Vestas v80-2.0. https://en.wind-turbine-models.com/turbines/19-vestas-v80-2.0, n.d. Accessed: 2021-11-12.

[10] E. E. Alonso. Risk analysis of slopes and its application to slopes in canadian sensitive clays. *Geotechnique*, 26(3):453–472, 1976.

[11] L. V. Andersen, M. Vahdatirad, M. T. Sichani, and J. D. Sørensen. Natural frequencies of wind turbines on monopile foundations in clayey soils—a probabilistic approach. *Computers and Geotechnics*, 43:1–11, 2012.

[12] A. S. Ang. Probability concepts in engineering planning and design. *Basic Concepts*, 1, 1975.

[13] M. Arshad and B. C. O'Kelly. Analysis and design of monopile foundations for offshore wind-turbine structures. *Marine Georesources & Geotechnology*, 34(6):503–525, 2016.

[14] A. H. Augustesen, K. Brødbaek, M. Møller, S. P. H. Sørensen, L. B. Ibsen, T. S. Pedersen, and L. Andersen. Numerical modelling of large-diameter steel piles at horns rev. In *Proceedings of the Twelfth International Conference on Civil, Structural and Environmental Engineering Computing*. Civil-Comp Press, 2009.

[15] G. S. Babu and A. Srivastava. Reliability analysis of allowable pressure on shallow foundation using response surface method. *Computers and Geotechnics*, 34(3):187–194, 2007.

[16] G. Baecher and J. Christian. Reliability and statistics in geotechnical engineering-john wiley and sons, chichester. 2003.

[17] S. A. Barakat, A. I. H. Malkawi, and H. T. Ra'ed. Reliability-based optimization of laterally loaded piles. *Structural safety*, 21(1):45–64, 1999.

[18] D. E. Becker. Eighteenth canadian geotechnical colloquium: Limit states design for foundations. part ii. development for the national building code of canada. *Canadian Geotechnical Journal*, 33(6):984–1007, 1997.

[19] J. Benesty, J. Chen, Y. Huang, and I. Cohen. Pearson correlation coefficient. In *Noise reduction in speech processing*, pages 1–4. Springer, 2009.

[20] R. Bergua, A. Robertson, J. Jonkman, A. Platt, A. Page, J. Qvist, E. Amet, Z. Cai, H. Han, A. Beardsell, et al. Oc6 phase ii: Integration and verification of a new soil–structure interaction model for offshore wind design. *Wind Energy*, 2021.

[21] A. Betz. Das maximum der theoretisch möglichen ausnützung des windes durch windmotoren. *Zeitschrift für das gesamte Turbinenwesten*, 20, 1920.

[22] S. Bhattacharya. *Design of foundations for offshore wind turbines*. John Wiley & Sons, 2019.

[23] R. Boulanger and I. Idriss. State normalization of penetration resistance and the effect of overburden stress on liquefaction resistance. *Proceedings 11th SDEE and 3rd ICEGE. Berkeley, CA*, 2004.

[24] E. R. Bowman. *Investigation of the lateral resistance to movement of a plate in cohesionless soil*. PhD thesis, University of Texas at Austin, 1958.

[25] H. Breuning-Madsen and N. H. Jensen. Pedological regional variations in well-drained soils, denmark. *Geografisk Tidsskrift-Danish Journal of Geography*, 92(1):61–69, 1992.

[26] H. J. Burd, D. M. Taborda, L. Zdravković, C. N. Abadie, B. W. Byrne, G. T. Houlsby, K. G. Gavin, D. J. Igoe, R. J. Jardine, C. M. Martin, et al. Pisa design model for monopiles for offshore wind turbines: application to a marine sand. *Géotechnique*, 70(11):1048–1066, 2020.

[27] B. W. Byrne, G. T. Houlsby, H. J. Burd, K. G. Gavin, D. J. Igoe, R. J. Jardine, C. M. Martin, R. A. McAdam, D. M. Potts, D. M. Taborda, et al. Pisa design model for monopiles for offshore wind turbines: application to a stiff glacial clay till. *Géotechnique*, 70(11):1030–1047, 2020.

[28] Y. Cai, F. Bransby, C. Gaudin, and M. Uzielli. A framework for the design of vertically loaded piles in spatially variable soil. *Computers and Geotechnics*, 134:104140, 2021.

[29] G. Casella and R. L. Berger. Statistical inference: Cengage learning, 2001.

[30] C. Chan and B. K. Low. Reliability analysis of laterally loaded piles involving nonlinear soil and pile behavior. *Journal of Geotechnical and Geoenvironmental Engineering*, 135(3):431–443, 2009.

[31] T. Charlton and M. Rouainia. Cyclic performance of a monopile in spatially

variable clay using an advanced constitutive model. *Soil Dynamics and Earthquake Engineering*, 140:106437, 2021.

[32] C. Cherubini. Probabilistic approach to the design of anchored sheet pile walls. *Computers and Geotechnics*, 26(3-4):309–330, 2000.

[33] C. Cherubini. Reliability evaluation of shallow foundation bearing capacity on c'φ'soils. *Canadian Geotechnical Journal*, 37(1):264–269, 2000.

[34] J. Ching. *Practical Monte Carlo based reliability analysis and design methods for geotechnical problems*. INTECH Open Access Publisher, 2011.

[35] S. E. Cho. Probabilistic assessment of slope stability that considers the spatial variability of soil properties. *Journal of geotechnical and geoenvironmental engineering*, 136(7):975–984, 2010.

[36] R. Chowdhury and D. Xu. Reliability index for slope stability assessment—two methods compared. *Reliability Engineering & System Safety*, 37(2):99–108, 1992.

[37] A. Correia. A pile-head macro-element approach to seismic design of monoshaft-supported bridges. *Unpublished PhD thesis). European School for Advanced Studies in Reduction of Seismic Risk (ROSE School), Pavia, Italy*, 2011.

[38] S. R. Dash, S. Bhattacharya, A. Blakeborough, and M. Hyodo. Py curve to model lateral response of pile foundations in liquefied soils. In *14th World Conference on Earthquake Engineering Beijing, China*, pages 12–17, 2008.

[39] I. Depina, T. M. H. Le, G. Eiksund, and T. Benz. Behavior of cyclically loaded monopile foundations for offshore wind turbines in heterogeneous sands. *Computers and geotechnics*, 65:266–277, 2015.

[40] G. Dnv. *DNVGL-ST-0126: Support structures for wind turbines*. 2016.

[41] P. Doherty and K. Gavin. Laterally loaded monopile design for offshore wind farms. *Proceedings of the institution of civil engineers-energy*, 165(1):7–17, 2012.

[42] A.-K. El Haj, A.-H. Soubra, and J. Fajoui. Probabilistic analysis of an offshore monopile foundation taking into account the soil spatial variability. *Computers and Geotechnics*, 106:205–216, 2019.

[43] G. A. Fenton. Error evaluation of three random-field generators. *Journal of engineering mechanics*, 120(12):2478–2497, 1994.

[44] T. J. F. M. Ferradosa. Reliability analysis applied to the optimization of dynamic scour protections for offshore windfarm foundations. 2018.

[45] W. S. Forrest and T. L. Orr. Reliability of shallow foundations designed to eurocode 7. *Georisk*, 4(4):186–207, 2010.

[46] M. Georgiadis. Development of py curves for layered soils. In *Geotechnical practice in offshore engineering*, pages 536–545. ASCE, 1983.

[47] J. R. Giampa and A. S. Bradshaw. A simple method for assessing the peak friction angle of sand at very low confining pressures. *Geotechnical Testing Journal*, 41(4):639–647, 2018.

[48] A. Glisic, G. T. Ferraz, and P. Schaumann. Sensitivity analysis of monopiles' fatigue stresses to site conditions using monte carlo simulation. In *The 27th International Ocean and Polar Engineering Conference*. OnePetro, 2017.

[49] E. W. Grafarend. *Linear and nonlinear models: fixed effects, random effects, and mixed models*. de Gruyter, 2006.

[50] D. Griffiths and G. A. Fenton. Probabilistic slope stability analysis by finite elements. *Journal of geotechnical and geoenvironmental engineering*, 130(5):507–518, 2004.

[51] S. Haldar and G. S. Babu. Effect of soil spatial variability on the response of laterally loaded pile in undrained clay. *Computers and Geotechnics*, 35(4):537–547, 2008.

[52] S. Haldar, J. Sharma, and D. Basu. Probabilistic analysis of monopile-supported offshore wind turbine in clay. *Soil Dynamics and Earthquake Engineering*, 105:171–183, 2018.

[53] M. E. Harr. *Reliability-based design in civil engineering*, volume 20. Department of Civil Engineering, School of Engineering, North Carolina State ..., 1984.

[54] Y. Hata, K. Ichii, and K.-i. Tokida. A probabilistic evaluation of the size of earthquake induced slope failure for an embankment. *Georisk: Assessment and Management of Risk for Engineered Systems and Geohazards*, 6(2):73–88, 2012.

[55] J. C. Helton and F. J. Davis. Latin hypercube sampling and the propagation of uncertainty in analyses of complex systems. *Reliability Engineering & System Safety*, 81(1):23–69, 2003.

[56] C. Horgan. Using energy payback time to optimise onshore and offshore wind turbine foundations. *Renewable energy*, 53:287–298, 2013.

[57] A. P. Institute. *RP2A-WSD: Recommended Practice for Planning, Designing and Constructing Fixed Offshore Platforms – Working Stress Design*. 1993.

[58] R. A. Jaeger and I. P. Maki. Estimating the peak friction angle of sandy soils in situ with state-based overburden normalized cpt tip resistance. 2016.

[59] J. JCSS. Probabilistic model code. *Joint Committee on Structural Safety*, 2001.

[60] S.-H. Jiang, D.-Q. Li, Z.-J. Cao, C.-B. Zhou, and K.-K. Phoon. Efficient system reliability analysis of slope stability in spatially variable soils using monte carlo simulation. *Journal of Geotechnical and Geoenvironmental Engineering*, 141(2):04014096, 2015.

[61] D. Kallehave, B. W. Byrne, C. LeBlanc Thilsted, and K. K. Mikkelsen. Optimization of monopiles for offshore wind turbines. *Philosophical Transactions of the Royal Society A: Mathematical, Physical and Engineering Sciences*, 373(2035):20140100, 2015.

[62] M. Karimirad. *Offshore energy structures: for wind power, wave energy and hybrid marine platforms*. Springer, 2014.

[63] A. Kaveh and S. Sabeti. Optimal design of monopile offshore wind turbine structures using cbo, ecbo, and vps algorithms. *Scientia Iranica*, 26(3):1232–1248, 2019.

[64] I. Komusanac, G. Brindley, D. Fraile, and L. Ramirez. 2020 statistics and the outlook for 2021-2025. 2021.

[65] F. Kulhawy. On the evaluation of soil properties, asce geotech. *Spec. Publ*, (31):95–115, 1992.

[66] T. M. H. Le, G. R. Eiksund, P. J. Strøm, and M. Saue. Geological and geotechnical characterisation for offshore wind turbine foundations: A case study of the sheringham shoal wind farm. *Engineering geology*, 177:40–53, 2014.

[67] I. Lee and W. White. Ingles, 0. g.'. *Geotechnical Engineering. Pitman, Boston*, 1983.

[68] O. B. Leite. *Review of design procedures for monopile offshore wind structures*. 2015.

[69] K. Lesny. *Foundations for offshore wind turbines: tools for planning and design*. VGE Verlag GmbH, 2010.

[70] B. Low and W. H. Tang. Efficient reliability evaluation using spreadsheet. *Journal of engineering mechanics*, 123(7):749–752, 1997.

[71] B. Low, C. Teh, and W. H. Tang. Stochastic nonlinear py analysis of laterally loaded piles. 2001.

[72] P. Lumb. The variability of natural soils. *Canadian geotechnical journal*, 3(2):74–97, 1966.

[73] P. Lumb. Safety factors and the probability distribution of soil strength. *Canadian Geotechnical Journal*, 7(3):225–242, 1970.

[74] W. Luo, T. Xuan, and J. Li. Estimating anisotropic soil properties using bayesian kriging. In *Geo-Risk 2017*, pages 370–381. 2017.

[75] M. Matsuo and K. Kuroda. Probabilistic approach to design of embankments. *Soils and Foundations*, 14(2):1–17, 1974.

[76] C. Matutano, V. Negro, J.-S. López-Gutiérrez, and M. D. Esteban. Scour prediction and scour protections in offshore wind farms. *Renewable energy*, 57:358–365, 2013.

[77] S. Mazzoni, F. McKenna, M. H. Scott, G. L. Fenves, et al. *OpenSees command language manual*, volume 264. Berkeley, California, United States, 2006.

[78] B. McClelland and J. A. Focht Jr. Soil modulus for laterally loaded piles. *Transactions of the American Society of Civil Engineers*, 123(1):1049–1063, 1958.

[79] F. Nadim. Tools and strategies for dealing with uncertainty in geotechnics. In *Probabilistic methods in geotechnical engineering*, pages 71–95. Springer, 2007.

[80] V. Nguyen and R. Chowdhury. Probabilistic study of spoil pile stability in strip coal mines—two techniques compared. In *International Journal of Rock Mechanics and Mining Sciences & Geomechanics Abstracts*, volume 21, pages 303–312. Elsevier, 1984.

[81] E. A. Oğuz. Spatial probabilistic evaluation of sea bottom soil properties and its effect on foundation design. Master's thesis, 2017.

[82] E. A. Oguz and N. Huvaj. Spatial probabilistic evaluation of offshore/nearshore sea bottom soils based on cone penetration tests. *Bulletin of Engineering Geology and the Environment*, 79(2):971–983, 2020.

[83] E. A. Oguz, N. Huvaj, and D. Griffiths. Vertical spatial correlation length based on standard penetration tests. *Marine Georesources & Geotechnology*, 37(1):45–56, 2019.

[84] E. A. Oguz, Y. Yalcin, and N. Huvaj. Probabilistic slope stability analyses: effects of the coefficient of variation and the cross-correlation of shear strength parameters. In *Geotechnical Frontiers 2017*, pages 363–371. 2017.

[85] A. M. Page, G. Grimstad, G. R. Eiksund, and H. P. Jostad. A macro-element pile foundation model for integrated analyses of monopile-based offshore wind turbines. *Ocean Engineering*, 167:23–35, 2018.

[86] K.-K. Phoon and F. H. Kulhawy. Characterization of geotechnical variability. *Canadian geotechnical journal*, 36(4):612–624, 1999.

[87] M. Pourahmadi. Cholesky decompositions and estimation of a covariance matrix: orthogonality of variance–correlation parameters. *Biometrika*, 94(4):1006–1013, 2007.

[88] E. S. M. A. Program. Going global: Expanding offshore wind to emerging markets, 2019.

[89] L. Ramirez, D. Fraile, and G. Brindley. Offshore wind in europe: Key trends and statistics 2019. 2020.

[90] L. Ramirez, D. Fraile, and G. Brindley. Offshore wind in europe: Key trends and statistics 2020. 2021.

[91] C. Reale, J. Tott-Buswell, and L. Prendergast. Impact of geotechnical uncertainty on the preliminary, design of monopiles supporting offshore wind turbines. *ASCE-ASME J Risk and Uncert in Engrg Sys Part B Mech Engrg*, 2021.

[92] L. C. Reese. Non-dimensional solutions for laterally loaded piles with soil modulus assumed proportional to depth. In *Proc. 8th Texas Conf. SMFE, The Univ. of Texas*, 1956.

[93] L. C. Reese, W. R. Cox, and F. D. Koop. Analysis of laterally loaded piles in sand. In *Offshore Technology Conference*. OnePetro, 1974.

[94] L. C. Reese and W. F. Van Impe. *Single piles and pile groups under lateral loading*. CRC press, 2000.

[95] W. S. T. I. W. M. . A. J. A. Reese, L. C. *LPILE v2019 Technical Manual*. Austin, TX, USA: Ensoft Inc. See https://www. ensoftinc. com/products/lpile . . . , 2020.

[96] P. Robertson. Soil classification using the cone penetration test: Reply. *Canadian Geotechnical Journal*, 28(1):176–178, 1991.

[97] P. K. Robertson and K. Cabal. Estimating soil unit weight from cpt. In *2nd International Symposium on Cone Penetration Testing*, pages 2–40, 2010.

[98] P. K. Robertson, R. G. Campanella, D. Gillespie, and J. Greig. Use of piezometer cone data. In *Use of in situ tests in geotechnical engineering*, pages 1263–1280. ASCE, 1986.

[99] B. Rogiers, D. Mallants, O. Batelaan, M. Gedeon, M. Huysmans, and A. Dassargues. Model-based classification of cpt data and automated lithostratigraphic mapping for high-resolution characterization of a heterogeneous sedimentary aquifer. *PloS one*, 12(5):e0176656, 2017.

[100] M. Rouholamin, S. Bhattacharya, and D. Lombardi. Winkler springs (py curves) for liquefied soil from element tests. 2015.

[101] A. RP et al. *Planning, designing, and constructing fixed offshore platforms—Working stress design*. 2014.

[102] S. Sayed, G. Dodagoudar, and K. Rajagopal. Reliability analysis of reinforced soil walls under static and seismic forces. *Geosynthetics International*, 15(4):246–257, 2008.

[103] M. Schevenels. The impact of uncertain dynamic soil characteristics on the prediction of ground vibrations. 2007.

[104] E. Schultze. Frequency distributions and correlations of soil properties. *Statistics and Probability in Civil Engineering, Hong Kong University Press, distributed by Oxford University Press, London*, 1972.

[105] S. P. H. Sørensen, L. B. Ibsen, and A. H. Augustesen. Effects of diameter on initial stiffness of py curves for large-diameter piles in sand. *Numerical Methods in Geotechnical Engineering*, pages 907–912, 2010.

[106] X. Sun, D. Huang, and G. Wu. The current state of offshore wind energy technology development. *Energy*, 41(1):298–312, 2012.

[107] M. Tabarroki, F. Ahmad, R. Banaki, S. K. Jha, and J. Ching. Determining the factors of safety of spatially variable slopes modeled by random fields. *Journal of Geotechnical and Geoenvironmental Engineering*, 139(12):2082–2095, 2013.

[108] K. Terzaghi. Evalution of conefficients of subgrade reaction. *Geotechnique*, 5(4):297–326, 1955.

[109] M. J. Vahdatirad, L. V. Andersen, L. B. Ibsen, J. Clausen, and J. D. Sørensen. Probabilistic three-dimensional model of an offshore monopile foundation: Reliability based approach. In *Seventh international conference on case histories in geotechnical engineering*, 2013.

[110] G. Van Alboom and A. Baertsoen. Geotechnical characterisation and monitoring versus fem calculation results for a massive quay wall in the harbour of antwerp, belgium. In *Proceedings of the 16th International Conference on Soil Mechanics and Geotechnical Engineering*, pages 1137–1140. IOS Press, 2005.

[111] R. Van der Have. Random fields for non-linear finite element analysis of reinforced concrete. 2015.

[112] W. N. Wandji, A. Natarajan, N. Dimitrov, and T. Buhl. Design of monopiles for multi-megawatt wind turbines at 50 m water depth. In *EWEA Annual Conference and Exhibition 2015*, pages 8–12. European Wind Energy Association (EWEA), 2015.

[113] Y. Wang and Z. Cao. Probabilistic characterization of young's modulus of soil using equivalent samples. *Engineering Geology*, 159:106–118, 2013.

[114] X. Z. Wu. Trivariate analysis of soil ranking-correlated characteristics and its application to probabilistic stability assessments in geotechnical engineering problems. *Soils and Foundations*, 53(4):540–556, 2013.

[115] M. Zhu. The openseespy library. `https://openseespydoc.readthedocs.io/en/latest/index.html#`, 2019. Accessed: 2021-11-20.